Space-Time Multiscale-Multiphysics Homogenization Methods for Heterogeneous Materials

Mahesh Raju Bailakanavar

Submitted in partial fulfillment of the
requirements for the degree of
Doctor of Philosophy
in the Graduate School of Arts and Sciences

COLUMBIA UNIVERSITY
2013

© 2013

Mahesh Raju Bailakanavar

All rights reserved

Abstract

Space-Time Multiscale-Multiphysics Homogenization Methods for Heterogeneous Materials

Mahesh Raju Bailakanavar

We present a unified, homogenization framework for computational analysis of heterogeneous materials consisting of multiple length scales, multiple time scales and coupled-multiple physics. The research efforts also addresses the technological issues associated with modeling the morphological details of microstructures with randomly distributed inclusions. The Random Sequential Adsorption (RSA) algorithm is improved to accurately and effectively model the morphological details of materials with randomly distributed inclusions. The proposed algorithm is more robust; computational efficient and versatile in comparison to the existing methods. A temporal homogenization scheme is developed and integrated with the previously developed spatial homogenization theory for fatigue life analysis of heterogeneous materials. The unified space-time multiscale homogenization model is validated for fatigue life prediction of elevated temperature Ceramic Matrix Composites (CMCs). In the final phase of the research a mathematical model for coupled moisture diffusion-mechanical deformation is developed. This model is integrated with the spatial homogenization framework to analyze problems consisting of multiple length scales and coupled-multiple physics. The unified multiscale-multiphysics model is validated for evaluating the degradation of physical and mechanical properties of short glass fiber and carbon fiber filled thermoplastic material systems.

Contents

Contents ... i

List of Tables ... v

List of Figures ... vi

Chapter 1 ... 2

Introduction and Scope ... 2

- 1.1 Introduction ... 2
- 1.2 Scope of the Thesis ... 6
- 1.3 Thesis Outline ... 7

Chapter 2 ... 11

Multiscale Homogenization for Heterogeneous Materials ... 11

- 2.1 Introduction ... 11
- 2.2 Spatial Homogenization Model for Vector Fields ... 11
  - 2.2.1 Residual-Free Fields and Model Reduction ... 17
  - 2.2.2 Reduced Order System of Equations ... 22
- 2.3 Numerical Implementation ... 25

Chapter 3 ... 30

Parametric Generation of Unit Cells with Randomly Distributed Inclusions ... 30

- 3.1 Introduction ... 30
- 3.2 Hierarchical Random Sequential Adsorption (HRSA) ... 34

3.2.1 Unit Cell Geometry Definition 34
3.2.2 Forced Packing 35
3.3 Unforced Packing 39
3.4 Hierarchical Inclusion Generation Strategy 40
3.4.1 Method of Radial Distances 40
3.4.2 Method of Separating Planes 41
3.4.3 Method of Separating Axes 42
3.5 Chopped Fibers Randomly Oriented in 2D Plane 44
3.6 Inclusions Randomly Oriented in 3D Space 51
3.6.1 Randomly Oriented Chopped Fibers Embedded in Matrix 51
3.6.2 Randomly Oriented Bonded Fibers Free of Matrix (FiberForm) 52
3.6.3 Ellipsoidal Inclusions Randomly Oriented in 3D Space 54
3.7 Statistical Study to Determine the Size of Unit Cell 57
3.7.1 Carbon Fiber Microstructure 60
3.7.2 Glass Fiber Microstructure 65
3.8 Methodology to Control the Volume Fractions of Constituent Phases 69
3.9 Conclusion 70
Chapter 4 72
Space-Time Multiscale Homogenization for Heterogeneous Materials 72
4.1 Introduction 72

4.2 Temporal Homogenization 74

4.3 Unified Space-Time Multiscale Homogenization 80

4.4 Fatigue Damage Model 84

4.5 Implementation of the Space-Time Multiscale Homogenization Model 85

4.5.1 Integration of Spatial Homogenization Model 86

4.5.2 Integration of Temporal Homogenization Model 88

4.6 Validation of the Space-Time Multiscale Homogenization Model.........................92

4.6.1 Validation of Fatigue Damage Model 93

4.6.2 Validation of Fatigue Life Prediction Model...97

4.7 Discussion 102

4.8 Conclusions...103

Chapter 5 106

Multiscale-Multiphysics Homogenization for Heterogeneous Materials.....................................106

5.1 Introduction 106

5.2 Effects of Moisture on the Properties of Polyamides 110

5.2.1 Effect of Moisture on the Glass Transition Temperature of Polyamides .110

5.2.2 Formulation for Maximum Moisture Content..113

5.2.3 Effect of Moisture on Strength and Stiffness of Polyamides......................114

5.3 Coupled Multiphysics Model...116

5.4 Unified Multiscale-Multiphysics Homogenization...120

5.4.1 Residual-Free Fields and Model Reduction 122

5.4.2 Reduced Order System of Equations 125

5.5 Implementation of the Multiscale-Multiphysics Homogenization Model 127

5.6 Experimental Program 129

5.7 Validation of the Multiscale-Multiphysics Homogenization Model 130

5.7.1 Moisture Conditioning as per ISO1110 (70C & 62% RH) 132

5.7.2 Uniaxial Tensile Tests for Dry As Molded Conditions (ISO 527-2) 135

5.7.3 Sequential Diffusion-Mechanical Problem 138

5.7.4 Three Point Bending Test 141

5.8 Conclusion 146

References 147

List of Tables

Table 1: Details of the microstructure of the two material systems 131

Table 2: Parameters of the resin mechanical model 136

List of Figures

Figure 1: The space-time multiscale-multiphysics attribute space 7

Figure 2: Illustration of coarse scale and fine scale domains 13

Figure 3: Illustration of a reduced order model 17

Figure 4: Schematic of the two scale reduced order homogenization 28

Figure 5: Hierarchal levels in the HRSA algorithm 35

Figure 6: Fiber-2 forced to bend over fiber-1 at the intersecting point 36

Figure 7: Four additional vertices added on fiber-2 to enforce shape change 37

Figure 8: Intersection of two line segments 38

Figure 9: Intersection check in 2D using method of separating axes 43

Figure 11: Random chopped fiber unit cell geometry 47

Figure 12: Division of the unit cell volume into five zones 47

Figure 13: Hierarchical RSA algorithm 50

Figure 14: Straight chopped fibers randomly distributed in 3D 52

Figure 15 (a) FiberForm unit cell with fiber volume fraction 5% and cross section radius equal to 2.4; (b) FiberForm unit cell with fiber volume fraction 10% and cross section radius equal to 0.6 54

Figure 16: (a) Geometry of an ellipsoidal inclusion (b) an ellipsoidal inclusion unit cell 55

Figure 17: Discretization of an ellipsoidal inclusion into 48 faces 55

Figure 18: A three-step hierarchical intersection check algorithm 56

Figure 19: Comparison of cpu times between method of separating axes and the 3-step hierarchical method 57

Figure 20: Statistical study framework 60

Figure 21: Carbon fiber microstructure: Averaged in-plane moduli for SR=1.0 61

Figure 22: Carbon fiber microstructure: Averaged in-plane moduli for SR=1.5 61

Figure 23: Carbon fiber microstructure: Averaged in-plane moduli for SR=2.0 61

Figure 24: Averaged in-plane moduli for SR=2.0 and SR=2.5 62

Figure 25: Carbon fiber microstructure: Averaged in-plane moduli for SR=3.0 62

Figure 26: Mean of homogenized modulus for carbon fiber microstructure for SR=1.0 to SR=3.0 63

Figure 27: Variance of homogenized modulus for carbon fiber microstructure for SR=1.0 to SR=3.0 63

Figure 28: Carbon fiber microstructure: Relative error for SR=1.0 to SR=3.0 64

Figure 29: CPU time for SR=1.0 to SR=3.0 64

Figure 30: Glass fiber microstructure: Averaged in-plane moduli for SR=1.0 66

Figure 31: Glass fiber microstructure: Averaged in-plane moduli for SR=1.5 66

Figure 32: Glass fiber microstructure: Averaged in-plane moduli for SR=2.0 66

Figure 33: Glass fiber microstructure: Averaged in-plane moduli for SR=2.5 67

Figure 34: Glass fiber microstructure: Averaged in-plane moduli for SR=3.0 67

Figure 35: Glass fiber microstructure: Averaged in-plane moduli for SR=3.0 and relative errors 67

Figure 36: The in-plane elastic modulus variance as a function of the size ratio for both the carbon and glass fiber unit cell microstructures 68

Figure 37: Schematic of the two scale reduced order homogenization model 88

Figure 38: Adaptive block scheme for fatigue life estimation 90

Figure 39: Schematic of the unified multi space-time homogenization framework 92

Figure 40: Unit cell model (21767 elements, 4298 nodes) 93

Figure 41: Piecewise damage evolution functions for matrix phase (left) and tow phase (right) 94

Figure 42: ¼th simulation model of eight-layer, five harness satin weave, ceramic composite...95

Figure 43: Comparison between experimental and simulation stress-strain curves......................96

Figure 44: Damage evolution as a function of the phase equivalent strain at 2100F 96

Figure 45: Damage evolution as a function of the phase equivalent strain at 2300F 97

Figure 46: Damage evolution as a function of the phase equivalent strain at 2400F 97

Figure 47: Simulation vs experimental results at 1Hz and 2100F 98

Figure 48: Simulation vs experimental results at 1Hz and 2300F 99

Figure 49: Simulation vs experimental results at 1Hz and 2400F 99

Figure 50: Gamma exponent vs load for varying temperatures at 1Hz..99

Figure 51: Gamma exponent vs temperature for varying loads at 1Hz..100

Figure 52: Simulation vs experimental results at 60Hz and 2100F 100

Figure 53: Simulation vs experimental results at 60Hz and 2300F 100

Figure 54: Simulation vs experimental results at 60Hz and 2400F 101

Figure 55: Gamma exponent vs load for various temperatures at 60Hz 101

Figure 56: Gamma exponent vs temperature for various loads at 60 Hz 101

Figure 57: Tg of Ultramid® T KR4357 G6 in dry state and moisture conditioned state [121] 111

Figure 58: Tg of Ultramid® T KR4370 C6 in dry state and moisture conditioned state [121]......111

Figure 59: Schematic representation of the $T_g(w)$ relationship [122]...112

Figure 60: Interaction of amide groups with absorbed moisture in PA-6 [118]............................113

Figure 61: Plot depicting decrease in modulus and strength of nylon-6 due to moisture ingression [121]...115

Figure 62: Illustration of the coarse and fine scale fields...116

Figure 63: Schematic of the unified multiscale-multiphysics formulation...................................129

Figure 64: Details of the experimental program..130

Figure 65 : Unit cell geometry (a) glass fiber filled (BASF, Ultramid® T KR4357 G6) (b) carbon fiber filled polyamide systems (BASF, Ultramid® T KR4370 132

Figure 66: Moisture uptake for glass fiber filled (BASF, Ultramid® T KR4357 G6) tensile specimen 133

Figure 67: Moisture uptake for glass fiber filled (BASF, Ultramid® T KR4357 G6) flex specimen 133

Figure 68: Moisture uptake for glass fiber filled (BASF, Ultramid® T KR4357 G6) impact specimen 134

Figure 69: Moisture uptake for carbon fiber filled (BASF, Ultramid® T KR4370 C6) tensile specimen 134

Figure 70: Moisture uptake for carbon fiber filled (BASF, Ultramid® T KR4370 C6) flex specimen 135

Figure 71: Moisture uptake for carbon fiber filled (BASF, Ultramid® T KR4370 C6) impact specimen 135

Figure 72: Schematic of the three-piece linear damage model 136

Figure 73: Stress-Strain plot for glass fiber filled (BASF, Ultramid® T KR4357 G6) 00 specimen 137

Figure 74: Stress-Strain plot for glass fiber filled (BASF, Ultramid® T KR4357 G6) 900 specimen 137

Figure 75: Stress-Strain plot for carbon fiber filled (BASF, Ultramid® T KR4370 C6) 00 specimen 137

Figure 76: Stress-Strain plot for carbon fiber filled (BASF, Ultramid® T KR4370 C6) 900 specimen 138

Figure 77: Uniaxial tensile test results for KR4357 GF 00 specimen 139

Figure 78: Uniaxial tensile test results for KR4357 GF 900 specimen... 139

Figure 79: Uniaxial tensile test results for KR4357 CF 00 specimen.. 140

Figure 80: Uniaxial tensile test results for KR4357 CF 900 specimen... 140

Figure 81: Schematic of the 3-point bending test (ASTM D790).. 141

Figure 82: Finite element model of the 3-point bending test (ASTM D790) 142

Figure 83: Contour plot of the displacements for Ultramid® T KR4357 G6 0^0 samples in DAM state 142

Figure 84: Plot of force-displacement for Ultramid® T KR4357 G6 0^0 samples in DAM state.... 143

Figure 85: Contour plot of the displacements for Ultramid® T KR4357 G6 0^0 samples in moisture conditioned state 143

Figure 86: Plot of force-displacement for Ultramid® T KR4357 G6 0^0 samples in moisture conditioned state 144

Figure 87: Contour plot of the displacements for Ultramid® T KR4357 G6 90^0 samples in DAM state 144

Figure 88: Plot of force-displacement for Ultramid® T KR4357 G6 90^0 samples in DAM state . 145

Figure 89: Contour plot of the displacements for Ultramid® T KR4357 G6 90^0 samples in moisture conditioned state 145

Figure 90: Plot of force-displacement for Ultramid® T KR4357 G6 90^0 samples in moisture conditioned state 146

Acknowledgements

I am extremely thankful to my wife, Tavishi Tiwari for her support without which this work would not have been possible. She has unwaveringly stood by my side and has encouraged and inspired me at each and every phase of my academic journey. I'm thankful to my parents Raju Bailakanavar and Saroja Bailakanavar for their support and encouragement. I want to express my gratitude to my parents-in-law Harish Tiwari and Sumitra Tiwari for their love, support and encouragement.

I have been very fortunate to work under Prof. Jacob Fish who is an esteemed researcher, a teacher and a mentor as well. He has taught and advised me throughout this academic journey and has constantly inspired and encouraged to excel in my academic research. I also want to thank Thomas Cook and Lynn Powers from Rollys Royce Corporation for their support of our collaborative work. It gives me great pleasure in expressing my gratitude to Venkat Aitharaju, Hamid Kia and William Rodgers from General Motors for providing all the valuable guidance and training during our collaborative work. I am also thankful to Prof Haim Waisman, Prof. Huming Yin and Prof. Sanat Kumar for agreeing to serve on my dissertation committee. I owe my deepest gratitude to Pawel Woelke and Najib Abboud at Weidlinger Associates for their support and encouragement as well.

I share the credit of my work with my fellow research group members Vasilina Filonova, Nan Hu, Yang Liu, Yuan Zifeng, Yuan Zheng and Tao Jiang. It's my pleasure to make a special mention of my closest buddies Badri Hiriyur, Suparno Mukhopadhyay, Luc Berger and Sergey Kuznetsov for their support, encouragement and valuable guidance in pursuing my research work. Thanks to my friends Malini, Uttam & Mahua, Shouvik & Tulika and others at Columbia University for making this PhD journey a memorable one. Last but not the least a special thanks to my pooch "Muffin" for his ever unconditional love.

PART I

INTRODUCTION

Chapter 1

Introduction and Scope

In this introductory chapter, the scope of the author's research and the motivation for the study is presented along with a brief outline of this dissertation.

1.1 Introduction

A composite material is created by combining two materials to produce a material that is superior to the individual materials and unique in terms of the physical and mechanical properties. The first use of composite materials dates back to the 1500s B.C., when the Egyptians and the Mesopotamians mixed straw with mud to create more durable dwellings [1]. Straw was also effectively used to strengthen pottery products and boats. The genesis of modern era composite materials can be traced back to 1937 when Owens Corning Fiberglass Company started producing glass fibers. The incorporation of glass fiber reinforced plastics (GFRPs) into the industrial world inspired researchers to develop new resin materials (vinyl, polystyrene and plexi-glass) that defied nature's own materials. With the advent of unsaturated polyester resins (patented in 1936) the production of GFRPs became more viable due to the ease in curing these resins.

The Second World War further augmented the development of composites, as an increasingly more number of aircrafts were produced. An ever increasing use of fiber reinforced composites in aerospace and naval applications was seen in the early 1940's due to their superior physical and mechanical properties like low strength to weight ratio and resistance to corrosion and environmental degradation. During this time composites were mainly used in tooling, but the use of these materials in structural and semi-structural parts was constantly explored.

The end of the World War II paved the way for commercial companies to extend the expertise in composite materials applications to public sector industries. The obvious choices were the commercial boat building and automobile industries. In 1953 the Molded Fiber Glass Corporation (MFG) along with Chevrolet Motor Company unveiled the first car Chevrolet Corvette with fiber glass reinforced body panels. In addition to the aerospace, marine, automotive and corrosion resistance applications, composite materials were incorporated in the construction industry as well. The push for aerospace dominance in the 1950's and the 60's saw a renewed impetus in the development of composite materials and that resulted in the invention of carbon composites. The development of these high performance carbon and glass fibers along with the advancements in polymers have contributed to the expansion of composite materials market into high temperature aerospace materials, armors, sports equipment and medical devices.

Yet with their superior physical properties contributing to enhanced performance, incorporation of composite materials as primary structural members is still a subject of active research. The primary reason contributing to the present state of affairs is the inability to accurately predict the behavior of these materials. This lack of predictability more often than not results in an overdesign, thereby offsetting the very advantages offered by these heterogeneous materials. Some of the reasons contributing to the current state of affairs are as follows

(i) Existence of multiple spatial scales due to the inherent heterogeneous nature of composite materials;

(ii) Inability to accurately model the microstructure and characterize the material models at various scales;

(iii) Existence of multiple temporal scales due to fatigue and multiple physical processes having disparate characteristic time scales;

(iv) Lack of scale separation;

(v) Existence of multiple coupled physical processes such as mechanical-diffusion, mechanical-thermal and mechanical-oxidation-thermal processes; and

(vi) Lack of enough experimental data at multiple scales or inability to separate the spatial scales in the material;

But with an ever increasing impetus for weight reduction, enhanced performance and reduction in time and cost involved with conducting tests on one hand and the recent developments in computational sciences and the enormous computational power of present generation machines on the other hand, the present phase in the history of composite materials is apt to develop computational tools to accurately model the behavior and performance of composite materials.

The overall effective properties of these heterogeneous materials depend upon the size, shape, spatial orientation and physical properties of the constituents comprising the microstructure. Various theories have been put forth to predict the behavior of composite materials. Among the noteworthy methods are the rule of mixtures, the effective medium models, the self-consistent methods, and the asymptotic homogenization theories.

The rule of mixture theories of Voight [2] and Reuss [3] involve computing of homogenized properties by averaging over the respective properties of the phases constituting the microstructure, weighted by their volume fractions. These methods assume either constant strain field (Voight) or constant stress field (Reuss) within material microstructure, and hence, inadequate in predicting the overall response of complex materials.

Considerable improvement has been proposed by Eshelby [4] in the form of effective medium theory. This theory was further enhanced by Hashin [5], Budiansky [6] and Mori-Tanaka [7]. By this approach the effective properties are computed by solving a unit cell boundary value problem consisting of a spherical or ellipsoidal inclusion embedded in an infinite matrix. Hill [8] and Christensen [9] proposed the generalized self-consistent theory, is an extension of the effective medium theory, where the effective properties are computed by solving a unit cell problem consisting of one phase embedded in another phase, properties of which are not known *a priori*. The effective medium models and the self-consistent approaches are well suited for linear elastic problems with structured unit cell geometries; they do not perform well for unit cells with randomly distributed inclusions or clustered inclusions.

Another class of methods, called the variational bounding methods (Hashin and Shtrikman [10]; Hashin [11]; Willis [12]; Ponte Castañeda and Suquet [13]) were developed to provide the lower and upper bounds for the overall properties of heterogeneous materials.

Asymptotic mathematical homogenization theories were first pioneered by Bensoussan [14], Sanchez-Palencia [15] and Bakhvalov and Panasenko [16]. The approach involves asymptotic expansion of the displacement fields over the fine-scale domain and the continuum domain, wherein the two scales are related by the length parameter. However, these homogenization theories fail to account for geometrical and material nonlinearities, multi-axial loading scenarios and the physical and geometrical changes the microstructure undergoes.

A practical implementation of the asymptotic homogenization methods became possible by utilizing finite element methods to solve boundary value problems at multiple scales. The basic premise underlying this theory has been presented in the papers by Guedes and Kikuchi [17]; Terada and Kikuchi [18]; Ghosh *et al.* [19, 20], Smit *et al.*[21], Miehe *et al.*[22], Michel *et al*. [23], Feyel and Caboche [24] , Kuznetsov *et al.* [25] and Fish *et al.*[26-28]. These so called computational homogenization methods are computationally prohibitive for large scale nonlinear problems. To develop a computationally viable method, the tremendous amount of information that exists at a fine scale has to be systematically reduced. One such approach has been offered by transformation field analysis pioneered by Dvorak [29, 30] and later improved by Fish *et al*. [31-33]

A vast majority of the engineering materials are subjected to cyclic loads or a combination of multiple loads like mechanical loads and environmental loads. Due to the difference in physical and mechanical properties, heterogeneous materials exhibit complex behavior in the presence of coupled-multiple physical processes. Experimental studies have shown considerable degradation of overall physical and mechanical properties due to combined effect of moisture diffusion, monotonic and cyclic mechanical/environmental loading, heat transfer and chemical reaction. Clearly, there is a need to extend the finite element based homogenization methods to account for multiple physical processes and multiple time scales. Development of computational tools capable of predicting the behavior of heterogeneous materials subjected to extreme environmental conditions will further extend the realm of application of composite materials and is the main thrust of the proposed research.

1.2 Scope of the Thesis

The primary objective of the proposed research program is to develop a space-time multiscale-multiphysics homogenization framework with emphasis on fatigue and moisture diffusion in composite materials. The proposed mathematical framework is envisioned to encapsulate semantic combinations of the three basic attributes spanning the space, namely length scales, time scales and physical fields as shown in Figure 1 [34]. The scope of the study also involves verification and validation of the proposed framework for random and periodic microstructures. The study also addresses the technological issues associated with modeling the morphological details of random inclusion microstructures.

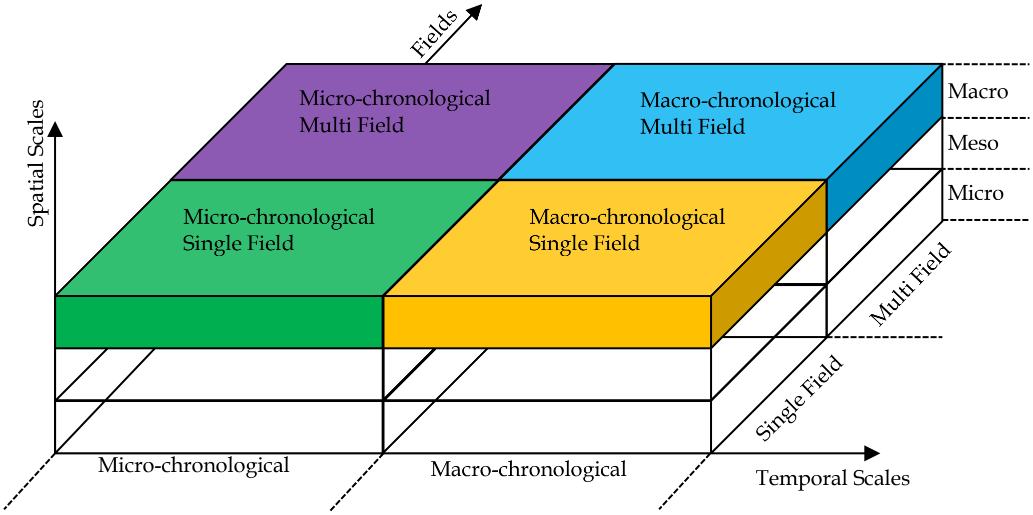
Fields
Spatial Scales
Micro-chronological
Multi Field
Macro-chronological
Multi Field
Micro-chronological
Single Field
Macro-chronological
Single Field
Macro
Meso
Micro
Multi Field
Single Field
Micro-chronological
Macro-chronological
Temporal Scales

Figure 1: The space-time multiscale-multiphysics attribute space

The focus of the first part of the thesis on methods aimed at modeling the morphological details of the composites with randomly distributed inclusions. The second part of the thesis extends the previously developed reduced order spatial homogenization framework to account for multiple temporal scales inherently existing in fatigue. The third part of the thesis extends the reduced order homogenization originally developed for a single physical process to multiple physical processes.

1.3 Thesis Outline

In Chapter 2 we present a parametric model for generating unit cells with randomly distributed inclusions. The proposed algorithm possesses (i) robustness by yielding unit cells with fiber volume fraction of up to 45% for aspect ratios as high as 20, (ii) computational efficiency accomplished through a hierarchy of algorithms with increasing computational complexity, and (iii) versatility by generating unit cells with different inclusion shapes. A statistical study aimed at determining the effective size of the unit cell is conducted. The method has been applied to various random inclusion microstructure composites including: (i) two-dimensional chopped tow composites employed in automotive applications, (ii) polyurea or polyethene coating consisting of hard and soft domains (segments) employed for energy absorption in military and industrial applications, and (iii) fiber framework called *fiberform* embedded in or free from an amorphous matrix used as heat shield on space crafts to prevent structural damage during reentry into the atmosphere.

In chapter 3 the space-time multiscale fatigue life prediction model for heterogeneous materials is developed. The proposed model combines a two-scale asymptotic homogenization approach in time with a "block cycle jump" technique into a unified temporal multiscale framework that can be effectively utilized for arbitrary material architectures and constitutive equations of micro-phases. The unified temporal multiscale approach in combination with a spatial multiscale approach based on the reduced order homogenization is validated for high temperature ceramic matrix composites.

The final phase of this research as described in Chapter 5 involves development of the multiscale-multiphysics homogenization formulation for investigating the kinetics of moisture diffusion in composite materials and the effect of moisture on the strength and stiffness of short fiber thermoplastics. The multiscale-multiphysics homogenization model is validated against experimental results of 30% by weight filled short glass fiber and short carbon fiber filled thermoplastic materials with applications in the automotive industry.

PART II

SPATIAL HOMOGENIZATION

Chapter 2

Multiscale Homogenization for Heterogeneous Materials

In this chapter an overview of the mathematical asymptotic method based spatial homogenization theory for vector field problems is presented. Model reduction along with implementation aspects is discussed as well. This theory presented in this chapter serves as a basis to extend the framework to problems involving multiple domain and coupled-multiple physics problems.

2.1 Introduction

In this chapter the eigen-deformation based multiscale spatial homogenization theory for vector fields is presented. The objective of this chapter is to offer an overview of the spatial homogenization theory, the model reduction technique and the numerical implementation aspects of the reduced order spatial homogenization that is previously developed by Fish *et. al*. [31, 33, 35]. The theory presented in this chapter serves as a basis to extend the multiscale homogenization framework to analyze problems consisting of multiple domains in Chapter 4 and multiple-coupled physical processes in Chapter 5. The chapter is organized as follows. In section 2.2 the two scale direct homogenization theory for nonlinear heterogeneous media is presented. Reformulation of the governing equations in terms of residual stress free fields and model reduction to improve the computational efficiency is presented in subsequent sections.

2.2 Spatial Homogenization Model for Vector Fields

For simplicity we consider the spatial domain consisting of two scales only, a coarse scale and a fine scale respectively. The formulation is presented for small deformations only and therefore no distinction is made between reference coordinates and deformed coordinates. Consider a heterogeneous nonlinear solid media on a composite domain Ω^{ζ} with boundary

$\partial\Omega^{\zeta}$ as shown in Figure 2. The superscript ζ implies the dependence of coarse scale fields on the fine scale fields. The microstructure of a composite material is assumed to be statistically homogeneous with local periodicity. The unit cell domain is denoted by Θ. The size of the unit cell is assumed to be small compared to the characteristic length of the coarse-scale domain Ω so that the asymptotic homogenization theory can be applied. Let x be the coarse-scale position vector in the coarse scale domain Ω and $y_i = x_i / \zeta$ be the fine-scale position vector in Θ where $0 < \zeta \ll 1$. All physical quantities are assumed to have two explicit dependencies: one on the coarse-scale coordinate x and the second one, on the fine scale coordinate y. Using the classical nomenclature, any periodic function can be represented as $f^{\zeta}(x) \equiv f(x, y(x)) \equiv f(x, y(x) + k\hat{y})$

The indirect coarse-scale spatial derivatives of the response function $f^{\zeta}(x)$ can be calculated by the chain rule as

$$f^{\zeta}{}_{,i} = \underbrace{\frac{\partial f(x,y)}{\partial x_i}}_{f_{,x_i}} + \frac{1}{\zeta}\underbrace{\frac{\partial f(x,y)}{\partial y_i}}_{f_{,y_i}} \tag{2.1}$$

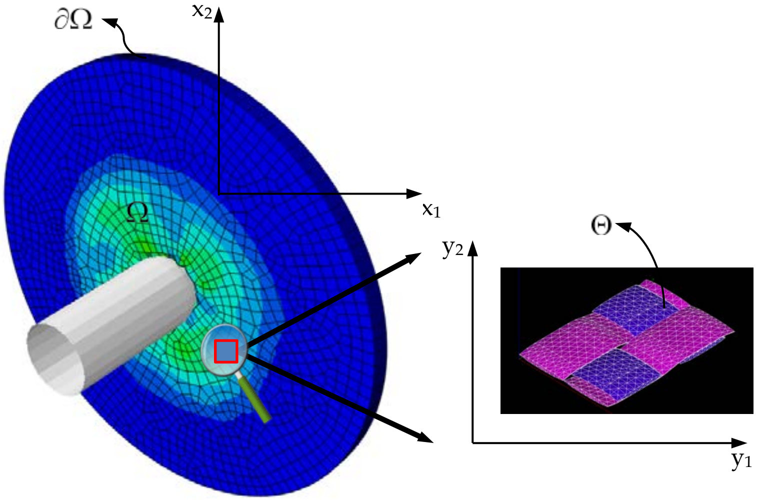

Figure 2: Illustration of coarse scale and fine scale domains

We assume that the micro constituents possess homogeneous properties and satisfy the following boundary value problem:

$$
\begin{aligned}
&\sigma^{\zeta}_{ij,j}(x)+b^{\zeta}_{i}(x)=0 \quad x\in\Omega^{\zeta}, \\
&\sigma^{\zeta}_{ij}(x)=L^{\zeta}_{ijkl}(x)\left(\varepsilon^{\zeta}_{kl}(x)-\mu^{\zeta}_{kl}(x)\right) \quad x\in\Omega^{\zeta}, \\
&\varepsilon^{\zeta}_{ij}(x)=u^{\zeta}_{(i,j)}(x)\equiv\frac{1}{2}\left(u^{\zeta}_{i,j}+u^{\zeta}_{j,i}\right) \quad x\in\Omega^{\zeta}, \\
&\mu^{\zeta}_{kl}(x)=\sum_{I}\mu^{I\zeta}_{kl}(x) \quad x\in\Omega^{\zeta}, \\
&u^{\zeta}_{i}(x)=\overline{u}^{\zeta}_{i}(x) \quad x\in\partial\Omega^{u\zeta}, \\
&\sigma^{\zeta}_{ij}(x)n^{\zeta}_{j}(x)=\overline{t}^{\zeta}_{i}(x) \quad x\in\partial\Omega^{t\zeta}, \\
&\delta^{\zeta}_{i}(x)\equiv\left[\!\left[u^{\zeta}_{i}(x)\right]\!\right]=u^{\zeta}_{i}\Big|_{S^{\zeta}_{-}}-u^{\zeta}_{i}\Big|_{S^{\zeta}_{+}} \quad x\in S^{\zeta}, \\
&\sigma^{\zeta}_{ij}n^{\zeta}_{j}\Big|_{S^{\zeta}_{+}}+\sigma^{\zeta}_{ij}n^{\zeta}_{j}\Big|_{S^{\zeta}_{-}}=t^{\zeta}_{i}\Big|_{S^{\zeta}_{+}}+t^{\zeta}_{i}\Big|_{S^{\zeta}_{-}}=0
\end{aligned}
\tag{2.2}
$$

The total strain ε^{ζ}_{kl} in equation (2.2)b is assumed to obey an additive decomposition into elastic and inelastic components, more generally referred to as eigenstrains μ^{ζ}_{kl}, which is summation of various eigenstrains types $\mu^{I\zeta}_{kl}(\boldsymbol{x})$, such as inelastic deformation, thermal change, moisture effects, etc. The traction boundary conditions govern the traction continuity along the interface of fine-scale constituents denoted by S^{ζ}; the $+/-$ signs indicate the two sides of the interface. δ_i^{ζ} is the displacement jump (or so-called eigen-separation) along the interface and $[\![\cdot]\!]$ is the jump operator.

In the double scale mathematical homogenization the response fields are assumed to depend on the coarse-scale position vector x in the coarse-scale domain Ω and fine-scale position vector y in the unit cell domain Θ. The displacement field $u_i^{\zeta}(x) = u_i(x,y)$ is approximated in terms of double-scale asymptotic expansions on $\Omega \times \Theta$ as

$$u_i^{\zeta}(x) = u_i^{(0)}(x,y) + \zeta u_i^{(1)}(x,y) + O\left(\zeta^2\right) \tag{2.3}$$

It is *a priori* assumed for nonlinear problems that the first term in asymptotic expansion of displacements does not depend on the fine-scale coordinates.

$$u_i^{(0)}\left(x\right) = u_i^c\left(x\right) \tag{2.4}$$

Thus equation (2.3) can be rewritten as

$$u_i^{\zeta}(x) \equiv u_i(x,y) = \underbrace{u_i^c(x)}_{u_i^{(0)}(x)} + \zeta u_i^{(1)}(x,y) + O\left(\zeta^2\right) \tag{2.5}$$

Likewise the asymptotic expansion of the strain field is obtained by substituting equation (2.3) into equation (2.2)c and making use of the chain rule in equation (2.1)

$$\varepsilon_{ij}^{\zeta}(x) = \frac{1}{\zeta}\varepsilon_{ij}^{(-1)}(x,y) + \varepsilon_{ij}^{(0)}(x,y) + \zeta\varepsilon_{ij}^{(1)}(x,y) + O\left(\zeta^2\right) \tag{2.6}$$

where various orders of strain are defined as

$$\begin{aligned} \varepsilon_{ij}^{(-1)} &= u_{(i,y_j)}^{(0)} \\ \varepsilon_{ij}^{(s)} &= u_{(i,x_j)}^{(s)} + u_{(i,y_j)}^{(s+1)} \quad s = 0,1... \end{aligned} \tag{2.7}$$

The subscript parentheses denote the symmetric gradients of the displacements. Following (2.7) (a) the asymptotic expansion in (2.6) can be restated as

$$\begin{aligned} \varepsilon_{ij}^{\zeta}(x) &= \varepsilon_{ij}^{(0)}(x,y) + \zeta\varepsilon_{ij}^{(1)}(x,y) + O\left(\zeta^2\right) \\ &= u_{(i,x_j)}^{(0)}(x) + u_{(i,y_j)}^{(1)}(x,y) + \zeta\varepsilon_{ij}^{(1)}(x,y) + O\left(\zeta^2\right) \\ &= \underbrace{\varepsilon_{ij}^{c} + u_{(i,y_j)}^{(1)}(x,y)}_{\varepsilon_{ij}^{f}(x,y)} + \zeta\varepsilon_{ij}^{(1)}(x,y) + O\left(\zeta^2\right) \end{aligned} \tag{2.8}$$

The stresses and strains for different orders of ζ are related by the constitutive relation in equation (2.2)(c). The two scale asymptotic expansion of the stress field is given by

$$\sigma_{ij}^{\zeta}(x) \equiv \sigma_{ij}(x,y) = \underbrace{\sigma_{ij}^{(0)}(x,y)}_{\sigma_{ij}^{f}(x,y)} + \zeta\sigma_{ij}^{(1)}(x,y)) + O\left(\zeta^2\right) \tag{2.9}$$

The eigenstrain $\mu_{ij}^{\zeta} \equiv \mu_{ij}^{\zeta}(\varepsilon^{\zeta}, \sigma^{\zeta}, s^{\zeta})$ depends on constitutive behavior of fine-scale constituents, and can be expressed in term of state variables s_i^{ζ}, strain and/or stress. Expanding eigenstrain in Taylor series around the leading order fields yields

$$\begin{aligned} \mu_{ij}^{\zeta} &\equiv \mu_{ij}(\varepsilon^{(0)}, \sigma^{(0)}, s^{(0)}) + \zeta\left(\frac{\partial\mu_{ij}^{\zeta}}{\partial\varepsilon_{kl}^{\zeta}}\varepsilon_{kl}^{(1)} + \frac{\partial\mu_{ij}^{\zeta}}{\partial\sigma_{kl}^{\zeta}}\sigma_{kl}^{(1)} + \frac{\partial\mu_{ij}^{\zeta}}{\partial s_k^{\zeta}}s_k^{(1)}\right) + O\left(\zeta^2\right) \\ &= \mu_{ij}^{f} + \zeta\mu_{ij}^{(1)} + O\left(\zeta^2\right) \end{aligned} \tag{2.10}$$

By substituting the asymptotic expansions in equation (2.5) to (2.9) in to the equilibrium equation (2.2) and enforcing the chain rule (2.1), yields equilibrium equations of various orders in ζ

$$O(\zeta^{-1}): \quad \sigma^{f}_{ij,y_j} = 0 \tag{2.11}$$

$$O(1): \quad \sigma^{c}_{ij,x_j} + b^{c}_{i} = 0 \tag{2.12}$$

The coarse-scale fields are defined as an average of the leading order (or fine-scale) fields computed over the unit cell domain as

$$\begin{aligned} \sigma^{c}_{ij} &= \frac{1}{|\Theta|}\int_{\Theta} \sigma^{f}_{ij}\, d\Theta; \quad b^{c}_{i} = \frac{1}{|\Theta|}\int_{\Theta} b^{\zeta}_{i}\, d\Theta \\ \overline{t}^{c}_{i} &= \frac{1}{|\partial\omega|}\int_{\partial\omega} \overline{t}^{\zeta}_{i}\, ds; \quad \overline{u}^{c}_{i} = \frac{1}{|\partial\omega|}\int_{\partial\omega} \overline{u}^{\zeta}_{i}\, ds \end{aligned} \tag{2.13}$$

Inserting the strain asymptotic expansion in equation (2.8) into the governing equation of the unit cell problem in equation (2.11) yields

$$\begin{aligned} &\varepsilon^{f}_{kl}(x,y) = \varepsilon^{c}_{kl}(x) + u^{(1)}_{(k,y_l)}(x,y) \\ &\sigma^{f}_{ij}(x,y) = L_{ijkl}(y)\underbrace{\left(\varepsilon^{f}_{kl}(x,y) - \mu^{f}_{kl}(x,y)\right)}_{\varepsilon^{f-el}_{kl}} \\ &\sigma^{f}_{ij,y_j} = 0 \end{aligned} \tag{2.14}$$

subjected to periodicity condition. The coarse-scale stress then follows from equations (2.13) and (2.14)

$$\sigma^{c}_{ij}(x) = \frac{1}{|\Theta|}\int_{\Theta} L_{ijkl}(y)\left(\varepsilon^{c}_{kl}(x) + u^{(1)}_{k,y_l}(x,y) - \mu^{f}_{kl}(x,y)\right) d\Theta \tag{2.15}$$

2.2.1 Residual-Free Fields and Model Reduction

The two scale spatial homogenization theory for nonlinear history dependent problems formulated in section 2.2 referred to as “Direct Homogenization” hereafter is computationally prohibitive. To illustrate the computational cost, consider a two scale problem with n_{el} elements, n_{gp} gauss points per element, n_{load} increments, I_{coarse} and I_{fine} number of average iterations at the coarse scale and fine scale respectively, then the total number of linear solutions of the fine scale problem is $n_{el} * n_{gp} * n_{load} ** I_{coarse} * I_{fine}$. This is a formidable task in terms of the computational cost involved and therefore the method has not been able to find much industrial applications. The prohibitive cost involved with the direct homogenization has been effectively addressed by parallel computing and by the introduction of meso-mechanical models as shown in Figure 3.

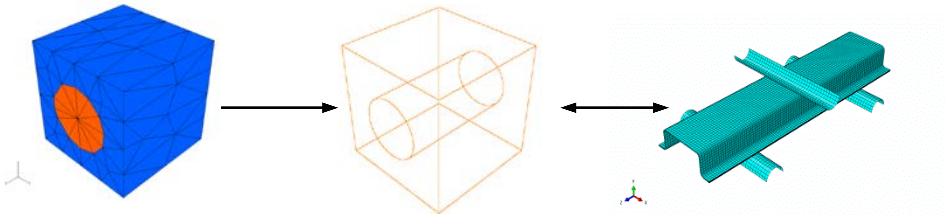

fine-scale model meso-scale model coarse-scale model

Figure 3: Illustration of a reduced order model

A review of literature highlights the following reduced order modeling methods: Voronoi cell method [36], the spectral method[37], the network approximation method [38], the Fast Fourier Transforms[39, 40], the Lattice Discrete Particle Model (LDPM)[41, 42], the Transformation Field Analysis (TFA)[30, 43] and methods based on control theory including balanced truncation [44, 45], optimal Hankel norm approximation [46], and proper orthogonal decomposition [47].

In this section the focus is on a variant of the TFA method [12, 29, 48, 49] that has found prominence in the recent years. The highlight of this method involves computation of certain localization operators, concentration tensors, transformation influence functions prior to the nonlinear two scale analysis. These localization operators/concentration tensors/influence functions account for the influence of the fine scale eigenstrains and eigen-separations on the coarse scale response by solving a series of linear elastic BVPs. However the method lacks a rigorous mathematical framework, is not hierarchical, cannot account for interface failure and is limited to a two scale framework only.

The reduced order homogenization [33, 35, 50-52] is an extension of the TFA methodology and overcomes the shortcomings mentioned above. The main characteristics of the reduced order homogenization method are enumerated below

(vii) The method accounts for failure at the interfaces where the separations at the interface is modeled as eigenseparations a concept that is analogous to eigenstrains.

(viii) It is equipped with model improvement capabilities that allow a hierarchical arrangement of discretization of the microstructure. The least expensive model in this hierarchy involves a discretization that assumes uniform deformation in each of the phases comprising the unit cell. On the other hand the most expensive model in this hierarchy coincides with the discretization involving the direct homogenization method.

(ix) Like the TFA, this methodology also involves construction of residual free fields. This unique feature allows the $n_{el} * n_{gp} * n_{load} ** I_{coarse} * I_{fine}$ solutions of the unit cell equilibrium equations to be satisfied *a priori* during the preprocessing phase.

The fine scale displacement field $u_i^{(1)}(x,y)$ is constructed as a function of the coarse coordinate x and fine scale coordinate y as in the method of separation of variables:

$$u_i^{(1)}(x,y) = H_i^{kl}(y)\varepsilon_{kl}^c(x) + \int_\Theta \tilde{h}_i^{kl}(y,\tilde{y})\, \mu_{kl}^f(x,\tilde{y})d\tilde{\Theta} + \int_S \breve{h}_i^{\breve{n}}(y,\breve{y})\, \delta_{\breve{n}}^f(x,\breve{y})d\breve{S} \qquad (2.16)$$

where H_i^{kl}, $\tilde{h}_i^{kl}$, and $\breve{h}_i^{\breve{n}}$ are the influence functions for coarse-scale strain, fine-scale eigenstrain, and fine-scale eigen-separation, respectively.

The above formulation for the fine scale displacements is constructed such that the stress fields in the unit cell satisfy the fine scale equilibrium equation for arbitrary coarse scale strains ε_{kl}^c, eigenstrains μ_{ij}^f and eigen-separations $\delta_{\hat{n}}^f$

Substituting the above formulation (2.16) in equation (2.14) gives the fine-scale equilibrium equation as

$$\left(L_{ijkl}(y) \left(\begin{gathered} \left(I_{klmn} + H_{(k,y_l)}^{mn} \right)\varepsilon_{mn}^c(x) + \left(\int_\Theta \tilde{h}_{(k,y_l)}^{mn}(y,\tilde{y})\, \mu_{mn}^f(x,\tilde{y})d\tilde{\Theta} - \mu_{kl}^f(x,y) \right) \\ + \int_S \breve{h}_{(k,y_l)}^{\breve{n}}(y,\hat{y})\, \delta_{\breve{n}}^f(x,\breve{y})d\breve{S} \end{gathered} \right) \right)_{,y_j} = 0 \qquad (2.17)$$

Model reduction is introduced by discretizing eigenstrains $\mu_{kl}^f(\boldsymbol{x},\boldsymbol{y})$ and eigen-separations $\delta_{\breve{n}}^f(x,y)$ using a point collocation approach discretization as illustrated in the following equations

$$\begin{aligned} &\mu_{kl}^f(x,\tilde{y}) = a_{kl}(x)d\left(y - \tilde{y}\right) \quad \tilde{y} \in \Theta \\ &\delta_{\breve{n}}^f = b_{\breve{n}}(x)d\left(y - \breve{y}\right) \quad \breve{y} \in S \end{aligned} \qquad (2.18)$$

where $d\left(y - \breve{y}\right)$ and $d\left(y - \tilde{y}\right)$ are the Dirac delta function in the unit cell domain and at the interfaces of fine-scale phases, respectively.

Substituting (2.18) into (2.17) and requiring arbitrariness of the coarse scale strain $\varepsilon_{kl}^{c}(x)$ and the coefficients in (2.18) yields the following influence function equations for the displacement field, the eigenstrain and eigen-separation.

$$\begin{aligned}
&\left\{L_{ijkl}(y)\left[I_{klmn}+H_{(k,y_l)}^{mn}(y)\right]\right\}_{,y_j}=0\\
&\left\{L_{ijkl}(y)\left[\tilde{h}_{(k,y_l)}^{mn}(y,\tilde{y})-I_{klmn}d(y-\tilde{y})\right]\right\}_{,y_j}=0\\
&\left\{L_{ijkl}(y)h_{(k,y_l)}^{\breve{n}}(y,\breve{y})\right\}_{,y_j}=0
\end{aligned}\tag{2.19}$$

Equations in (2.19) represent a set of elastic boundary value problems which can be solved during the preprocessing phase. Analytical solutions for the above boundary value problems for complex microstructures are generally unknown. Finite element analysis of these boundary value problems with point colocation discretization is not cost effective either. The alternate approach is to use the subdomain collocation approach for discretization of eigenstrains and eigen-separations as shown below

$$\begin{aligned}
&\mu_{ij}^{f}(x,y)=\sum_{\alpha=1}^{n}\tilde{N}^{(\alpha)}(y)\mu_{ij}^{(\alpha)}(x);\\
&\delta_{\breve{n}}^{f}(x,y)=\sum_{\xi=1}^{m}\breve{N}^{(\xi)}(y)\delta_{\breve{n}}^{(\xi)}(x)
\end{aligned}\tag{2.20}$$

where n and m denote the number of partitions of phases and interfaces respectively; $\mu_{ij}^{(\alpha)}$ and $\delta_{\breve{n}}^{(\xi)}$ denote the average eigenstrains and eigen-separations in phase partition $\Theta^{(\alpha)}$ and interface partition $S^{(\xi)}$, respectively. This allows having a hierarchical sequence of unit cell homogenization models, where a model that assumes one partition per element will incur computational cost associated with direct homogenization, while an assumption of uniform deformation in each of the phases will lead to a model with one partition per phase with maximum computational efficiency.

The shape functions $\tilde{N}^{(\alpha)}(y)$ for eigenstrain are chosen to be $C^{-1}(\Theta)$ functions as the eigenstrains need to satisfy the condition of continuity. The eigen-separation shape functions are chosen to be $C^{0}(S)$ functions as the cracks (displacement jumps) need to be continuous across the interfaces. Additionally the shape functions need to satisfy the partition of unity condition.

$$\sum_{\alpha=1}^{n_l} \tilde{N}^{(\alpha)}(y) = 1 \;\; ; \; \sum_{\xi=1}^{m} \breve{N}^{(\xi)}(y) = 1 \tag{2.21}$$

The average eigenstrains and eigen-separations are defined as

$$\begin{aligned} \mu_{ij}^{(\alpha)} &= \int_{\Theta} \tilde{\varphi}^{(\alpha)} \mu_{ij}^{f} \, d\Theta \\ \delta_{\breve{n}}^{(\xi)} &= \int_{S} \breve{\varphi}^{(\zeta)} \delta_{\hat{n}}^{f} \, dS \end{aligned} \tag{2.22}$$

The weight functions $\tilde{\varphi}^{(\alpha)}$ and $\breve{\varphi}^{(\zeta)}$ should satisfy the condition of positivity and normalization.

$$\begin{aligned} &\tilde{\varphi}^{(\alpha)} > 0 \;\; ; \; \breve{\varphi}^{(\zeta)} > 0 \\ &\sum_{\alpha=1}^{n} \tilde{\varphi}^{(\alpha)}(y) = 1 \;\; ; \; \sum_{\xi=1}^{m} \breve{\varphi}^{(\xi)}(y) = 1 \end{aligned} \tag{2.23}$$

A piecewise constant approximation for the eigenstrain and eigenseparation shape functions and weight functions satisfies the conditions in equations (2.21) and (2.23)

$$\begin{aligned} &\tilde{N}^{(\alpha)}(y) = \begin{cases} 1 & y \in \Theta^{(\alpha)} \\ 0 & y \in \Theta^{(\alpha)} \end{cases}, \quad \tilde{\varphi}^{(\alpha)}(y) = \tilde{N}^{(\alpha)}(y) / \left| \Theta^{(\alpha)} \right| \\ &\breve{N}^{(\xi)}(y) = \begin{cases} \sum\limits_{A \in S^{(\xi)}} N_{A}^{f}(y) & y \in S^{(\xi)} \\ 0 & y \notin S^{(\xi)} \end{cases}, \quad \breve{\varphi}^{(\zeta)}(y) = \begin{cases} 1 / \left| S^{(\zeta)} \right| & if \quad y \in S^{(\beta)} \\ 0 & elsewhere \end{cases} \end{aligned} \tag{2.24}$$

Substituting the above discretization in (2.20),(2.22) and (2.24) into (2.17) and requiring the unit cell equilibrium to be satisfied for arbitrary $\varepsilon_{kl}^{c}(x)$, $\mu_{ij}^{(\alpha)}$ and $\delta_{\breve{n}}^{(\xi)}$ yields the following strong form of the influence functions for the fine scale displacements, eigenstrains and eigenseparations

$$\begin{aligned}
&\left\{L_{ijkl}(y)\left[I_{klmn}+H_{(k,y_l)}^{mn}(y)\right]\right\}_{,y_j}=0\\
&\left\{L_{ijkl}(y)\left[P_{kl}^{mn(\alpha)}(y)-I_{klmn}^{(\alpha)}(y)\right]\right\}_{,y_j}=0\\
&\left\{L_{ijkl}(y)Q_{kl}^{\breve{n}(\xi)}(y)\right\}_{,y_j}=0\ \ with\ \ \delta_{\breve{n}}^{f}(\hat{y})=\breve{N}^{(\xi)}(\hat{y})
\end{aligned}\tag{2.25}$$

where

$$\begin{aligned}
&P_{ij}^{mn(\alpha)}(y)=\int_{\Theta^{(\alpha)}}\tilde{h}_{(i,y_j)}^{mn}(y,\tilde{y})\,d\tilde{\Theta}\\
&Q_{ij}^{\breve{n}(\xi)}(y)=\int_{S}\breve{h}_{(i,y_j)}^{\breve{n}}(y,\hat{y})\,\breve{N}^{(\xi)}(\breve{y})\,d\breve{S}
\end{aligned}\tag{2.26}$$

2.2.2 Reduced Order System of Equations

The main feature of the reduced order two scale homogenization frame work discussed in section 2.3 is that it allows pre-computing of the influence functions in equation (2.19) prior to the two scale nonlinear analysis. Therefore, each iteration of the coarse scale nonlinear analysis will involve computation of the fine scale strains, eigen-fields, updating of fine scale stresses and coarse scale stresses. The reduced order system of equations comprise of the following

(i) Reduced order equations for residual-free strain fields at the fine scale

(ii) Reduced order equations for traction continuity along the interfaces of the fine scale phases

(iii) Reduced order equations for the fine scale eigen-fields

The residual-free strain field is obtained by substituting (2.16) into (2.14)a

$$\varepsilon_{ij}^{f}(x,y)=E_{ij}^{kl}\left(y\right)\varepsilon_{kl}^{c}(x)+\int_{\Theta}\tilde{h}_{\left(i,y_j\right)}^{kl}(y,\tilde{y})\;\mu_{kl}^{f}(x,\tilde{y})d\tilde{\Theta}+\int_{S}\breve{h}_{\left(i,y_j\right)}^{\breve{n}}(y,\breve{y})\;\delta_{\breve{n}}^{f}(x,\breve{y})d\breve{S} \tag{2.27}$$

where

$$E_{ij}^{kl}=I_{ijkl}+H_{\left(i,y_j\right)}^{kl} \tag{2.28}$$

Substituting the discretization in equation (2.20) into equation (2.27) yields

$$\varepsilon_{ij}^{f}(x,y)=E_{ij}^{kl}\left(y\right)\varepsilon_{kl}^{c}(x)+\sum_{\alpha=1}^{n}P_{ij}^{kl(\alpha)}\left(y\right)\mu_{kl}^{(\alpha)}(x)+\sum_{\xi=1}^{m}Q_{ij}^{\breve{n}(\xi)}\left(y\right)\;\delta_{\breve{n}}^{(\xi)}(x) \tag{2.29}$$

Averaging the residual-free strain field over partition domain $\Theta^{(\beta)}$ yields

$$\varepsilon_{ij}^{(\beta)}(x)-\sum_{\alpha=1}^{n}P_{ij}^{kl(\beta\alpha)}\;\mu_{kl}^{(\alpha)}(x)-\sum_{\xi=1}^{m}Q_{ij}^{\breve{n}(\beta\xi)}\;\delta_{\breve{n}}^{(\xi)}(x)=E_{ij}^{kl(\beta)}\varepsilon_{kl}^{c}(x) \tag{2.30}$$

where

$$*^{(\beta)}\equiv\frac{1}{\left|\Theta^{(\beta)}\right|}\int_{\Theta^{(\beta)}}*d\Theta \tag{2.31}$$

Likewise the reduced order residual free fine-scale traction $t_{\breve{n}}^{(\eta)}$ along the interface is obtained by averaging $\sigma_{ij}^{f}\breve{n}_j$ over the interface partition

$$-\sum_{\alpha=1}^{n}C_{\breve{n}}^{kl(\eta\alpha)}\mu_{kl}^{(\alpha)}(x)+t_{\breve{n}}^{(\eta)}(x)-\sum_{\xi=1}^{m}D_{\breve{n}}^{\breve{m}(\eta\xi)}\delta_{\breve{m}}^{(\xi)}(x)=T_{\breve{n}}^{kl(\eta)}\varepsilon_{kl}^{c}(x) \tag{2.32}$$

where

$$\begin{aligned} C_{\hat{m}}^{kl(\alpha)} &= a_{\hat{m}i} L_{ijpq}(y)\left[P_{pq}^{kl(\alpha)}(y) - I_{pqkl}^{(\alpha)} \right] \hat{n}_j(y) \\ D_{\hat{m}\hat{n}}^{(\xi)} &= a_{\hat{m}i} L_{ijpq}(y) Q_{pq}^{\breve{n}(\xi)}(y) \breve{n}_j(y) \\ T_{\hat{m}}^{kl} &= a_{\hat{m}i} L_{ijpq}(y) E_{pq}^{kl}(y) \breve{n}_j(y) \\ *^{(\eta)} &\equiv \frac{1}{\left| S^{(\eta)} \right|} \int_{S^{(\eta)}} * dS \end{aligned} \tag{2.33}$$

The reduced order constitutive relations for eigenstrains and eigenseparations are given as

$$\mu_{ij}^{(\alpha)}(x) = f\left(\varepsilon_{ij}^{(\alpha)}(x) \right); \quad t_{\breve{n}}^{(\eta)}(x) = g\left(\delta_{\breve{n}}^{(\eta)}(x) \right) \tag{2.34}$$

Equations (2.30), (2.32) and (2.34) comprise a reduced order system of nonlinear equations for independent unknowns $\varepsilon_{ij}^{(\alpha)}(\boldsymbol{x})$ and $\delta_{\breve{n}}^{(\xi)}(\boldsymbol{x})$. Finally, the reduced order form for the coarse-scale stress is obtained by integrating σ_{ij}^{f} over unit cell domain, which yields

$$\sigma_{ij}^{c}(x) = L_{ijkl}^{c} \varepsilon_{kl}^{c}(x) + \sum_{\alpha=1}^{n} A_{ijkl}^{c(\alpha)} \, \mu_{kl}^{(\alpha)}(x) + \sum_{\xi=1}^{m} B_{ij\breve{n}}^{c(\xi)} \, \delta_{\breve{n}}^{(\xi)}(x) \tag{2.35}$$

where

$$\begin{aligned} L_{ijkl}^{c} &= \frac{1}{|\Theta|} \int_{\Theta} L_{ijmn}(y) E_{mn}^{kl}(y) \, d\Theta \\ A_{ijkl}^{c(\alpha)} &= \frac{1}{|\Theta|} \int_{\Theta} L_{ijmn}(y) \left[P_{mn}^{kl(\alpha)}(y) - I_{mnkl}^{(\alpha)} \right] d\Theta \\ B_{ij\breve{n}}^{c(\xi)} &= \frac{1}{|\Theta|} \int_{\Theta} L_{ijmn}(y) Q_{mn}^{\breve{n}(\xi)}(y) \, d\Theta \end{aligned} \tag{2.36}$$

Equation (2.35) can be rearranged by defining coarse-scale eigenstrain $\mu_{kl}^{c}(x)$

$$\mu_{kl}^{c}(x) = \sum_{\alpha=1}^{n} \left(-M_{ijkl}^{c} A_{ijmn}^{c(\alpha)} \right) \mu_{mn}^{(\alpha)}(x) + \sum_{\xi=1}^{m} \left(-M_{ijkl}^{c} B_{ij\breve{n}}^{c(\xi)} \right) \delta_{\breve{n}}^{(\xi)}(x) \tag{2.37}$$

which yields a coarse-scale constitutive equation having a similar structure to that of fine-scale constitutive equation

$$\sigma_{ij}^{c}(x) = L_{ijkl}^{c}\left(\varepsilon_{kl}^{c}(x) - \mu_{kl}^{c}(x)\right) \tag{2.38}$$

In summary, in the preprocessing stage prior to nonlinear coarse-scale analysis the influence problems (2.25) are solved and the coefficient tensors (2.31), (2.33) and (2.36) are calculated. At each iteration of nonlinear coarse-scale analysis, the eigenstrains and eigen-separations are updated by solving the reduced-order unit cell system(2.30), (2.32) and(2.34). Finally, the-coarse scale stress is updated using(2.35).

2.3 Numerical Implementation

This section discusses the aspects of numerical implementation of the reduced order homogenization and its integration into conventional finite element code architecture by utilizing the functionality of user-defined material interfaces. The reduced order formulation detailed in the previous section is recast into a form that allows addition of user defined materials models. The primary step of the numerical implementation phase involves solution of the nonlinear equations in (2.30) and (2.32). The equations are solved using Newton's method by defining the unit cell residual in the following form

$$r^{(\beta,\eta)} \equiv r\left(\Delta\varepsilon_{ij}^{(\beta)}, \Delta\delta_{\hat{n}}^{(\eta)}\right) = \begin{bmatrix} \Delta\varepsilon_{ij}^{(\beta)} - \sum\limits_{\gamma=1}^{n} P_{ij}^{kl(\beta\gamma)} \Delta\mu_{kl}^{(\gamma)} - \sum\limits_{\tau=1}^{m} Q_{ij}^{\hat{n}(\beta\tau)} \Delta\delta_{\hat{n}}^{(\tau)} - E_{ij}^{kl(\beta)} \Delta\varepsilon_{kl}^{c} \\ -\sum\limits_{\gamma=1}^{n} C_{\hat{n}}^{kl(\eta\gamma)} \Delta\mu_{kl}^{(\gamma)} + \Delta t_{\hat{n}}^{(\eta)} - \sum\limits_{\tau=1}^{m} D_{\hat{n}}^{\breve{m}(\eta\tau)} \Delta\delta_{\breve{m}}^{(\tau)} - T_{\hat{n}}^{kl(\eta)} \Delta\varepsilon_{kl}^{c} \end{bmatrix} = 0 \tag{2.39}$$

The unknowns are the increments of fine scale phase strain fields $\Delta\varepsilon_{ij}^{(\beta)}$ and eigen-separations $\Delta\delta_{\hat{n}}^{(\tau)}$, whereas the coarse-scale strain ${}_{n+1}^{i+1}\Delta\varepsilon_{kl}^{c}$ is prescribed by the coarse-scale problem at every load increment *n+1* and iteration *i+1*. The solution of the nonlinear system of equation in (2.30) and (2.32) using Newton's method requires function derivatives with respect to the variable $\theta^{(\alpha,\zeta)} \equiv \left\{ \Delta\varepsilon_{kl}^{(\alpha)}, \Delta\delta_{\hat{m}}^{(\xi)} \right\}$ at every load increment and iteration of the coarse scale nonlinear problem analysis.

$$\frac{\partial r^{(\beta,\eta)}}{\partial \theta^{(\alpha,\xi)}} = \left| \begin{matrix} \delta_{\beta\alpha} I_{ijkl} - \sum_{\gamma=1}^{n} P_{ij}^{kl(\beta\alpha)} \dfrac{\partial \Delta\mu_{mn}^{(\alpha)}}{\partial \Delta\varepsilon_{kl}^{(\alpha)}} \delta_{\alpha\gamma} - \sum_{\tau=1}^{m} Q_{ij}^{\breve{n}(\beta\xi)} \delta_{\tau\xi} \\ - \sum_{\gamma=1}^{n} C_{\hat{n}}^{kl(\eta\alpha)} \dfrac{\partial \Delta\mu_{mn}^{(\alpha)}}{\partial \Delta\varepsilon_{kl}^{(\alpha)}} \delta_{\alpha\gamma} + \delta_{\eta\xi} \dfrac{\partial \Delta t_{\breve{n}}^{(\xi)}}{\partial \Delta\bar{\delta}_{\breve{m}}^{(\xi)}} - \sum_{\tau=1}^{m} D_{\breve{n}}^{\breve{m}(\eta\xi)} \delta_{\tau\xi} \end{matrix} \right.$$

$$\left| \begin{matrix} \delta_{\beta\alpha} I_{ijkl} - P_{ij}^{kl(\beta\alpha)} \dfrac{\partial \Delta\mu_{mn}^{(\alpha)}}{\partial \Delta\varepsilon_{kl}^{(\alpha)}} - -Q_{ij}^{\breve{n}(\beta\xi)} \\ -C_{\hat{n}}^{kl(\eta\alpha)} \dfrac{\partial \Delta\mu_{mn}^{(\alpha)}}{\partial \Delta\varepsilon_{kl}^{(\alpha)}} + -C_{\hat{n}}^{kl(\eta\alpha)} \dfrac{\partial \Delta\mu_{mn}^{(\alpha)}}{\partial \Delta\varepsilon_{kl}^{(\alpha)}} \end{matrix} \right. \tag{2.40}$$

In the above equation δ_{ij} is Kronecker Delta. The derivative of the eigenstrains with respect to the phase strain can be computed from

$$\begin{aligned} \Delta\mu_{ij}^{(\alpha)} &= \Delta\varepsilon_{ij}^{(\alpha)} - M_{ijkl}^{(\alpha)} \Delta\sigma_{kl}^{(\alpha)} \\ \frac{\partial \Delta\mu_{ij}^{(\alpha)}}{\partial \Delta\varepsilon_{kl}^{(\alpha)}} &= I_{ijkl} - M_{ijmn}^{(\alpha)} \frac{\partial \Delta\sigma_{mn}^{(\alpha)}}{\partial \Delta\varepsilon_{kl}^{(\alpha)}} \end{aligned} \tag{2.41}$$

where $M_{ijkl}^{(\alpha)}$ is elastic compliance tensor for phase partition α and $\dfrac{\partial \Delta\sigma_{mn}^{(\alpha)}}{\partial \Delta\varepsilon_{kl}^{(\alpha)}}$ is the consistent tangent stiffness for the corresponding phase. The derivatives $\dfrac{\partial \Delta\mu_{ij}^{(\alpha)}}{\partial \Delta\varepsilon_{kl}^{(\alpha)}}$ and $\dfrac{\partial \Delta t_{\breve{n}}^{(\xi)}}{\partial \Delta\delta_{\breve{m}}^{(\xi)}}$ in equation (2.40) can also be computed by utilizing the constitutive relations for the phases and the interfaces as given in equation (2.34).

Once the unknowns $\theta^{(\alpha,\xi)} \equiv \left\{ \Delta\varepsilon_{kl}^{(\alpha)}, \Delta\delta_{\breve{m}}^{(\xi)} \right\}$ are solved, the phase eigenstrains are updated using the constitutive behavior defined in equation (2.34)(a). Finally the coarse scale stress is computed using equation (2.35) rewritten below for convenience

$$\sigma_{ij}^{c}(\boldsymbol{x}) = L_{ijkl}^{c}\varepsilon_{kl}^{c}(\boldsymbol{x}) + \sum_{\alpha=1}^{n} A_{ijkl}^{c(\alpha)}\,\mu_{kl}^{(\alpha)}(\boldsymbol{x}) + \sum_{\xi=1}^{m} B_{ij\breve{n}}^{c(\xi)}\,\delta_{\breve{n}}^{(\xi)}(\boldsymbol{x}) \tag{2.42}$$

Analysis of nonlinear problems with implicit solvers necessitates the computation of the coarse scale tangent stiffness tensor. The derivation of the coarse scale consistent tangent tensor is described in the ensuing paragraphs.

The derivative of the coarse scale stress σ_{ij}^{c} in equation (2.42) with respect to coarse scale strain ε_{kl}^{c} is as given below

$$\frac{\partial\Delta\sigma_{ij}^{c}}{\partial\Delta\varepsilon_{kl}^{c}} = L_{ijkl}^{c} + \sum_{\alpha=1}^{n} A_{ijmn}^{c(\alpha)} \frac{\partial\Delta\mu_{mn}^{(\alpha)}}{\partial\Delta\varepsilon_{kl}^{c}} + \sum_{\xi=1}^{m} B_{ij\breve{n}}^{c(\xi)} \frac{\partial\Delta\delta_{\breve{n}}^{(\xi)}}{\partial\Delta\varepsilon_{kl}^{c}} \tag{2.43}$$

Using the chain rule the above equation can be restated as follows

$$\frac{\partial\Delta\sigma_{ij}^{c}}{\partial\Delta\varepsilon_{kl}^{c}} = L_{ijkl}^{c} + \sum_{\alpha=1}^{n} A_{ijmn}^{c(\alpha)} \frac{\partial\Delta\mu_{mn}^{(\alpha)}}{\partial\Delta\varepsilon_{pq}^{(\alpha)}} \boxed{\frac{\partial\Delta\varepsilon_{pq}^{(\alpha)}}{\partial\Delta\varepsilon_{kl}^{c}}} + \sum_{\xi=1}^{m} B_{ij\breve{n}}^{c(\xi)} \boxed{\frac{\partial\Delta\delta_{\breve{n}}^{(\xi)}}{\partial\Delta\varepsilon_{kl}^{c}}} \tag{2.44}$$

Computing the highlighted terms in the above equation will give us the necessary consistent tangent tensor. We proceed by taking the derivative of the reduced order system of equations in (2.30) and (2.32) with respect to the incremental coarse scale strain $\Delta\varepsilon_{kl}^{c}$, which yields

$$\begin{gathered} \frac{\partial\Delta\varepsilon_{ij}^{(\beta)}}{\partial\Delta\varepsilon_{kl}^{c}} - \sum_{\alpha=1}^{n} P_{ij}^{mn(\beta\alpha)} \frac{\partial\,\Delta\mu_{mn}^{(\alpha)}}{\partial\Delta\varepsilon_{kl}^{c}} - \sum_{\xi=1}^{m} Q_{ij}^{\breve{n}(\beta\xi)} \frac{\partial\Delta\delta_{\breve{n}}^{(\xi)}}{\partial\Delta\varepsilon_{kl}^{c}} = E_{ij}^{kl(\beta)} \\ -\sum_{\alpha=1}^{n} C_{\hat{n}}^{mn(\eta\alpha)} \frac{\partial\,\Delta\mu_{mn}^{(\alpha)}}{\partial\Delta\varepsilon_{kl}^{c}} + \frac{\partial\Delta t_{\breve{n}}^{(\eta)}}{\partial\Delta\varepsilon_{kl}^{c}} - \sum_{\xi=1}^{m} D_{\hat{n}}^{\breve{m}(\eta\xi)} \frac{\partial\Delta\delta_{\breve{m}}^{(\xi)}}{\partial\Delta\varepsilon_{kl}^{c}} = T_{\breve{n}}^{kl(\eta)} \end{gathered} \tag{2.45}$$

Again using chain rule the above equation can be simplified to the following linear system of equations

$$\begin{gathered}\sum_{\alpha=1}^{n}\left(\delta_{\beta\alpha} I_{ijpq} - \sum_{\alpha=1}^{n} P_{ij}^{mn(\beta\alpha)} \frac{\partial\Delta\mu_{mn}^{(\alpha)}}{\partial\Delta\varepsilon_{pq}^{(\alpha)}}\right)\boxed{\frac{\partial\Delta\varepsilon_{pq}^{(\alpha)}}{\partial\Delta\varepsilon_{kl}^{c}}} - \sum_{\xi=1}^{m} Q_{ij}^{\breve{m}(\beta\xi)} \boxed{\frac{\partial\Delta\delta_{\breve{m}}^{(\xi)}}{\partial\Delta\varepsilon_{kl}^{c}}} = E_{ij}^{kl(\beta)} \\ -\sum_{\alpha=1}^{n} C_{\hat{n}}^{mn(\eta\alpha)} \frac{\partial\Delta\mu_{mn}^{(\alpha)}}{\partial\Delta\varepsilon_{pq}^{(\alpha)}} \boxed{\frac{\partial\Delta\varepsilon_{pq}^{(\alpha)}}{\partial\Delta\varepsilon_{kl}^{c}}} + \sum_{\xi=1}^{m}\left(\delta_{\eta\xi}\frac{\partial\Delta t_{\breve{n}}^{(\xi)}}{\partial\Delta\delta_{\breve{m}}^{(\xi)}} - D_{\breve{n}}^{\breve{m}(\eta\xi)}\right)\boxed{\frac{\partial\Delta\delta_{\breve{m}}^{(\xi)}}{\partial\Delta\varepsilon_{kl}^{c}}} = T_{\breve{n}}^{kl(\eta)}\end{gathered} \tag{2.46}$$

The highlighted terms are computed by solving the linear system of equations in (2.46). Finally the coarse scale consistent tangent tensor is computed by using equation (2.44). A schematic representation of the numerical implementation of the two scale reduced order homogenization model is illustrated in Figure 4 below.

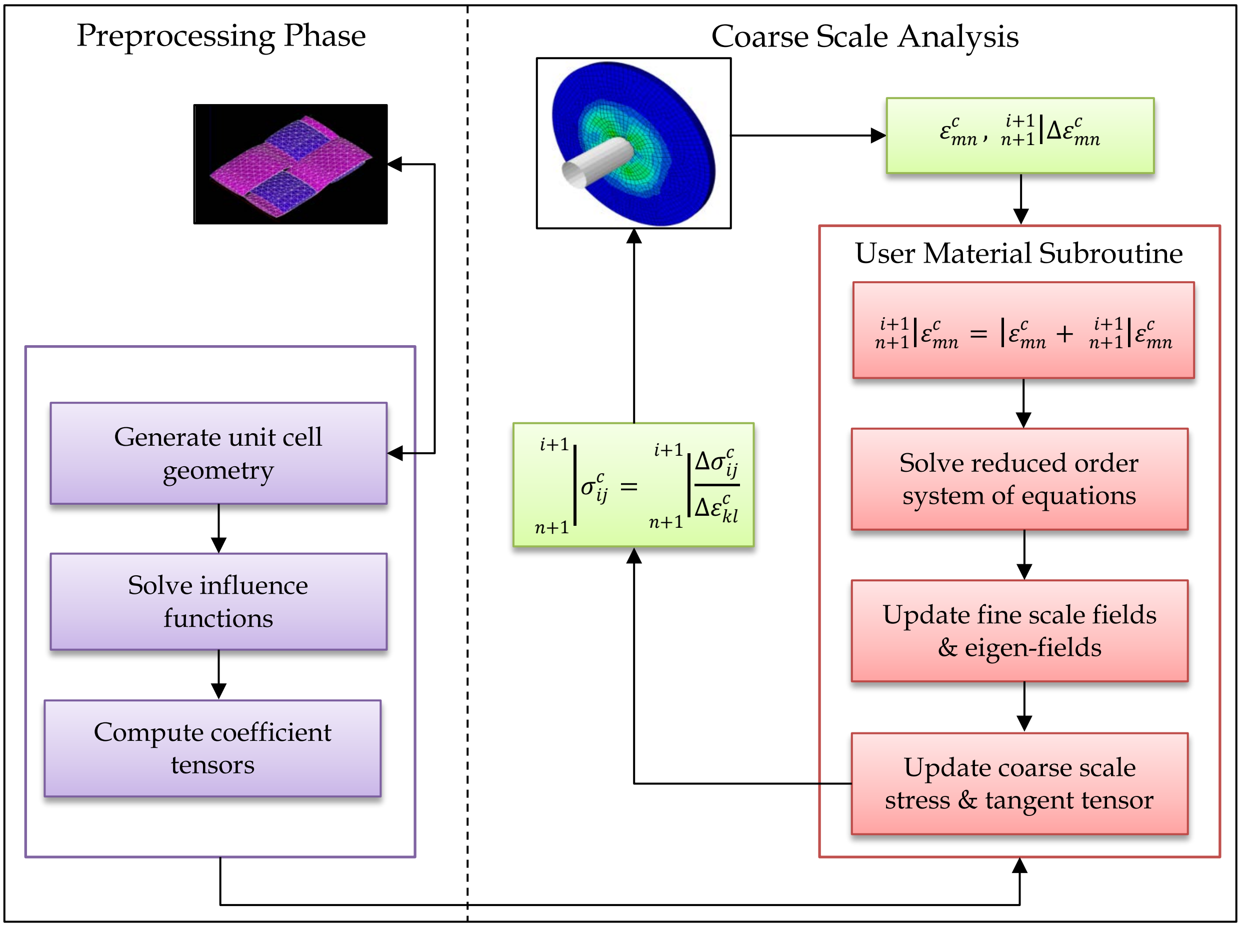
Preprocessing Phase
Coarse Scale Analysis
$\varepsilon^c_{mn},\ {}^{i+1}_{n+1}|\Delta\varepsilon^c_{mn}$
User Material Subroutine
${}^{i+1}_{n+1}|\varepsilon^c_{mn} = |\varepsilon^c_{mn} + {}^{i+1}_{n+1}|\varepsilon^c_{mn}$
Solve reduced order system of equations
Update fine scale fields & eigen-fields
Update coarse scale stress & tangent tensor
${}^{i+1}_{n+1}\Big|\sigma^c_{ij} = {}^{i+1}_{n+1}\Big|\frac{\Delta\sigma^c_{ij}}{\Delta\varepsilon^c_{kl}}$
Generate unit cell geometry
Solve influence functions
Compute coefficient tensors

Figure 4: Schematic of the two scale reduced order homogenization

PART III

RSA ALGORITHM

Chapter 3

Parametric Generation of Unit Cells with Randomly Distributed Inclusions

In this chapter the modified RSA algorithm is developed to generate unit cells for heterogeneous materials with randomly distributed inclusions of varying shapes and sizes. A statistical study aimed at understanding the effective size of the unit cell and its dependence on the relative properties of the phases comprising the unit cell is conducted. The inputs from co-authors of the paper (Bailakanavar et.al. [53]) from which the main sections in this chapter are reproduced are gratefully acknowledged.

3.1 Introduction

Identification and generation of unit cell geometry is a vital step (preprocessing phase) in the multiscale analysis of composite materials. Computational challenges in automatic generation of periodic microstructures, such as woven or fabric composites, have been by at large addressed (see for instance [54]). However, automatic generation of morphological details of materials with randomly distributed inclusions, such as defects in ceramics, hard and soft domains in polymers, chopped fiber composites etc. pose new challenges. Typical inclusions like ellipsoids, short fibers, platelets and discs found in heterogeneous materials are often of different shapes and sizes. Parameters influencing the unit cell geometry are the shape and size of the inclusion, the volume fraction and the morphological details like the spatial orientation and spatial distribution of the inclusions. Statistical data about such morphological details may be obtained from X-ray tomography, and 3D image analysis. The key challenges that need to be addressed when generating the random inclusion unit cells are:

(i) Accurate representation of the inclusion size and shape to minimize geometric approximation errors;

(ii) Generation of unit cells with packing fraction as high as 45%, typically found in industrial grade composite materials;

(iii) Determination of the unit cell size that constitutes a macroscopically homogeneous material;

(iv) Generation of unit cells in quick succession with maximum computational efficiency for utilization in a stochastic multiscale framework.

A literature review points out to two main approaches being used to generate unit cells with randomly distributed inclusions, namely the Concurrent Construction (CC) method [55-57] and the Random Sequential Adsorption (RSA) method [58-64]. The CC method is a two-step procedure. In the first step an initial configuration with an ordered packing of the inclusions is generated. In the second step these inclusions are perturbed in the phase space until the spatial orientation and distribution as observed in the statistical morphological data is achieved. The inclusions are not allowed to intersect or overlap as they reorient in the phase space. Duschlbauer et al. [57] used the CC method to generate short fiber composite unit cells with random orientations in 2D space. For a fiber aspect ratio (AR) of 10, they achieved a maximum of 21% fiber volume fraction without allowing any fiber intersections, which is about 75% of the maximum unforced packing limit for 2D random fibers [65].

Inclusions found in physical processes, such as burning of coal char, convective burning of porous explosives and regression of solid propellants, are often characterized by particular shapes, such as spheres, disks, spherocylinders and perforated rods. Lubachevsky and Stillinger [66] generated random packs of disks in 2D space by a concurrent construction algorithm. The inclusions start with random positions and velocities and they grow uniformly in size from a point in space to jammed disks as they move about in space. Stafford and Jackson [67] extended the Lubachevsky-Stillinger (LS) algorithm to create packs of non-spherical shapes for modeling heterogeneities in energetic materials like gun propellants.

In the RSA approach, a point in a given unit cell volume is randomly chosen and the first inclusion is placed with its center at the chosen position. Next, another point is randomly chosen from the diminished volume in the unit cell and the second inclusion is placed at this point. Likewise the process of sequentially and randomly positioning an inclusion is continued till the desired volume fraction is achieved or till the jamming limit is encountered. This method generates unit cells with non-intersecting inclusions wherein the gap between the inclusions is user-defined, typically of the order of inclusion size. The RSA algorithm have been employed for generating unit cells with various inclusions, including disks [68], spheres [69], ellipsoids [70] and spherocylinders [71]. Böhm et al. [59] modified the RSA algorithm to include user specified distance between adjacent inclusions to generate unit cells with cylindrical (AR=5) , sphero-cylindrical (AR=5) and spherical inclusions with inclusion volume fraction of 15%. Kari et al. [59] also used a modified RSA algorithm wherein the unit cells with cylindrical inclusions (AR=10) of up to a volume fraction of 25% were generated. For volume fractions greater than 25%, cylindrical inclusions with decreasing aspect ratios (AR<10) were gradually added after reaching the jamming limit. Pan et al. [64] used another variant of the modified RSA algorithm wherein a combination of straight and curved fibers (AR=20) were used to generate unit cells with fiber volume fraction of 35%.

Experimental study [72] of packing of short fibers in random orientation found that the packing fraction decreased rapidly with increasing aspect ratio of the rods. A theoretical study by Evans et al. [73] suggested that for fibers with AR>10, the fiber volume fraction should be proportional to the inverse aspect ratio, yielding a maximum fiber volume fraction of 20% for fibers with aspect ratio of 20. Likewise for fibers with aspect ratio of 20, Williams et al. [61]

reported a maximum volume fraction of 22%, while Parkhouse et al. [72] reported a volume fraction of 28%. Toll [65] reported a maximum achievable volume fraction of 18.5% for unforced fiber packing. Toll suggests that forced packing of fibers governed by bending of fibers at contact points is imperative for attaining higher fiber volume fractions. It is important to note that in all these estimates, fibers were considered to be straight and nonintersecting. Either of the methods mentioned above fails to generate unit cells with volume fractions as high as 45% found in various heterogeneous materials. A modified RSA algorithm by Pan et al. [64] can generate volume fractions of up to 35%. The algorithm is computationally expensive as it involves solving optimization problems to identify fiber intersection in 2D and 3D space. Additionally the algorithm is not robust and versatile to be implemented in a multiscale stochastic framework.

The research work presented in this chapter focusses on developing a parametric model for generating unit cells with randomly distributed inclusions. The proposed algorithm possesses superior robustness, computational efficiency and versatility compared to the previously developed RSA algorithms:

(i) robustness: it yields unit cells with fiber volume fraction of up to 45% for aspect ratios as high as 20;

(ii) efficiency: it consists of a hierarchy of algorithms with increasing computational complexity;

(ii) versatility: it generates unit cells with different inclusion shapes.

In Section 3.2 to 3.6 details of the proposed hierarchical RSA algorithm, hereafter to be referred to as HRSA, for various inclusions is presented. Section 3.7 presents a statistical study of stiffness and strength properties of randomly distributed chopped fiber composite aimed at determining the effective size of the unit cell. The HRSA algorithm has been applied to random inclusion microstructure composites including: (i) two-dimensional chopped tow composites in automotive applications, (ii) polyurea or polyethene coating consisting of hard and soft domains (segments) employed for energy absorption in military applications, and (iii) fiber framework called *fiberform* embedded in or free from an amorphous matrix used as heat shield on spacecraft to prevent structural damage during reentry into the atmosphere. A simple algorithm to minimize the geometric approximation and mesh discretization errors is presented in Section 3.8.

3.2 Hierarchical Random Sequential Adsorption (HRSA)

In this section a robust and computationally efficient unit cell generation algorithm for randomly distributed inclusions is presented. The two key features of the proposed HRSA algorithm are the capability to generate high packing fractions of up to 45% for inclusions with AR>10 and computational efficiency in generating unit cells in a quick succession. These two factors have not been addressed at tandem in the literature. These two objectives are accomplished by (i) forced packing aimed at achieving higher packing fractions followed by (ii) hierarchical inclusion generation strategy aimed at ensuring computational efficiency. The different levels in the HRSA algorithm are illustrated in Figure 5. A detailed flowchart of the HRSA algorithm is presented in Figure 12.

3.2.1 Unit Cell Geometry Definition

A set of independent user-defined model parameters along with dependent parameters uniquely define the unit cell geometry. The set of independent parameters is specific to the type of inclusion. The unit cell size is defined as a function of the inclusion's largest dimension. The Hierarchical Random Sequential Adsorption (HRSA) algorithm has been developed to include all possibilities of inclusion shapes found in heterogeneous materials. The size and shape of the inclusions are chosen based on the X-ray scans. Inclusions are approximated by piecewise polygons in 2D space and piecewise polyhedra in 3D space. A methodology to minimize the errors inherently introduced due to approximation of the geometry is built into the algorithm.

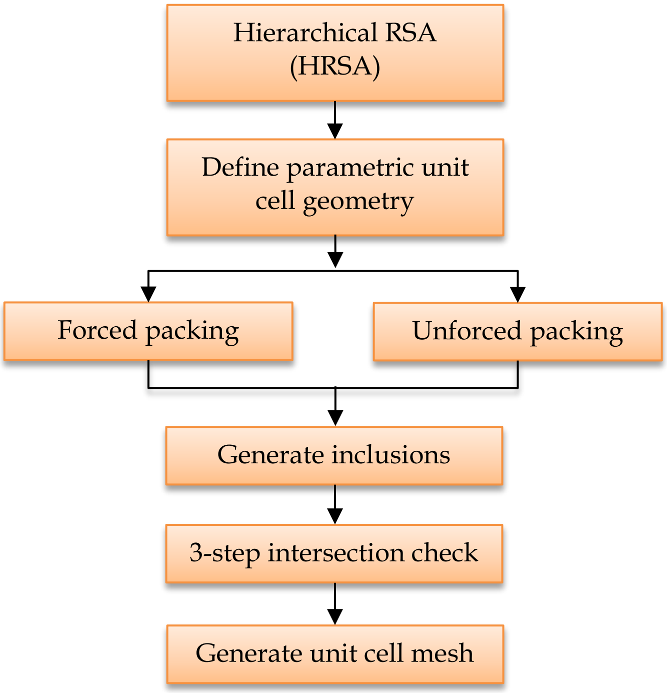
Hierarchical RSA
(HRSA)
Define parametric unit
cell geometry
Forced packing
Unforced packing
Generate inclusions
3-step intersection check
Generate unit cell mesh

Figure 5: Hierarchal levels in the HRSA algorithm

3.2.2 Forced Packing

Having described the unit cell geometry, the next step in the HRSA algorithm is to develop strategies for attaining higher inclusion packing fractions. Forced packing is imperative in generating unit cells with higher packing fractions by either varying the size or shape of the inclusions. For instance, microstructures of materials such as polyurea comprise of soft and hard domains. The hard domain comprises of inclusions of varying sizes in the form of ellipsoids. In generating such microstructures, first inclusions with highest AR are added. Once the jamming point is attained inclusions with decreasing aspect ratios (AR<10) are gradually added.

In addition to changing the size of the inclusions, forced packing is also accomplished by *changing the shape* of the inclusions for inclusions with AR>10. The inclusion geometry in general is described by the coordinates of the center, the in-plane angle range $\phi \in [0, 2\pi]$ and the out-of-plane angle range $\theta \in (0, 2\pi)$. The first inclusion is generated without enforcing any change in shape or size. From the second inclusion onwards, the inclusion being added is checked for intersection with all the previously generated inclusions. The intersection points on the inclusion being added are identified by projecting that inclusion along with all the previously generated fibers on a 2D space and obtaining a closed form solution using the closest point of approach (CPA) method [74]. After the intersection points on the new inclusion being added are identified, additional points are added on the inclusion spine to enforce a change in shape. In the case of random chopped fiber composites, two pairs of additional points are added on either side of the intersecting point for bending the fiber in- and out-of- plane as shown in Figure 6 and Figure 7. Given the set of independent and dependent parameters the inclusion geometry is constructed in 3D.

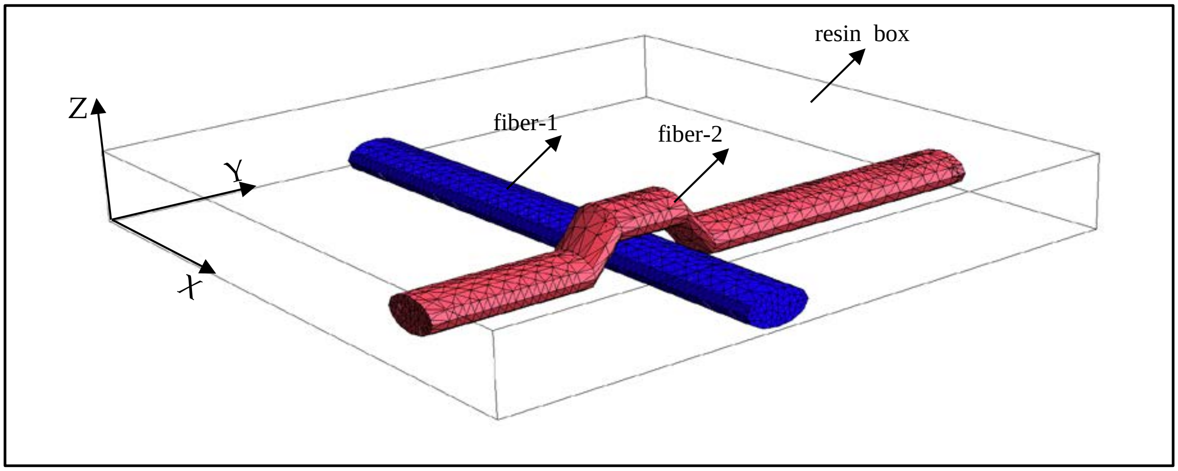

Figure 6: Fiber-2 forced to bend over fiber-1 at the intersecting point

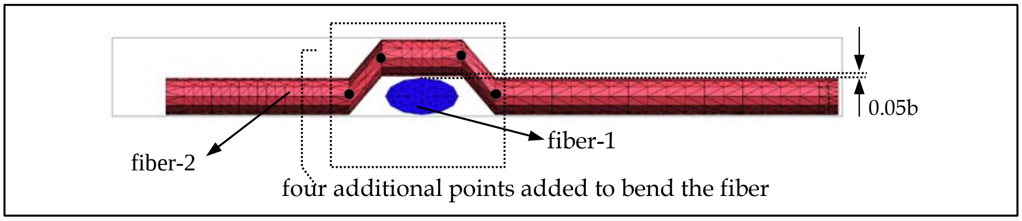

Figure 7: Four additional vertices added on fiber-2 to enforce shape change

The intersection check using the CPA method is given below.

Consider two infinite lines

$$L_1 = P(s) = P_1 + s \bullet (P_2 - P_1) = P_1 + s \bullet \vec{u}$$
$$L_2 = P(t) = P_3 + t \bullet (P_4 - P_3) = P_3 + t \bullet \vec{v} \tag{3.1}$$

Let $\vec{w}(s,t) = P(s) - P(t)$ be a vector between two points on the two lines as shown in Figure 8. We want to find $\vec{w}(s,t)$ that has a minimum length for all *s* and *t*. Eberly [75] used algebraic approach to determine the shortest length between the two infinite lines. Sunday [74] used the geometric approach, the CPA and so did Teller [76] . However, Teller's method uses cross product of the line segments that restricts it to 3D space. The closed form solutions given by Eberly and Sunday are faster than Teller's approach, which computes intermediate planes and gets their intersections with the two lines. In the present work we employ the geometric approach proposed by Sunday [74].

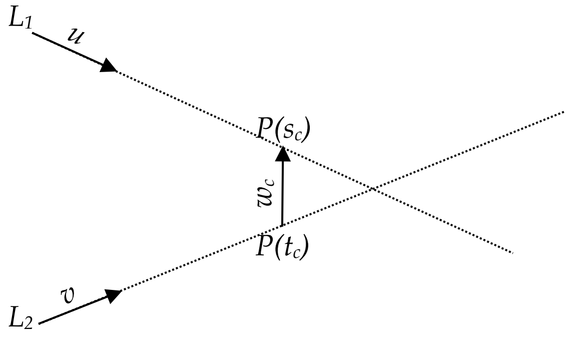

Figure 8: Intersection of two line segments

In Figure 8, two lines L_1 and L_2 are closest at unique points $P(s_c)$ and $P(t_c)$ for which $\vec{w}(s,t)$ attains its minimum length. If L_1 and L_2 are not parallel, then the line segment $\vec{w}(s_c,t_c)$ joining the closest points $P(s_c)$ and $P(t_c)$ is uniquely perpendicular to both lines at the same time. No other line segment between L_1 and L_2 has this property. Vector $\vec{w}_c = \vec{w}(s_c,t_c)$ is uniquely perpendicular to the vectors $\vec{u}$ and $\vec{v}$, and this is equivalent to it satisfying the two equations:

$$\vec{u} \bullet w_c = 0 \text{ and } \vec{v} \bullet \vec{w}_c = 0 \tag{3.2}$$

By substituting $\vec{w}_c = P(s_c) - P(t_c) = \vec{w}_0 + s_c \bullet \vec{u} - t_c \bullet \vec{v}$ where $\vec{w}_0 = P_1 - P_3$ into equation (3.2) gives two simultaneous linear equations:

$$\begin{aligned} (\vec{u}\bullet\vec{u})s_c - (\vec{u}\bullet\vec{v})t_c &= -\vec{u}\bullet\vec{w}_0) \\ (\vec{v}\bullet\vec{u})s_c - (\vec{v}\bullet\vec{v})t_c &= -\vec{v}\bullet\vec{w}_0) \end{aligned} \tag{3.3}$$

Then, letting $a = \vec{u}\bullet\vec{u},\ b = \vec{u}\bullet\vec{v},\ c = \vec{v}\bullet\vec{v},\ d = \vec{u}\bullet\vec{w},\ e = \vec{v}\bullet\vec{w}$ we can solve for s_c and t_c :

$$s_c = \frac{be - cd}{ac - b^2} \text{ and } t_c = \frac{ae - bd}{ac - b^2} \tag{3.4}$$

where the denominator $ac - b^2$ is nonzero. When $ac - b^2 = 0$, the two lines are parallel and the distance between the lines is constant. We can solve for the distance of separation by fixing the value of one parameter and using either equation to solve for the other. Selecting $s_c = 0$, we get $t_c = d / b = e / c$.

Having solved for the closest point s_c and t_c, the distance between them is given by:

$$d(L_1, L_2) = \vec{w}_0 + s_c \vec{u} - t_c \vec{v} \tag{3.5}$$

In the approach used by Pan *et. al*. [64], the distance between two points on two different generic line segments is given by:

$$d(\xi_1, \xi_2) = \left\| \vec{P}_1(\xi_1) - \vec{P}_2(\xi_2) \right\| \tag{3.6}$$

The minimum distance between two lines is determined by minimizing the constrained nonlinear two-variable function $d(\xi_1, \xi_2)$ described in equation(3.6),

$$d_{\min 2D} = \min(d(\xi_1, \xi_2)) \tag{3.7}$$

subjected to the constraints $0 < \xi_1 < 1$ and $0 < \xi_2 < 1$ where ξ is the normalized distance along the line segment. The closed form solution in equation (3.5) is computationally more efficient than the minimization problem in equation(3.7).

3.3 Unforced Packing

Microstructures with either a low inclusion aspect ratio or a low volume fraction obviate the necessity to force packing. In generating such unit cells the inclusions are not enforced to change their shape or size. Therefore the intersection check using CPA method can be bypassed, thereby reducing the computational cost. The inclusion geometry as in the case of forced packing is described by the coordinates of the center $C(x, y, z)$, the in-plane angle range

$\phi \in [0,2\pi]$ and the out-of-plane angle range $\theta \in (0,2\pi)$. Given the set of independent and dependent parameters, inclusions are generated and sequentially added in the unit cell domain.

3.4 Hierarchical Inclusion Generation Strategy

Optimization tools have been previously used [64] to check for inclusion intersections in 3D space. In the HRSA algorithm, closed form solutions are incorporated to check for inclusion intersections in 3D space rather than optimization tools to provide increased efficiency. This step is executed after the inclusions are generated in 3D and preceded by either the forced or the unforced packing phase.

The method of separating axis serves as the main engine for checking whether or not the inclusions intersect in 3D space. However, the computational cost of this method is enormous. To reduce the computational cost, the method of separating axis is preceded by a hierarchy of less costly methods, such as the method of radial distances and the method of separating planes. With this hierarchy in place, a somewhat large set is checked for intersections using the significantly less costly methods of intersecting ellipsoids and separating planes. Consequently, a small subset needs to be checked for intersections using the method of separating axis. This results in a significant increase in the computational efficiency of the RSA algorithm. The three methods are explained in the following sections in the order of their implementation in the algorithm.

3.4.1 Method of Radial Distances

This is the first method in the three-step hierarchical approach. The method involves estimation of the radial distance between the inclusion being currently added and all the previously generated inclusions. The larger set is reduced to a small subset by considering the inclusions in the near field of the inclusion being added and excluding all other inclusions in the far field. It is trivial exercise to show that inclusion of any shape can be contained in a convex ellipsoid with three semi principal axes a, b, and c with $R = \max\{a,b,c\}$. Thus, for two ellipsoids with centers A and B, if the distance between A and B is larger than 2R, then these two ellipsoids do not intersect. Thus all the inclusions that are at a radial distance greater than 2R from the center of the inclusion being added can be excluded from the next intersection check in the three-step hierarchy.

3.4.2 Method of Separating Planes

Two stationary convex objects do not intersect if and only if there exists a plane that separates them - a *separating plane*. The method is based on determining whether a node on one object lies on or inside the other object given the relative position of the node with respect to all the planes on the other object. Consider a plane in the infinite space that has two sides: the inner side and the outer side. By using the right-handed rule, it is possible to distinguish between the two sides. Let ΔABC be the triangle lying on this plane with nodal coordinates denoted by $A(x_a, y_a, z_a)$, $B(x_b, y_b, z_b)$ and $C(x_c, y_c, z_c)$. The nodes are numbered counterclockwise. Consider an arbitrary node $P(x,y,z)$. We determine its location relatively to the triangle ΔABC by calculating

$$\Delta = \begin{vmatrix} 1 & x_A & y_A & z_A \\ 1 & x_B & y_B & z_B \\ 1 & x_C & y_C & z_C \\ 1 & x & y & z \end{vmatrix} = \begin{vmatrix} x_B - x_A & y_B - y_A & z_B - z_A \\ x_C - x_A & y_C - y_A & z_C - z_A \\ x - x_A & y - y_A & z - z_A \end{vmatrix} \tag{3.8}$$

If $\Delta > 0$, then node P is at the outer side of the plane and vice versa; if $\Delta \leq 0$, then P is on the plane or at the inner side of the plane. If a node on a convex object lies inside all the surfaces of the other object, then the two convex objects are intersecting.

3.4.3 Method of Separating Axes

This section discusses the method of separating axis - the method employed to determine whether two stationary convex objects are intersecting or not. It can be proved that, two convex stationary objects will not intersect if; there exists a line for which the intervals of projection of the two objects onto that line do not intersect. This line is termed as a *separating line* or, more commonly, as a *separating axis* [77].

Consider two compact, convex sets C_1 and C_2 and a line D passing through the origin. The projection intervals of these compact, convex sets on to the line D are given by

$$\begin{aligned} I_1 &= \left[\xi_{\min}^{(1)}(D), \xi_{\max}^{(1)}(D)\right] = \left[\min\{D \bullet X \ : \ X \in C_1\}, \max\{D \bullet X : X \in C_1\}\right] \\ I_2 &= \left[\xi_{\min}^{(2)}(D), \xi_{\max}^{(2)}(D)\right] = \left[\min\{D \bullet X \ : \ X \in C_2\}, \max\{D \bullet X : X \in C_2\}\right] \end{aligned} \tag{3.9}$$

where ξ is the projection vector on D and the superscripts corresponds to the index of the convex set. The two convex sets do not intersect, if $\xi_{\min}^{(1)}(D) > \xi_{\max}^{(2)}(D)$ or $\xi_{\max}^{(1)}(D) < \xi_{\min}^{(2)}(D)$. A 2D example is shown in Figure 9 to illustrate the idea of this method.

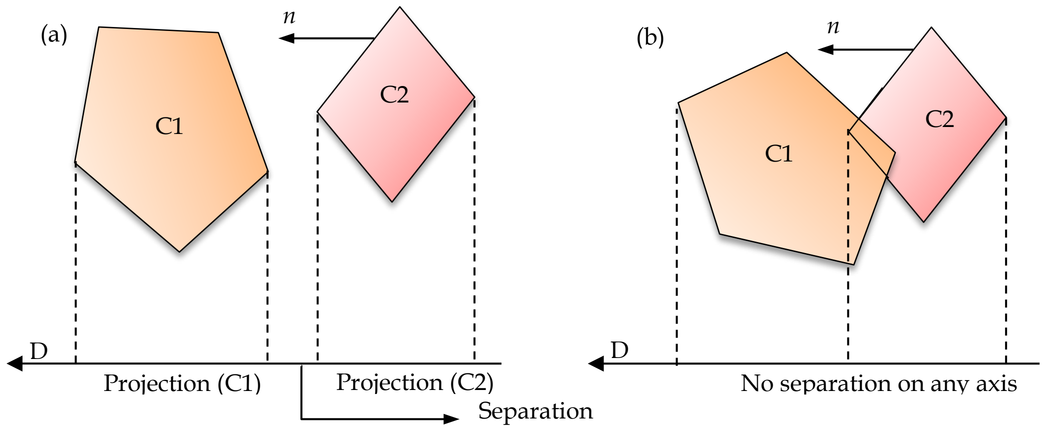

Figure 9: Intersection check in 2D using method of separating axes

To check for the intersection of convex polyhedra in 3D space the set of direction vectors includes the normal vectors to the faces of the convex polyhedra and vectors generated by the cross product of two edges, one from each polyhedron. The curved fibers are considered to be comprising of s piecewise compact, convex sets. Let C_j with $j = 1,2$ be the convex polyhedra with vertices $\left\{V_i^{(j)}\right\}_{i=1}^{L}$ edges $\left\{E_i^{(j)}\right\}_{i=1}^{M}$ and faces $\left\{F_i^{(j)}\right\}_{i=1}^{N}$ with outward pointing normal to each face being computed and stored.

Alternatively, a separation check for convex polyhedra in 3D space can be performed by solving an optimization problem. Two convex polyhedra containing "s" faces can be algebraically defined by a set of solutions to a linear system of equations defined by

$$\begin{aligned} A_1\vec{x}_1 &\le b_1 \\ A_2\vec{x}_2 &\le b_2 \end{aligned} \tag{3.10}$$

where A_1 and A_2 are real $s \times 3$ matrices, b_1 and b_2 are real $s \times 1$ matrices and x_1 and x_2 are vectors of the coordinates of the convex polyhedra in 3D space.

The minimum distance between two inclusions in 3D space can then be determined by solving the convex optimization problem

$$d_{\min}^{3D} = \min[d(x_1, x_2)] \tag{3.11}$$

The minimization solution is computationally less efficient compared to method of separating axis.

3.5 Chopped Fibers Randomly Oriented in 2D Plane

In this section the implementation of the HRSA algorithm to generate unit cell geometry with fibers that are randomly dispersed in the resin medium as seen in the microstructures of short fiber thermoplastics. We consider a chopped fiber tow (or fiber bundle) that has a large number of individual fibers. In the present manuscript the term *"fiber"* will be loosely referred to the fiber bundle or fiber tow. The chopped fiber composites are manufactured by blowing these chopped fiber tows on to a mandrel to create a perform which is then injected by a resin in a rapid injection process [78].

Planar scans of the chopped fiber composite material suggest that the chopped fiber bundles are randomly oriented in the XY plane. The through-the-thickness scans suggest that the fiber bundle cross section has been deformed into an elliptical cross-section during the compression molding process with the minor semi-axis of the elliptical cross-section along the out-of-plane direction (Z-axis). The fibers are either straight or curved as seen in the scans. The fiber bundles do not intersect each other and can be curved at the fiber bundle contact points.

The unit cell geometry generation algorithm for carbon chopped fiber composites builds on the work of Pan et al. [64]. The algorithm [64] has been modified to obtain higher fiber packing fractions and to improve the computational efficiency. Fibers are modeled as straight cylinders whereas the curved fibers are approximated by piecewise straight cylinders. A curved fiber profile is approximated by a piecewise convex polyhedra. The fiber elliptical cross-section is approximated by a dodecagon. The fiber geometry is described by the coordinates of the center $C(x,y,z)$, the elliptical cross-section major axis a, the minor axis b, the fiber length l, and the in plane angle range $\phi \in [0,2\pi]$ with predefined out-of-plane angle $\theta = \pi / 2$. The fiber volume fraction V_f, the cross-section major axis and minor axes and the fiber length are all user defined parameters. The gap between adjacent fibers can be user-defined, but in the present study is set to be 5% of the fiber cross-section semi-minor axis b. The in-plane unit cell size is assumed to be a function of the fiber length.

The unit cell geometry comprises of two fiber rich layers of thickness $2b$ separated by three resin rich layers of thickness $b / 20$. The unit cell length and breadth are defined in the XY plane with the out of plane thickness determined by fiber cross-section and the resin layers, which is 4.15 times the semi-minor axis of the fiber cross-section (Refer to Figure 10(c)). Fibers are randomly generated in the X-Y plane bounded by the in-plane dimensions of the unit cell, with the elliptical cross-section major axis a lying in the X-Y plane and the minor axis b along the out-of-plane Z direction as shown in Figure 10(b). The center and the in-plane angle are generated randomly, with the provision to define bounds for the in-plane distribution to account for preferential orientation as found in some material microstructures. Fibers are not allowed to intersect in 2D or 3D space. In case of a new fiber intersecting with previously generated fibers, the new fiber is forced to bend at the intersection points as shown in Figure 6 and Figure 7. The bend is either in- or out-of- the X-Y plane so that the projection of the fibers on to the X-Y plane is a straight line. The lower fiber-rich layer accommodates only fibers with no bends whereas the upper fiber-rich layer can accommodates the bends on the curved fibers and straight only fibers as well.

To generate unit cells with fiber volume fractions of up to 45% in the shortest possible time it is imperative that the fibers be tightly packed as they are sequentially added to the resin box. To this effect, the unit cell volume is divided into five zones as follows. The planar areas of these zones are parameterized in terms of the unit cell planar dimensions. Thus the planar areas of these zones will change with a change in the fiber aspect ratio. Fibers are initially generated in zone 1 which is the area surrounding the center of the planar dimensions as shown in Figure 11. The available area is then gradually increased to involve zone-2 and zone-3. The zone-4 area comprises of the areas at the four corners of the plane. Fibers are restricted to be generated in this zone by restricting the area for generating the fiber center and the spatial orientation. The zone-5 comprises of the second fiber rich layer.

A statistical study is conducted to determine the maximum volume fraction that can be achieved in every zone and the optimum number of realizations required to achieve that volume fraction. This study is conducted for unit cells with fiber aspect ratios of 5.0, 10.0, 15.0, 20.0 and 25.0. The maximum achievable volume fraction and the optimum number of realizations for each of the five zones is studied for the five fiber aspect ratios. The fiber generation process moves from one zone to the next when either the bound on achievable volume fraction or the number of realizations is reached for that zone. The unit cell geometry is meshed with tetrahedral elements based on predefined mesh density. A pseudo resin layer with a thickness of *b/20* is introduced around the unit cell to ensure that unit cell has perfect periodic boundaries.

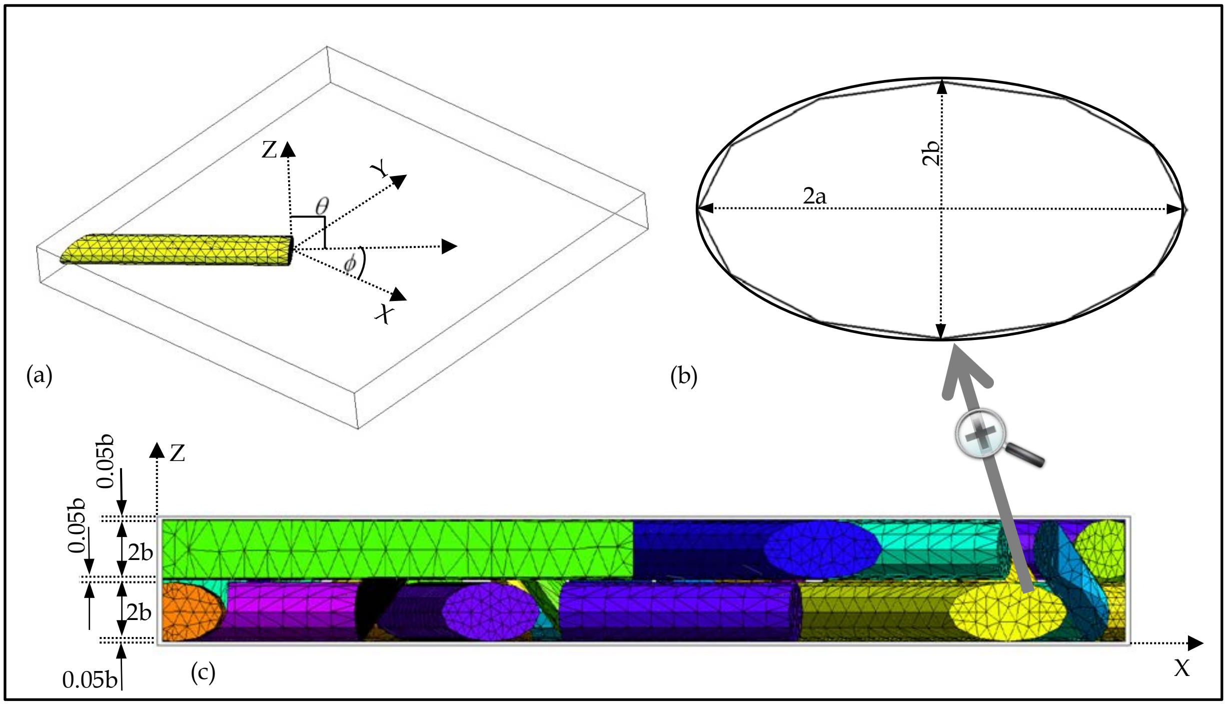
Z
Y
θ
ϕ
X
(a)
2b
2a
(b)
0.05b
0.05b
Z
2b
2b
0.05b
(c)
X

Figure 10: Random chopped fiber unit cell geometry

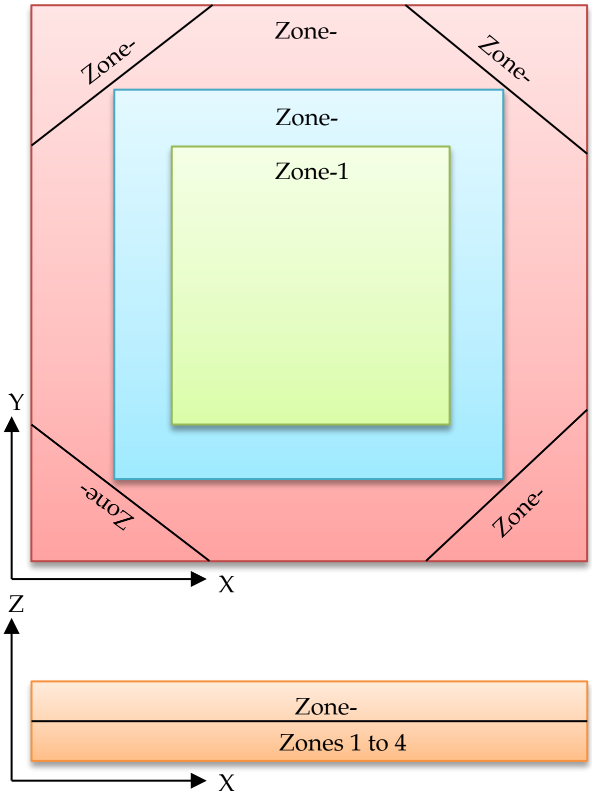
Zone-
Zone-
Zone-
Zone-
Zone-1
Y
Zone-
Zone-
X
Z
Zone-
Zones 1 to 4
X

Figure 11: Division of the unit cell volume into five zones

The HRSA algorithm flowchart is depicted in Figure 12. The unit cell generation algorithm is described below

(i) For a randomly generated center in 3D space C(x, y, z) and in-plane angle range $\phi(0,2\pi)$ the fiber spine is generated in the lower fiber rich layer. Based on the zones discussed above, the z coordinate of the fiber spine center is either defined to lie in the bottom fiber-rich layer or the top fiber-rich layer.

(ii) From the generation of the second fiber onwards, a newly generated fiber spine along with all the previously generated fiber spines are projected onto the XY planes to check whether or not the new fiber intersects with any of the previously generated fibers. The Closest Point of Approach [74] method is incorporated into the algorithm to check for fiber intersections in 2D space.

(iii) If the newly generated fiber does not intersect with any previously generated fibers, then the fiber is generated in 3D space by sweeping the fiber cross-section profile along the fiber spine. Subsequently, the fiber is added to the unit cell, the fiber volume fraction is updated and the algorithm moves on to generate the next fiber spine.

(iv) If the newly generated fiber spine intersects with any of the previously generated fiber spines, then the intersection points are identified on the new fiber spine.

(v) Next, the z coordinate of the intersection point on the new fiber spine is moved to the next fiber rich layer. In addition two pairs of additional points are added on either side of the intersecting point on the top and bottom fiber rich layers for bending the fiber in and out of the X-Y plane as shown in Figure 6 and Figure 7.

(vi) The fiber is generated in 3D by sweeping the cross-section profile along the fiber spine.

(vii) If any of the fiber lies outside the unit cell, they are clipped by the planes of the resin bounding box. Since the clipped fiber lengths only need to be taken into account to update the fiber volume fraction, the fibers need to be checked and clipped on the fly.

(viii) The fiber is checked for intersection with the other fibers in 3D space through the method of separating axis [77].

(ix) If the new fiber passes the 3D intersection check, then it is added to the unit cell and the fiber volume fraction is updated.

(x) Steps (i) to (ix) are repeated till the required fiber volume fraction is achieved.

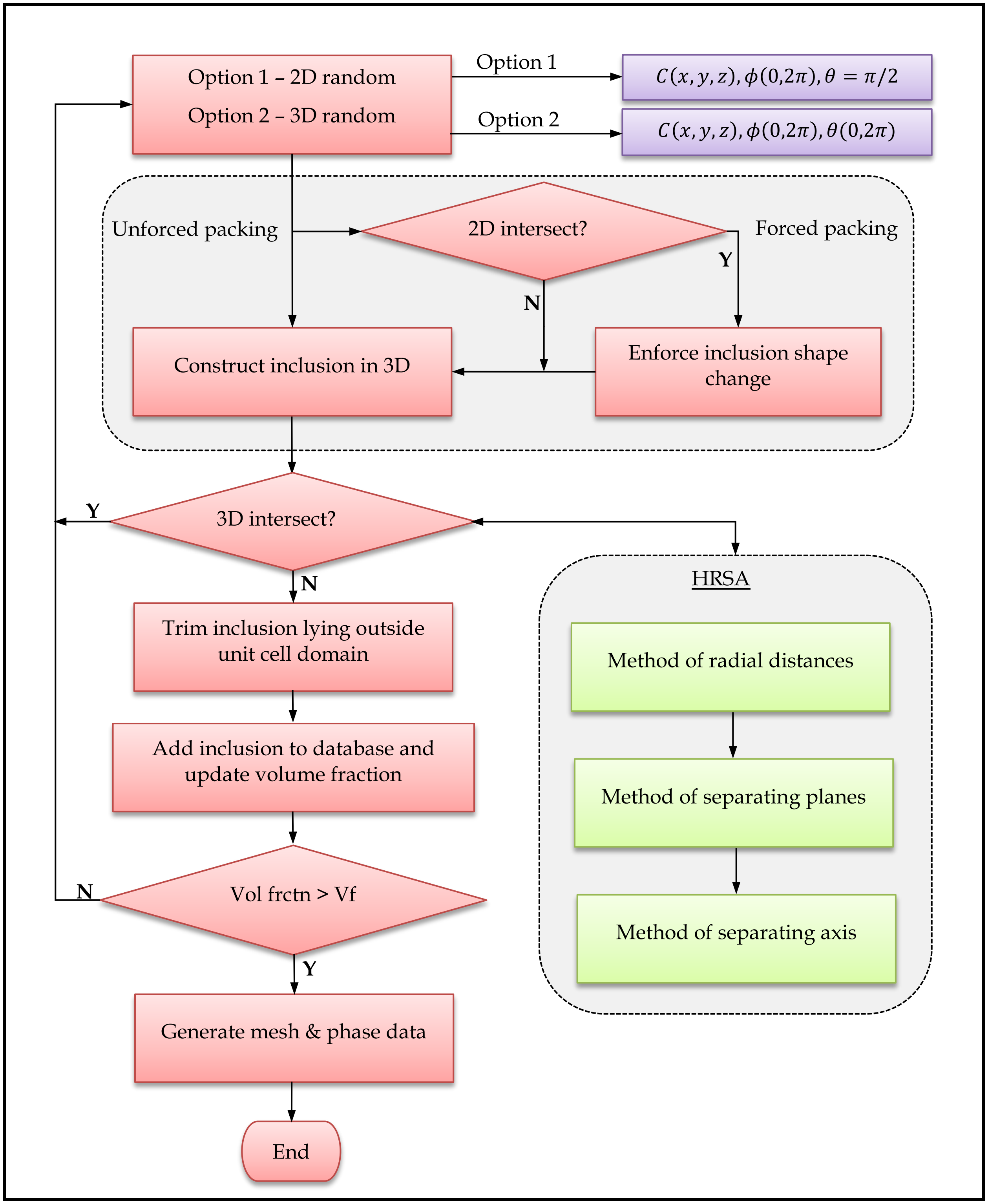
Option 1 – 2D random
Option 2 – 3D random
Option 1
Option 2
$C(x,y,z), \phi(0,2\pi), \theta = \pi/2$
$C(x,y,z), \phi(0,2\pi), \theta(0,2\pi)$
Unforced packing
2D intersect?
Forced packing
Y
N
Construct inclusion in 3D
Enforce inclusion shape change
Y
3D intersect?
N
HRSA
Method of radial distances
Method of separating planes
Method of separating axis
Trim inclusion lying outside unit cell domain
Add inclusion to database and update volume fraction
N
Vol frctn > Vf
Y
Generate mesh & phase data
End

Figure 12: Hierarchical RSA algorithm

3.6 Inclusions Randomly Oriented in 3D Space

The process of generating a random inclusion composite unit cell in 3D consists of placing inclusions of a given shape and size (or size range) and rotation angle (or rotation angle range) one by one in randomly selected positions in the unit cell domain. Each time a new inclusion is attempted to be placed in the unit cell domain, the overlaps with existing inclusions are checked for. If a newly introduced inclusion does not overlap with previously generated inclusion, it is accepted; otherwise, another position is attempted. If, after a predefined number of trials, the inclusion has not found its place so that it does not overlap with existing inclusions, it is discarded and another inclusion is selected and tried in the same manner. This process is repeated until a predefined inclusion volume fraction is reached. The algorithm can be easily implemented for complex inclusion geometries. However, the method is very time consuming and, for non-spherical inclusions, rearrangement by way of rotation is often not possible. Moreover, since some inclusions may have to be discarded, the size distribution of packed inclusions may be different from the intended. The packing density depends on the sequence of inclusion addition. For example, if larger inclusions are added first, the final packing density tends to be higher than if smaller inclusions are placed first. In the following paragraphs we describe the algorithm for unit cells with inclusions in the form of straight chopped fibers randomly oriented in 3D space and unit cells with ellipsoidal inclusions.

3.6.1 Randomly Oriented Chopped Fibers Embedded in Matrix

The microstructure of materials such as phenolic impregnated carbon ablators (PICA) consists of chopped fibers randomly dispersed in resin. The volume fraction of fibers is typically very small. The algorithm developed to generate the randomly oriented chopped fibers in 2D space can be tailored to generate the unit cell for carbon phenolic impregnated carbon ablators

(PICA). The inclusions are idealized by straight cylinders, with user-defined cross-section and length. Since the inclusions are randomly oriented in 3D space, the center $C(x,y,z)$ and the in-plane $\phi(0,2\pi)$ and the out-of-plane $\theta(0,2\pi)$ angles are randomly generated. The random orientation in 3D space obviates the intersection check in 2D space. The aforementioned three-step intersection check process is used to check for fiber intersections in 3D space. A newly generated fiber is rejected if it fails the intersection check in 3D space. The unit cell with straight chopped fibers randomly oriented in 3D space is shown in Figure 13.

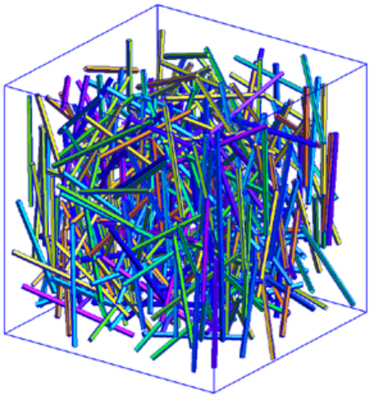

Figure 13: Straight chopped fibers randomly distributed in 3D

3.6.2 Randomly Oriented Bonded Fibers Free of Matrix (FiberForm)

FiberForm is a low density very porous carbon fiber insulation material designed for high temperatures applications. It consists of a group of carbon fibers bonded to each other by means of an organic binder that is carbonized at very high temperature as shown in Figure 14. The FiberForm unit cell is defined parametrically as a function of handful parameters, such as fiber characteristics (volume fraction, dimensions, orientations) and the dimensional characteristics of binders. The FiberForm unit cell generation process consists of two steps. In Step 1, a unit cell with randomly oriented disconnected fibers embedded in matrix material as described in the previous section is generated. In Step 2, the binders connecting the fibers are generated as follows. The nearest distance between a fiber and its neighboring fiber is computed by looping over all the fibers. If the distance between a fiber and its neighboring fiber is less than the user-prescribed binder length, then all the matrix elements between the nearest points on each fiber are enclosed in a cylinder to create a bond between the fibers. Once all the bonds in the unit cell are identified, the elements in the enclosed cylinders are reassigned with binder material properties. The resulting FiberForm unit cell consists of three phases: fibers, binders and fictitious matrix phase, which excludes the binders. There are two possibilities to proceed. Matrix elements lying outside the fiber and binder phases can be removed resulting in a two-phase material consisting of fibers and binders. Alternatively, one can assign negligible elastic material properties to the fictitious matrix phase resulting in a three phase material. The former is obviously computationally advantageous, while the latter provides additional robustness in case some fibers are “not sufficiently connected”, i.e. connected at a fewer than two nodes resulting in a mechanism and ultimately singularity of the resulting stiffness matrix. In the latter case the fictitious matrix serves as a stabilizer. The FiberForm unit cell is depicted in Figure 14.

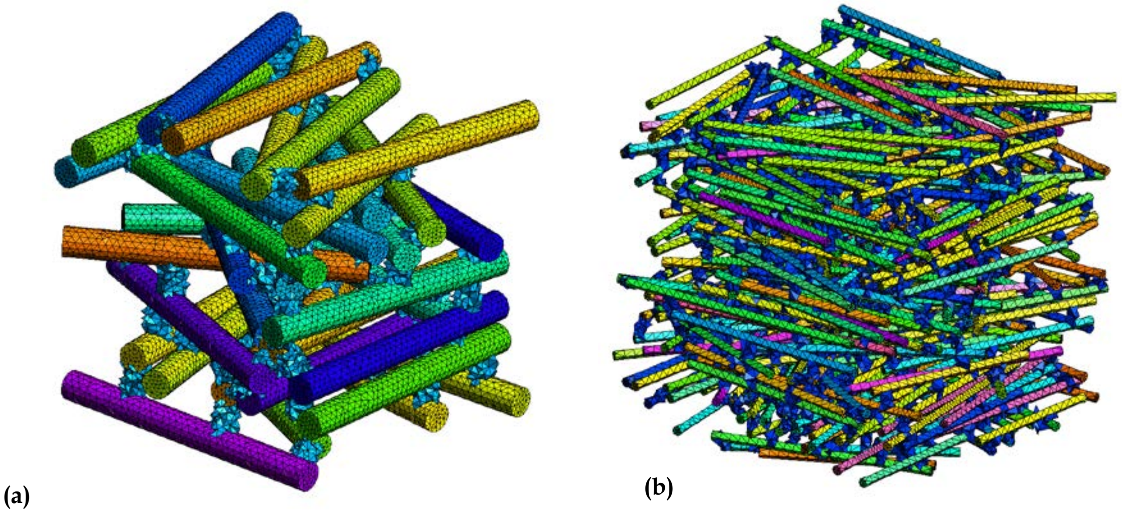

Figure 14 (a) FiberForm unit cell with fiber volume fraction 5% and cross section radius equal to 2.4; (b) FiberForm unit cell with fiber volume fraction 10% and cross section radius equal to 0.6

3.6.3 Ellipsoidal Inclusions Randomly Oriented in 3D Space

The geometry of an ellipsoid is defined by the coordinates of the center $C(x, y, z)$, the semi-principal axes *a, b* and *c*, the in-plane angle $\phi(0, 2\pi)$ and the out-of-plane angle $\theta(0, 2\pi)$. The center is generated randomly whereas the major axis *a*, minor axes *b* and *c*, and the in-plane angle ϕ and out-of-plane angle θ are user defined parameters. One can generate these parameters randomly or specify exact values in order to generate unit cells with preferential size and packing angles of the ellipsoids. The ellipsoids are randomly oriented in 3D space. The geometry of an ellipsoidal inclusion is shown in Figure 15 (a). As in the case of chopped fibers the ellipsoids are checked for intersection in 3D space using the three-step hierarchical approach discussed above. To this effect, an ellipsoid is discretized into a convex polyhedron with 48 sub-surfaces, as shown in Figure 16. The three-step hierarchical intersection check in 3D is outlined in Figure 17. A unit cell with randomly sized and oriented ellipsoids is depicted in Figure 15 (b).

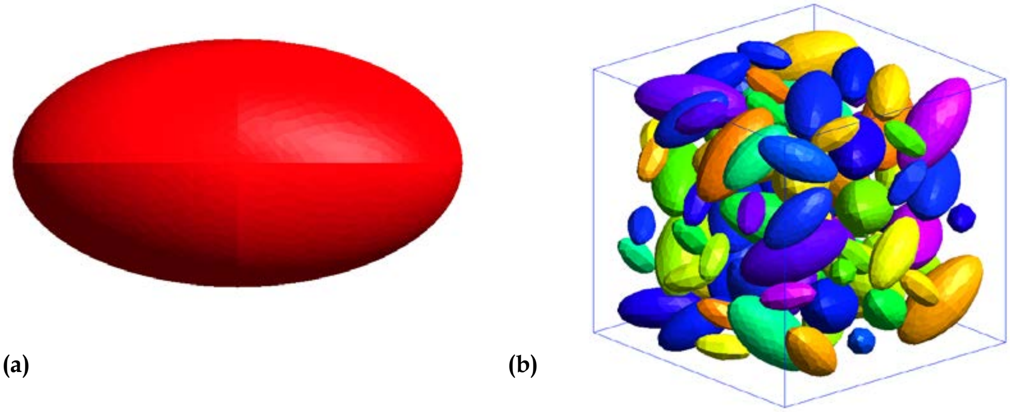

(a) (b)

Figure 15: (a) Geometry of an ellipsoidal inclusion (b) an ellipsoidal inclusion unit cell

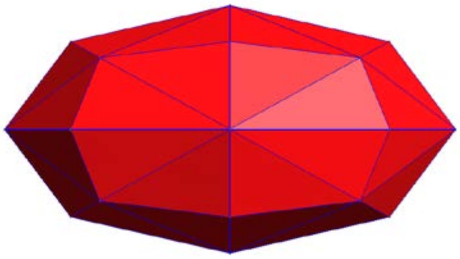

Figure 16: Discretization of an ellipsoidal inclusion into 48 faces

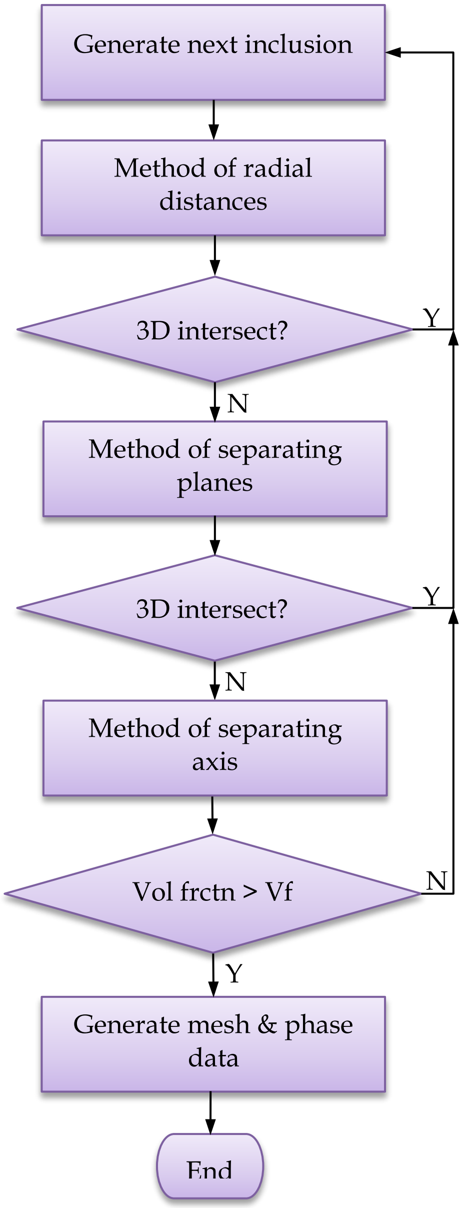
Generate next inclusion
Method of radial distances
3D intersect?
Y
N
Method of separating planes
3D intersect?
Y
N
Method of separating axis
Vol frctn > Vf
N
Y
Generate mesh & phase data
End

Figure 17: A three-step hierarchical intersection check algorithm

The computational times involved in generating a unit cell with ellipsoidal inclusions by employing the method of separating axes alone and the three step hierarchical approach for is shown in **Figure 18**. It is evident that the three-step intersection checking approach significantly reduces computational cost when compared with the method of separating axes alone.

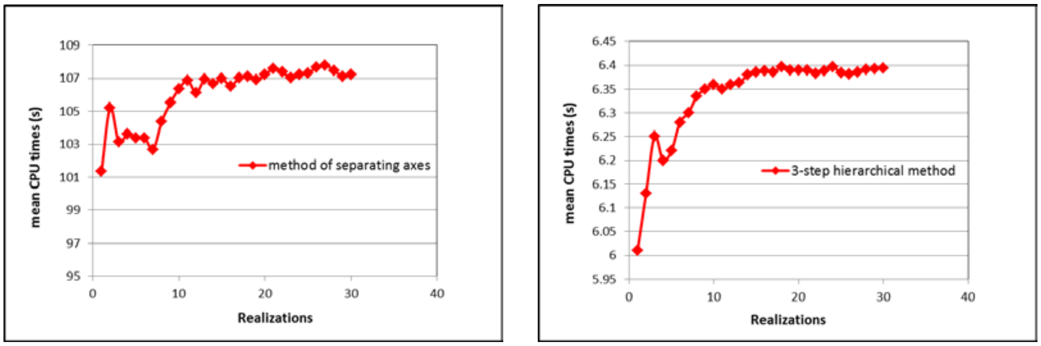

Figure 18: Comparison of cpu times between method of separating axes and the 3-step hierarchical method

3.7 Statistical Study to Determine the Size of Unit Cell

For random microstructure composites there are several definitions of the unit cell or representative volume element (RVE). The first definition suggests that the unit cell is a statistical representation of the microstructure of the composite material. This implies that the unit cell size should be sufficiently large to include an effective sampling of all the heterogeneities including grains, cracks, voids and inclusions. The average of the estimates of material properties should be accurate and the scatter should be small. The second definition by Drugan and Willis [79] suggests that the unit cell is the smallest volume element of the material for which the spatially constant “overall modulus” macroscopic constitutive representation is a sufficiently accurate to represent mean constitutive response. This definition does not insist that the scatter be small but only the average of the estimates be accurate, which is a superimposition of all the possible fluctuations associated with local microstructure. Kanit et al. [80] suggests that smaller unit cells with morphological or physical properties averaged over several number of realizations of the unit call may be used to get the same accuracy as given by a large unit cell which is a statistical representation of the microstructure. The variance for each unit cell size is used to define the precision of the property estimates. The notion of integral range is used to relate the precision to the minimum unit cell size. Thus for a given precision and number of realizations the minimum required unit cell volume can be determined to give accurate effective properties.

In this section we present a study to determine the size of the unit cell with randomly distributed chopped fibers. The scope of the research involves computation of the effective properties, in this case the homogenized modulus averaged over several realizations for five different unit cell sizes and study the distribution of the variance and mean of the homogenized properties in comparison to the experimentally observed mean properties, based on which the effective size of the unit cell is decided. The study also investigates whether or not, the optimal size of the unit cell depends on the relative physical and mechanical properties of the phases comprising the microstructure. In our study we consider carbon fiber, which is approximately two orders magnitude stiffer than the resin phase, and the glass fiber, which is approximately one order of magnitude stiffer than the resin phase.

The unit cell in-plane dimensions are considered to be equal and parameterized in terms of the random chopped fiber length. The unit cell thickness is determined by the fiber cross-section area and is set to $4.15 * b$ for all the five cases, where b is the semi-minor axis of the elliptical cross-section of the fiber. Various number of realizations are carried out for size ratios of 1.0, 1.5, 2.0, 2.5 and 3.0, where the size ratio (SR) is defined as

$$\mathrm{SR}=\frac{\text{Unit Cell planar dimenison}}{\text{fiber length}} \tag{3.12}$$

The statistical study has been implemented in a stochastic multiscale framework. At the coarse-scale coupons of the glass and carbon fiber reinforced composites are subjected to uniaxial tension test. The fine scale microstructure geometry is constructed by utilizing the HRSA algorithm presented in Section 2.2. The unit cell problem is then subjected to six modes of deformation and the stress influence functions are computed by solving the unit cell problem [31-33]. The homogenized elastic stiffness tensor is computed by integrating the stress influence function over the unit cell domain. The flowchart illustrating the statistical study framework is shown in Figure 19. The following guidelines are adhered to in determining the optimal unit cell size.

(i) The in-plane Young's moduli in tension (E_{11}^{c}, E_{22}^{c}) averaged over the realizations should converge and they should converge to the spatially constant mean response E_{eff}^{c} observed in the experiments.

(ii) The variance or the relative error of the averaged properties should be within a specified tolerance.

(iii) There exists a unit cell in the realization history that has the in-plane moduli equal to the mean moduli that is $E_{11}^{c} = E_{22}^{c} = E_{eff}^{c}$. This is required in order to conduct model reduction on a macroscopically homogeneous unit cell.

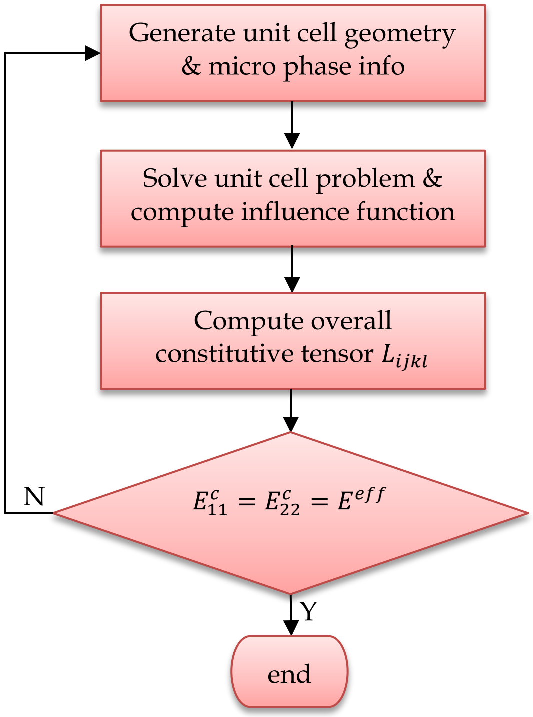
Generate unit cell geometry & micro phase info
Solve unit cell problem & compute influence function
Compute overall constitutive tensor L_{ijkl}
$E_{11}^c = E_{22}^c = E^{eff}$
N
Y
end

Figure 19: Statistical study framework

3.7.1 Carbon Fiber Microstructure

The results of the statistical study involving the randomly distributed carbon fiber composite unit cell are presented in this section. Figure 20 to Figure 24 depict the average in-plane elastic moduli as obtained over the increasing number of realizations for each of the five cases for carbon fiber composite.

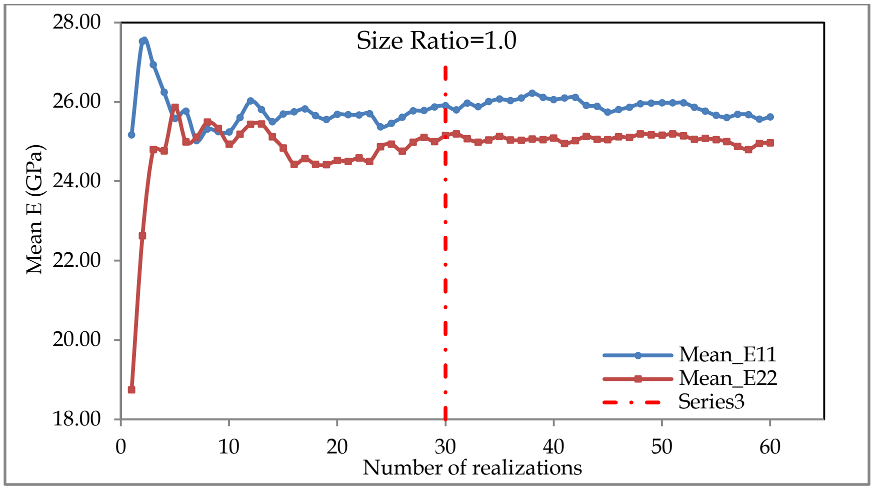

Figure 20: Carbon fiber microstructure: Averaged in-plane moduli for SR=1.0

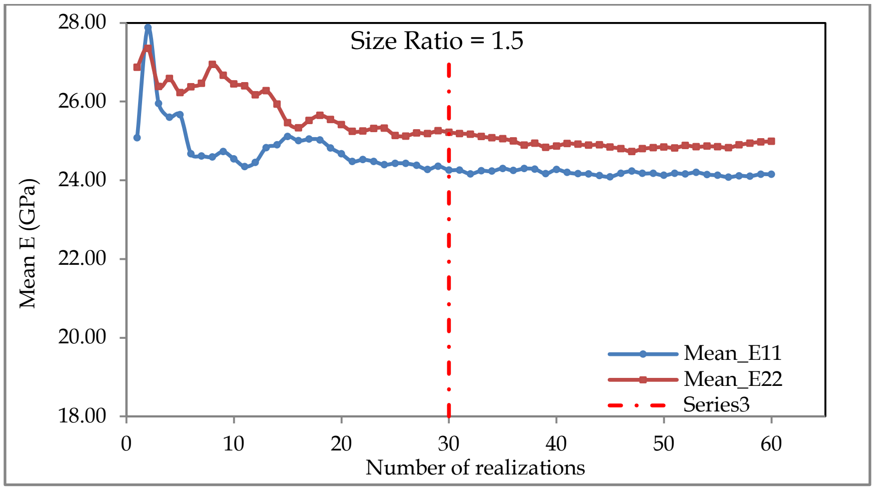

Figure 21: Carbon fiber microstructure: Averaged in-plane moduli for SR=1.5

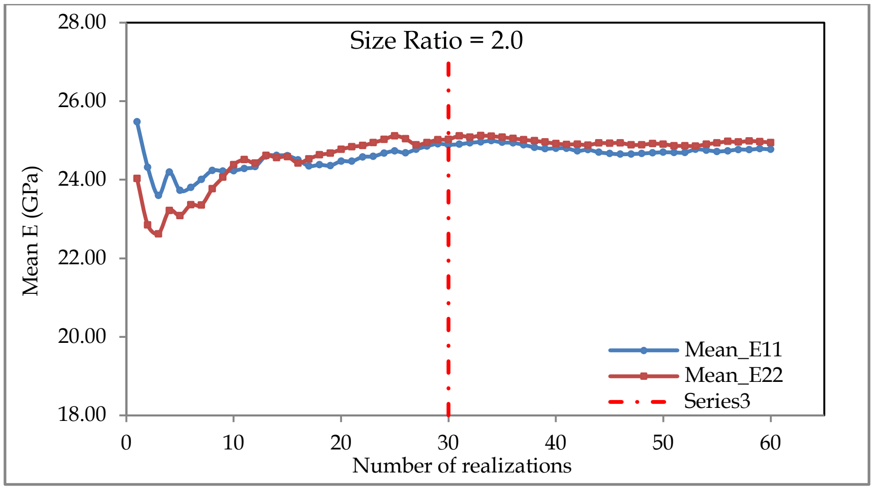

Figure 22: Carbon fiber microstructure: Averaged in-plane moduli for SR=2.0

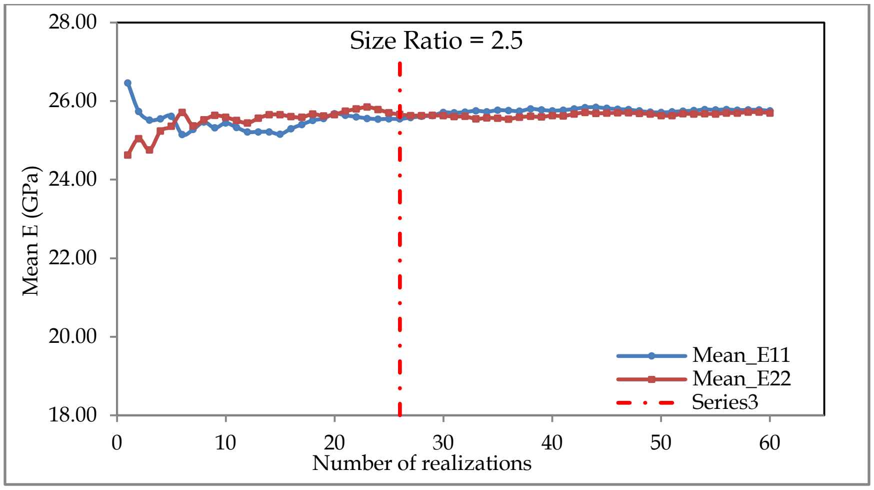

Figure 23: Averaged in-plane moduli for SR=2.0 and SR=2.5

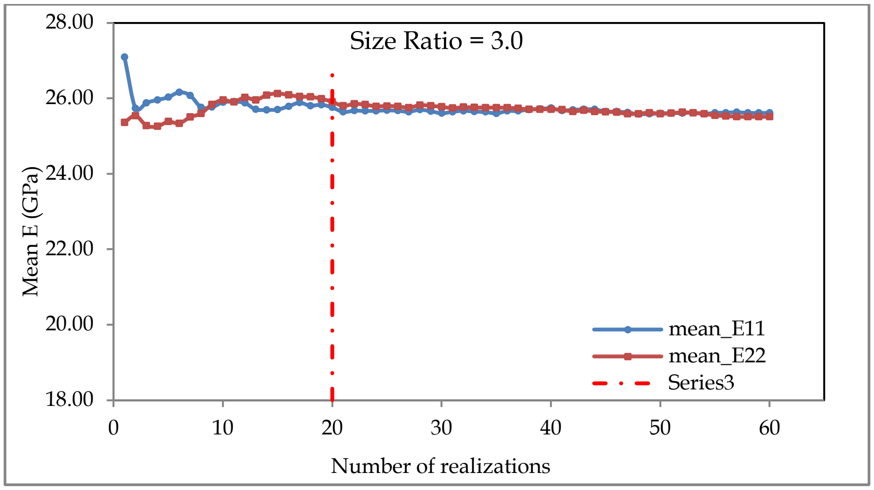

Figure 24: Carbon fiber microstructure: Averaged in-plane moduli for SR=3.0

For cases with SR=1.0 and SR=1.5, the in plane moduli converge but do not converge to the mean. This is attributed to the bias observed in small unit cells. Similar bias has been reported by Huet [81], Sab [82] and Ostoja-Starzewski [83]. Kanit et al. [80] reported that very small unit cells subjected to kinematic uniform boundary conditions (KUBC) yielded an average modulus close to the upper Voigt bound, whereas those subjected to static uniform boundary conditions (SUBC) yielded an average modulus close to the lower Reuss bound. The modulus of unit cells subjected to periodic boundary conditions varied the least as a function of the size of the unit cell. The averaged in-plane moduli, the variance and the relative error are presented in Figure 25, Figure 26 and Figure 27 respectively.

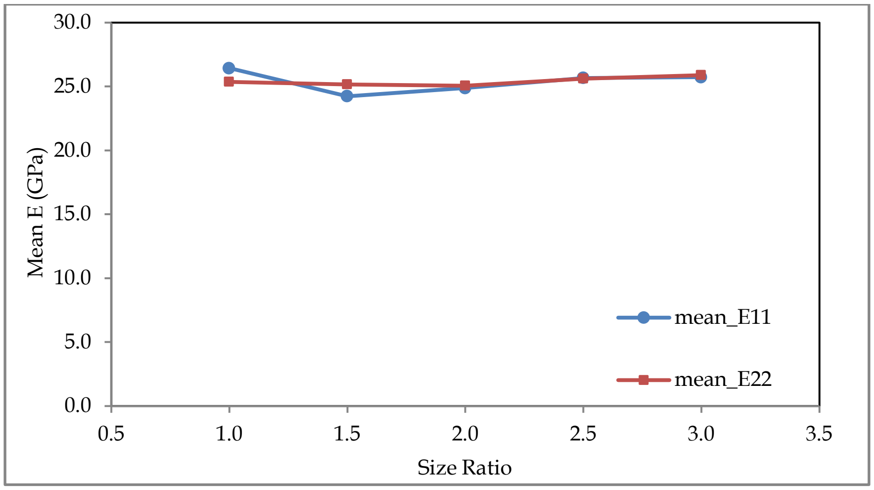

Figure 25: Mean of homogenized modulus for carbon fiber microstructure for SR=1.0 to SR=3.0

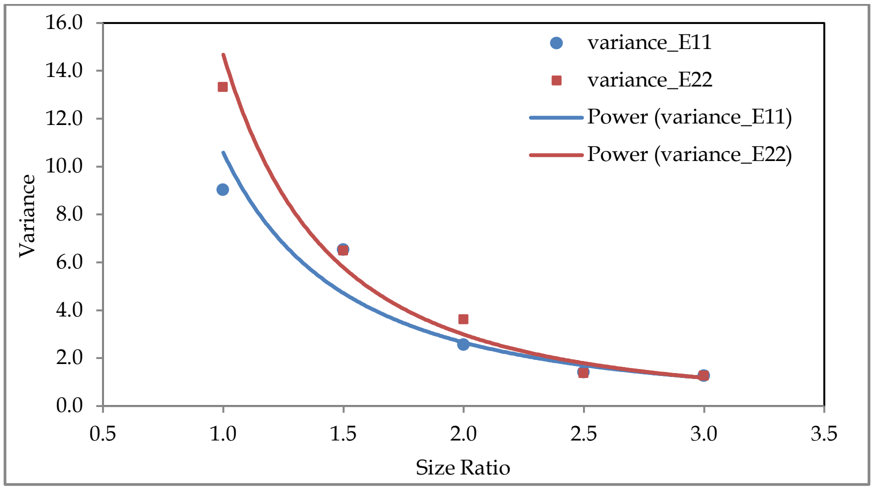

Figure 26: Variance of homogenized modulus for carbon fiber microstructure for SR=1.0 to SR=3.0

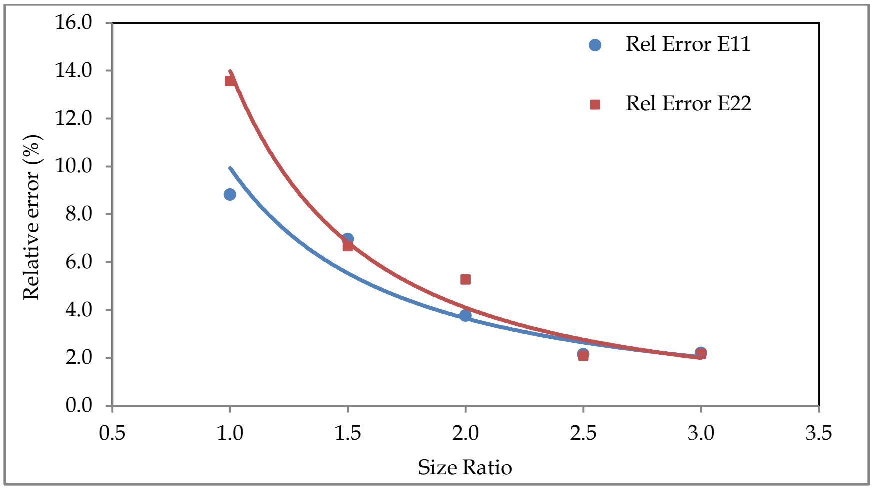

Figure 27: Carbon fiber microstructure: Relative error for SR=1.0 to SR=3.0

It is evident from Figure 25 that for the size ratio greater than 2.0 the mean in-plane moduli averaged over realizations is nearly constant. The relative error in Figure 27 decreases according to power law with the relative error being less than 5% for size ratio (SR) greater than two. The mean computational time for generating the unit cell and computing the homogenized modulus tensor for all five cases is presented in Figure 28. It can be seen that the mean computational time increases exponentially with the increase in the size of the unit cell.

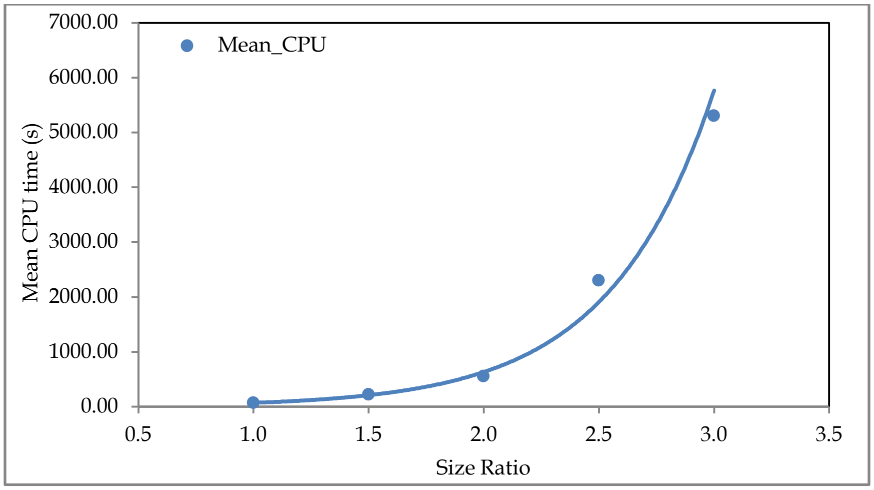

Figure 28: CPU time for SR=1.0 to SR=3.0

For the case with SR = 2.0 it takes a fairly reasonable number of realizations (around 30) to converge and a mean computational time per realization is roughly 550 s. Thus the total CPU time is approximately 16500 s and the relative error is around 4%. For the case with size ratio of 2.5 and 3.0 the relative error is around 2% and convergence to the mean in 20-25 realizations is around 55000 s for SR=2.5 and 106000 s for SR=3.0. Thus SR = 2.0 seems to be optimal and is chosen to statistically represent the microstructure of the random chopped fiber composite material.

3.7.2 Glass Fiber Microstructure

In this section we conduct statistical study for the chopped glass fiber unit cell. As in the previous section the averaged in-plane elastic modulus is obtained over the increasing number of realizations for each of the five cases as shown in Figure 29 - Figure 33. Unlike for the carbon-fiber unit cell, the averaged in-plane elastic modulus for the glass-fiber unit cell converges for all the five cases. The number of realizations required for convergence decreases with increasing SR. Since the geometry of the unit cell remains the same, the mean computational time for generating the unit cell and computing the homogenized modulus tensor for all five cases is the same as in Figure 28. The in-plane elastic modulus variance as a function of the size ratio for both the carbon and glass fiber unit cell microstructures is shown in Figure 35.

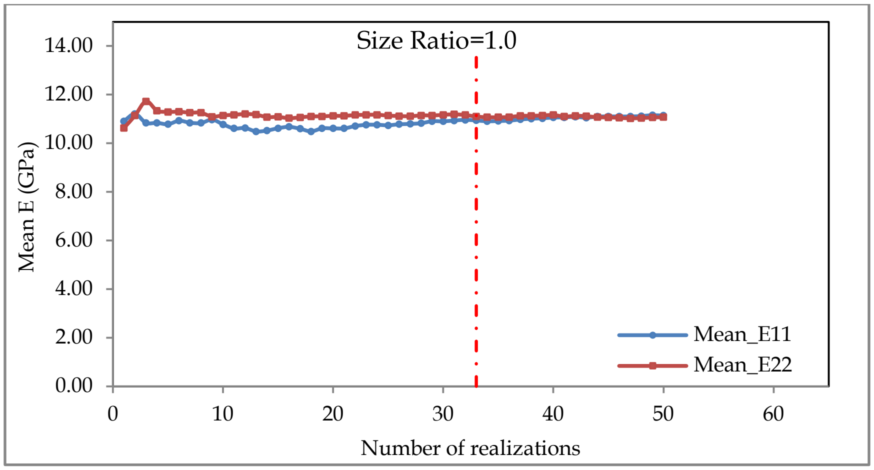

Figure 29: Glass fiber microstructure: Averaged in-plane moduli for SR=1.0

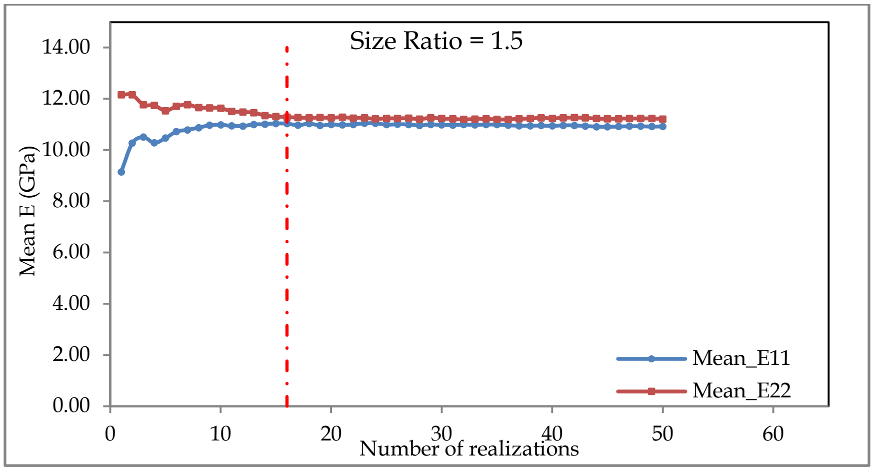

Figure 30: Glass fiber microstructure: Averaged in-plane moduli for SR=1.5

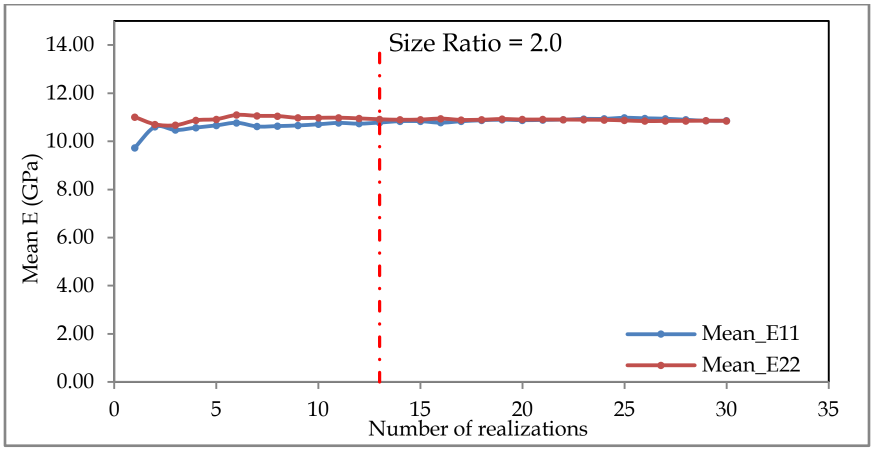

Figure 31: Glass fiber microstructure: Averaged in-plane moduli for SR=2.0

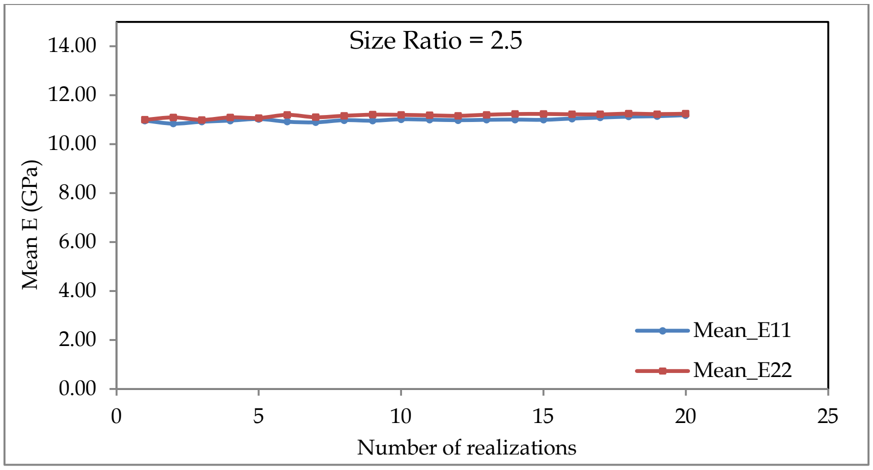

Figure 32: Glass fiber microstructure: Averaged in-plane moduli for SR=2.5

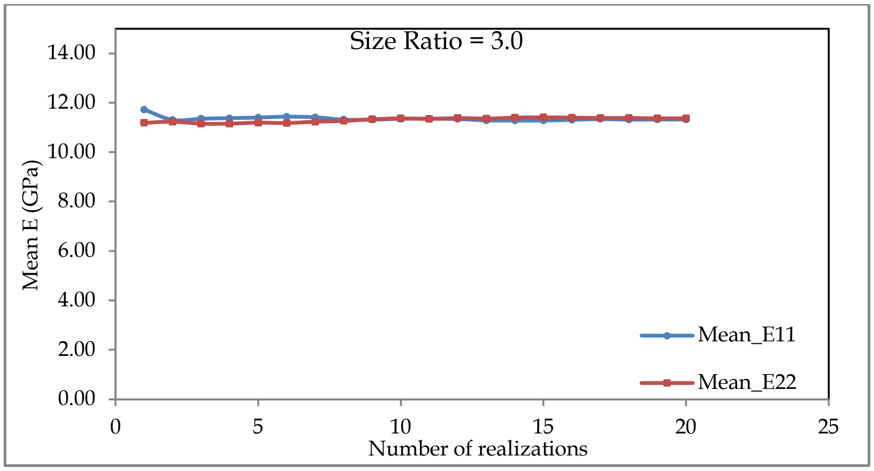

Figure 33: Glass fiber microstructure: Averaged in-plane moduli for SR=3.0

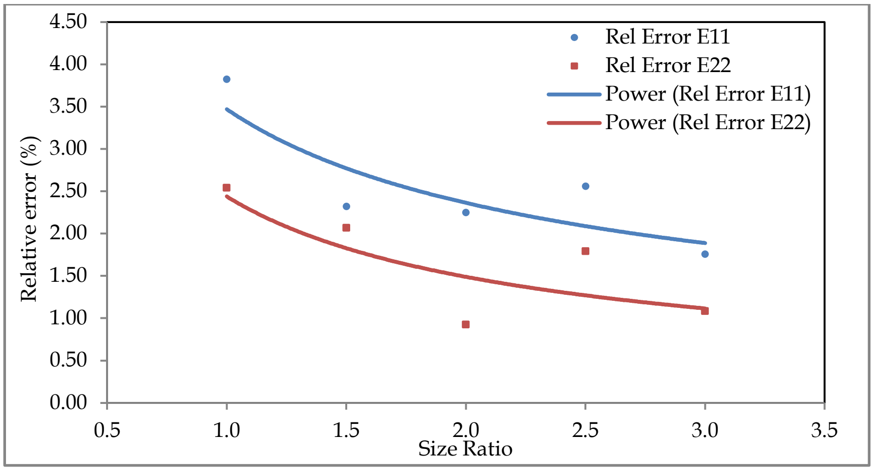

Figure 34: Glass fiber microstructure: Averaged in-plane moduli for SR=3.0 and relative errors

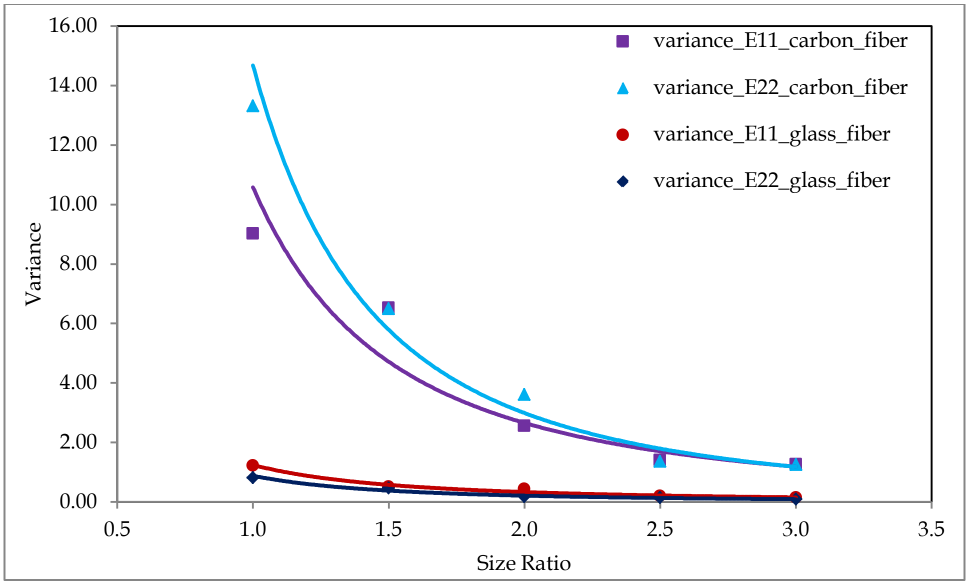

Figure 35: The in-plane elastic modulus variance as a function of the size ratio for both the carbon and glass fiber unit cell microstructures

For the case with SR = 1.0 it takes around 33 realizations to converge and the mean computational time per realization is roughly 68s. Thus the total CPU time is approximately 2244 s and the maximum relative error is around 3.8%. For the case with size ratio of 1.5 it takes around 16 realizations to convergence and the mean computational time per realization is around 220s thus amounting to a total CPU time of 3520s and the maximum relative error is around 2.3 %. For the case with SR=3.0 the number of realizations to convergence is 13 with an average computational time of 550s thus amounting to a total of 7150s and a maximum relative error of 2.25%. Taking into account the optimal values for the CPU time and the relative errors, we conclude that the case with SR = 1.5 is nearly optimal for the e-glass fibers. This leads to a conclusion that for a given material system with randomly distributed inclusions the optimal size of the unit cell depends on the relative stiffness of the phases comprising the microstructure.

3.8 Methodology to Control the Volume Fractions of Constituent Phases

The volume fractions of the constituent phases in the unit cell are affected by the geometry idealization and mesh size. Geometric approximation errors are introduced when curved features in the geometry are approximated by planar surfaces. Consequently, the resulting volume fractions of the constituent phases may vary from the actual volume fractions of phases. The errors introduced by mesh discretization can be reduced by refining the mesh, but this will significantly increase the computational cost involved in solving the unit cell problem. Alternatively, one can generate a higher volume fraction of the constituent phases than required, so that the resultant volume fraction attained is equal to the actual volume fraction of the constituent phase [54]. In the present study, the mesh density parameter is specified as a multiple of the fiber cross-section semi-minor axis *b*. For a mesh seeding size equal to *b*, the error introduced by mesh discretization has been found to be approximately 7%. The volume fraction errors introduced by finer mesh densities have been pre-computed by numerical experiments. The following empirical equation was employed to obtain a desired volume fraction

$$V_f^{gen} = V_f^{act}(1 + V_f^{error}) \tag{3.13}$$

where V_f^{gen} is the volume fraction generated, V_f^{des} is the desired volume fraction of the inclusion in the random chopped fiber composite and V_f^{error} is the error in the volume fraction introduced by mesh discretization.

3.9 Conclusion

In this chapter a parametric model for generating unit cells with randomly distributed inclusions is developed. The proposed algorithm is robust, yields unit cells with fiber volume fraction of up to 45% for aspect ratios as high as 20 and possesses versatility by being able to generate unit cells with inclusions of varying shapes and sizes. Computational efficiency is incorporated into the algorithm through a hierarchy of algorithms with increasing computational complexity. The method has been implemented to generate to microstructure geometries of various random inclusion composites, namely two-dimensional chopped tow composites; polyurea or polyethene coating consisting of hard and soft domains (segments) and carbon *fiberform* embedded in, or free from an amorphous matrix. A statistical study aimed at determining the effective size of the unit cell is conducted. The study considered two material systems, namely 35% by volume randomly distributed glass fiber microstructure geometry and a 35% by volume randomly distributed carbon fiber microstructure geometry. For the carbon fiber microstructure, the averaged in-plane elastic moduli converged to the effective properties for cases with SR>2.0 only and the suggested optimum SR is 2.0. For the glass fiber microstructure the in-plane averaged elastic moduli converged for all the five cases and the optimum SR is 1.5. This leads to a conclusion that for a given material system with randomly distributed inclusions the optimal size of the unit cell depends on the relative stiffness of the phases comprising the microstructure.

PART IV

SPACE-TIME MULTISCALE HOMOGENIZATION

Chapter 4

Space-Time Multiscale Homogenization for Heterogeneous Materials

In this chapter the temporal homogenization theory is formulated. The theory is integrated with spatial homogenization theory presented in Chapter 2 to develop a unified space-time homogenization theory to analyze problems consisting of multiple length scales and multiple domains. The model is validated for fatigue life analysis of high temperature CMC's with turbo-machinery applications. The inputs from co-authors of the paper (Bailakanavar et.al. [84]) from which the main sections in this chapter are reproduced are gratefully acknowledged.

4.1 Introduction

Fatigue of heterogeneous material systems is a multiscale phenomenon in space and time. It is multiscale in space due to the fact that the size of a material heterogeneity, defects and cracks could be of several orders of magnitude smaller than of a structural component. It is multiscale in time because the cyclic load period could be of the order of seconds while component life may span years. Owing to this tremendous disparity between spatial and temporal scales, component fatigue life prediction poses tremendous challenge to engineers.

The study of fatigue life prediction dates back to the 19th century [85]. The first paper describing failure due to cyclic loading was published in 1829 [86]. Fatigue life prediction methods range from sole experimentation, to modeling and computational resolution of spatial scales. Today, experiments are the essential design tools for fatigue life estimations. S-N curves [87], which provide component life versus cyclic stress/strain level information, are the most commonly used tools in practice. Due to considerable scatter in fatigue life data, a family of S-N curves with probability of failure known as S-N-P plots is often used. On the other hand, numerical studies of fatigue life prediction often employ the Paris law [88] for predicting high cycle (~ above 1000 cycles) fatigue life and the ε-N curves [89, 90] for low cycle fatigue life (~

below 1000 cycles). More recently, fatigue life predictions based on continuum damage mechanics (CDM) have been advocated for homogeneous [91-96] and heterogeneous [97-99] materials.

Paris law [88] can be viewed as an empirical temporal multiscale approach, which states that under ideal conditions of high cycle fatigue (or small scale yielding) and constant amplitude loading, growth rate of long cracks depends on the amplitude of the stress intensity factors. Models departing from these ideal conditions have also been developed and implemented [100-103]. Various crack growth "laws" have been used in conjunction with multiple spatial scales methods to propagate arbitrary discontinuities.

An alternative to Paris-like fatigue models is to carry out a direct cycle-by-cycle simulation. These simulations often employ a cohesive law to model fatigue crack growth based on unloading-reloading hysteresis [104]. However, the cycle-by-cycle approach is not feasible for high cycle fatigue life prediction of large scale heterogeneous systems. Nevertheless, an attractive feature of this approach is that it provides a unified treatment of long and short cracks and the ability to account for overloads.

To circumvent the computational challenges posed by the cycle-by-cycle simulation, several temporal multiscale approaches have been proposed. The first is often coined as a "block cycle jump" technique [99, 105, 106] wherein the rate of damage growth due to fatigue during a single load cycle is computed at each spatial integration point by constructing an ordinary differential equation

$$\frac{dw(x_I)}{dt} = w(x_I)\Big|_{K} - w(x_I)\Big|_{K-1} \tag{4.1}$$

where $\omega(x_I)$ is the damage variable at an integration point x_I, *t* is the cyclic load period; and K is a cycle count. The block cycle jump is closely related to the unified brittle-fatigue damage model [107]. The second approach [50, 108-110] employs a multiple temporal scales asymptotic analysis. By this approach, loads and response fields are assumed to depend on slow time coordinate *t,* due to slow degradation of material properties during fatigue, as well as on fast time coordinate τ , due to locally periodic loading in time domain.

In the present chapter, a unified space-time multiscale homogenization framework is developed for modeling of fatigue induced damage and prediction of fatigue life. We show that essentially the above mentioned temporal multiscale approaches are closely related and that the unified framework can be effectively utilized in practice for arbitrary material architectures and constitutive equations of phases at the fine scale. We start by introducing multiple temporal scales in the context of a single spatial scale and discuss the application of the proposed framework to model the phenomenon of fatigue. Consideration of multiple spatial and temporal scales is subsequently discussed. The unified space-time multiscale homogenization model is validated for high temperature ceramic matrix composites (CMC). In the present study we consider a local damage model where the finite element mesh serves as a localization limiter. A more general formulation necessitates consideration of non-local and gradient models (see [111] for nonlocal fatigue model).

4.2 Temporal Homogenization

In this section a unified temporal homogenization model is developed for homogeneous materials. Generalization of this approach to heterogeneous materials involving multiple length scales and multiple domains is presented in Section 4.3. The premise of the temporal homogenization formulation lies in the assumption that the damage nucleation and subsequent degradation of material properties occurs in a slow time scale as compared to the fast time scale in which the cyclic loads are applied. This assumption allows us to implement a temporal scales separation. The slow timescale is denoted by t and $t \in [0, N]$ where N is a number of cycles until failure. The fast timescale is denoted by τ and $\tau \in [0, \tau_0]$. The fast time scale is chosen to satisfy the local periodicity (τ- periodicity) assumption, similar to the fine-scale periodicity assumption in the spatial homogenization theory. The fast timescale is related to the slow timescale by $\tau = t/\eta$ where $0 < \eta \ll 1$. The response fields ϕ are assumed to depend on the two temporal scales:

$$\phi^{\eta}(x,t) = \phi(x,t,\tau) \tag{4.2}$$

Time differentiation of response fields with respect to multiple temporal scales is given by the chain rule:

$$\frac{d\phi^{\eta}(x,t)}{dt} = \frac{\partial\phi(x,t,\tau)}{\partial t} + \frac{1}{\eta}\frac{\partial\phi(x,t,\tau)}{\partial\tau} = \dot{\phi}(x,t,\tau) + \frac{1}{\eta}\phi'(x,t,\tau) \tag{4.3}$$

where $\frac{d\phi^{\eta}}{dt}$, $\dot{\phi}$, ϕ' denote total time derivative, partial time derivative with respect to slow time variable t and partial time derivation with respect to fast time variable τ , respectively.

Consider a homogeneous inelastic solid subjected to periodic loads and/or boundary conditions in time domain. Assuming, for simplicity, small deformations the governing equations are

$$\begin{aligned}
&\sigma_{ij,j}(x,t,\tau)+b_i(x,t,\tau)=0 \quad \text{on} \quad \Omega\times[0,N]\times[0,\tau_0],\\
&\sigma_{ij}(x,t,\tau)=L_{ijkl}(x)\big(\varepsilon_{kl}(x,t,\tau)-\mu_{kl}(x,t,\tau)\big) \quad \text{on} \quad \Omega\times[0,N]\times[0,\tau_0],\\
&\varepsilon_{ij}(x,t,\tau)=u_{(i,j)}(x,t,\tau) \quad \text{on} \quad \Omega\times[0,N]\times[0,\tau_0],\\
&u_i(x,t,\tau)=\overline{u}_i(x,t,\tau) \quad \text{on} \quad \partial\Omega^u\times[0,N]\times[0,\tau_0],\\
&\sigma_{ij}(x,t,\tau)n_j=\overline{t}_i(x,t,\tau) \quad \text{on} \quad \partial\Omega^t\times[0,N]\times[0,\tau_0].
\end{aligned} \tag{4.4}$$

The eigenstrain evolution equation can be expressed as

$$\frac{d\mu_{kl}}{dt}=f_{ij}\left(\sigma,\varepsilon,s\right) \tag{4.5}$$

where s_i denotes state variables. Applying temporal differentiation rule in (4.3) to (4.5) yields

$$\frac{d\mu_{kl}^{\eta}}{dt}=\dot{\mu}_{kl}+\frac{1}{\eta}\mu_{kl}'=f_{ij}\left(\sigma,\varepsilon,s\right) \tag{4.6}$$

Consider the leading order term in asymptotic expansion of eigenstrains

$$\mu_{kl}^{\eta}\left(x,t\right)\equiv\mu_{kl}\left(x,t,\tau\right)=\hat{\mu}_{kl}\left(x,t,\tau\right)+O(\zeta) \tag{4.7}$$

Substituting (4.7) into (4.6) yields the leading order equation

$$\frac{\partial\hat{\mu}_{kl}\left(x,t,\tau\right)}{\partial\tau}=0\rightarrow\hat{\mu}_{kl}=\hat{\mu}_{kl}\left(x,t\right) \tag{4.8}$$

Thus the leading order eigenstrain is only a function of slow time coordinate t, i.e.

$$\mu_{kl}\left(x,t,\tau\right)=\hat{\mu}_{kl}\left(x,t\right)+O\left(\eta\right) \tag{4.9}$$

Equation (4.9) suggests that inelastic deformations evolve slowly in time, i.e., it is little affected by what happens in a single load cycle. Applying the time-averaging operator

$$\left\langle \phi\left(x,t,\tau\right)\right\rangle \equiv \frac{1}{\tau_0}\int_0^{\tau_0}\phi\left(x,t,\tau\right)d\tau \tag{4.10}$$

to (4.9) yields

$$\left\langle \mu_{kl}\left(x,t,\tau\right)\right\rangle = \hat{\mu}_{kl}\left(x,t\right)+O\left(\eta\right) \tag{4.11}$$

Given the above definition of the time-averaging operator we can state the leading order slow-evolving (time-homogenized) governing equations

$$\begin{aligned}
&\left\langle \sigma_{ij}\right\rangle_{,j}(x,t)+\left\langle b_i\right\rangle(x,t)=0 \quad \text{on} \quad \Omega\times\left[0,N\right],\\
&\left\langle \sigma_{ij}\right\rangle(x,t)=L_{ijkl}(x)\left(\left\langle \varepsilon_{kl}\right\rangle(x,t)-\hat{\mu}_{kl}(x,t)\right) \quad \text{on} \quad \Omega\times\left[0,N\right],\\
&\left\langle \varepsilon_{ij}\right\rangle(x,t)=\left\langle u_{(i,j)}\right\rangle(x,t) \quad \text{on} \quad \Omega\times\left[0,N\right],\\
&\left\langle u_i\right\rangle(x,t)=\left\langle \overline{u}_i\right\rangle(x,t) \quad \text{on} \quad \partial\Omega^u\times\left[0,N\right],\\
&\left\langle \sigma_{ij}\right\rangle(x,t)n_j=\left\langle \overline{t}_i\right\rangle(x,t) \quad \text{on} \quad \partial\Omega^t\times\left[0,N\right].
\end{aligned} \tag{4.12}$$

To complete the definition of the initial-boundary value problem for the time-averaged governing equations in (4.12), it remains to construct the evolution equation for the leading order eigenstrain $\hat{\mu}_{kl}(\boldsymbol{x},t)$ with respect to slow time scale. The time derivative $\dot{\hat{\mu}}_{kl}(\boldsymbol{x},t)$ after $t=K$ cycles can be evaluated using finite difference over two subsequent cycles

$$\left.\dot{\hat{\mu}}_{kl}(x,t)\right|_{t=K}=\left.\hat{\mu}_{kl}(x,t)\right|_{t=K}-\left.\hat{\mu}_{kl}(x,t)\right|_{t=K-1} \tag{4.13}$$

Substituting (4.9) into (4.13) and denoting $\left(t=K-1,\tau=\tau_0\right)\equiv\left(t=K,\tau=0\right)$ yields the evolution equation of the leading order eigenstrain with respect to the slow timescale

$$\left.\dot{\hat{\mu}}_{kl}(x,t)\right|_{t=K}\cong\mu_{kl}(x,t=K-1,\tau=\tau_0)-\mu_{kl}(x,t=K,\tau=0) \tag{4.14}$$

Equation (4.14) states that the eigenstrain growth rate with respect to slow timescale can be approximated by computing the difference between the values of eigenstrain in the beginning and the end of the previous load cycle.

Using forward Euler's integration the eigenstrain after Δt_K cycles from the current load cycle *K* can be approximated by

$$\hat{\mu}_{kl}(x,t)\Big|_{t=K+\Delta t} = \hat{\mu}_{kl}(x,t)\Big|_{t=K} + \dot{\hat{\mu}}_{kl}(x,t)\Big|_{t=K} \Delta t_K \tag{4.15}$$

The relation in (4.15) is termed as the *predicto*r. It is important to note that by evolving eigenstrains (4.15) while keeping the rest of the fields (stresses, strains, etc.) unchanged would violate the governing equations in (4.4) .This inconsistency can be alleviated by equilibrating discrete equilibrium equations. In the remainder of the chapter, this process will be referred as *consistency adjustment*.

The block size Δt_K is selected to ensure accuracy based on the following criteria:

Let $\Delta\hat{\mu}_a$ be user-defined allowable eigenstrain increment for Δt_K cycles and $\max\limits_I \|\Delta\hat{\boldsymbol{\mu}}\|$ be the norm of the largest eigenstrain increment obtained in a single cycle among all the quadrature points *I*. Then the initial value of Δt_K can be evaluated as $\Delta t_K = \operatorname{int}\left\{\Delta\hat{\mu}_a / \max\limits_I \|\Delta\hat{\mu}\|\right\}$ where $\operatorname{int}\{\cdot\}$ denotes truncation to the decimal part.

Given the above initial value of the block size Δt_K evaluate the eigenstrain based on the average of the growth rates at $\dot{\hat{\mu}}_{kl}(x,t)\Big|_{t=K}$ and $\dot{\hat{\mu}}_{kl}(x,t)\Big|_{t=K+\Delta t_K}$

$$\hat{\mu}_{kl}(x,t)\Big|_{t=K+\Delta t_K}^{cor} = \hat{\mu}_{kl}(x,t)\Big|_{t=K} + \frac{\Delta t_K}{2}\left(\dot{\hat{\mu}}_{kl}(x,t)\Big|_{t=K} + \dot{\hat{\mu}}_{kl}(x,t)\Big|_{t=K+\Delta t_K}\right) \tag{4.16}$$

The relation in the above equation (4.16) is termed as the *corrector*. If the difference in some norm between the predictor (4.15) and corrector (4.16) is sufficiently small then the step is accepted and the above mentioned consistency adjustment is performed. Otherwise the block size is halved and the predictor-corrector step is repeated.

We now focus on solution post processing, similarly to the post processing in the spatial homogenization. Let ϕ^* be the fast-time correction from the average defined by

$$\phi^* = \phi^\zeta - \langle \phi \rangle \tag{4.17}$$

Then the governing equations for the fast-scale correction u_i^* can be obtained by subtracting the governing equation for the temporal averages in (4.12) from (4.4), which yields

$$\begin{aligned}
&\sigma^*_{ij,j}(x,\tau) + b_i^*(x,\tau) = 0 \quad on \quad \Omega \times [0,\tau_0], \\
&\sigma^*_{ij}(x,\tau) = L_{ijkl}(x)\varepsilon^*_{kl}(x,\tau) \quad on \quad \Omega \times [0,\tau_0], \\
&\varepsilon^*_{ij}(x,\tau) = u^*_{(i,j)}(x,\tau) \quad on \quad \Omega \times [0,\tau_0], \\
&u_i^*(x,\tau) = \overline{u}_i^*(x,\tau) \quad on \quad \partial\Omega^u \times [0,\tau_0], \\
&\sigma^*_{ij}(x,\tau)n_j = \overline{t}_i^*(x,\tau) \quad on \quad \partial\Omega^t \times [0,\tau_0].
\end{aligned} \tag{4.18}$$

It is instructive to point out that the above equations are linear. Moreover, if the prescribed boundary conditions and body forces have the same τ_0 periodicity, then $b_i^*(x,\tau)$, $\overline{u}_i^*(x,\tau)$, $\overline{t}_i^*(x,\tau)$ and the resulting fast-scale correction $u_i^*(x,\tau)$ can be computed by analyzing a linear problem (4.18) over a single load cycle. Finally, if $b_i^*(x,0)$, $\overline{u}_i^*(x,0)$, $\overline{t}_i^*(x,0)$ vanish at $\tau = 0$ then in the case of quasi-static loading the fast-scale correction vanish at the start and at the end of the cycle.

4.3 Unified Space-Time Multiscale Homogenization

Having developed the temporal homogenization model in context of a single spatial scale (inelastic homogeneous solid), we proceed to develop the unified formulation. The phenomenon of fatigue involves multiple length scales in space and time domains and hence the formulation is termed as *unified space-time multiscale homogenization.*

For a heterogeneous inelastic solid subjected to cyclic loading the spatial and temporal homogenization procedures can be sequentially applied starting with spatial upscaling. Spatial upscaling based on the reduced order homogenization described in Chapter 2, gives rise to the following equations at the coarse scale [26-33]:

$$\begin{aligned}
&\sigma^c_{ij,x_j}(x,t,\tau)+b^c_i(x,t,\tau)=0 \quad \text{on} \quad \Omega\times[0,N]\times[0,\tau_0],\\
&\sigma^c_{ij}(x,t,\tau)=L^c_{ijkl}\left(\varepsilon^c_{kl}(x,t,\tau)-\mu^c_{kl}(x,t,\tau)\right) \quad \text{on} \quad \Omega\times[0,N]\times[0,\tau_0],\\
&\varepsilon^c_{ij}(x,t,\tau)=u^c_{(i,j)}(x,t,\tau) \quad \text{on} \quad \Omega\times[0,N]\times[0,\tau_0],\\
&u^c_i(x,t,\tau)=\overline{u}^c_i(x,t,\tau) \quad \text{on} \quad \partial\Omega^u\times[0,N]\times[0,\tau_0],\\
&\sigma^c_{ij}(x,t,\tau)n^c_j=\overline{t}^c_i(x,t,\tau) \quad \text{on} \quad \partial\Omega^t\times[0,N]\times[0,\tau_0].
\end{aligned} \tag{4.19}$$

The coarse-scale stress in the reduced order spatial homogenization theory is updated by the fine-scale partitioned eigenstrain and partitioned eigen-separation [31-33]. The coarse-scale eigenstrain evolution equation will be constructed from the reduced order constitutive equations of partitioned eigenstrain and partitioned eigen-separation

$$\frac{d\mu^{(\alpha)}_{mn}}{dt}=f^{(\alpha)}_{mn}\left(\varepsilon^{(\alpha)},\tilde{s}^{(\alpha)}\right); \quad \frac{d\delta^{(\xi)}_{\breve{n}}}{dt}=f^{(\xi)}_{\breve{n}}\left(t^{(\xi)}_{\breve{n}},\breve{s}^{(\xi)}\right) \tag{4.20}$$

We proceed by decomposing the coarse-scale governing equations (4.19) into a slow timescale and a fast timescale initial and boundary value problem (IBVP) using the temporal averaging operator (4.10) and the time differentiation rule (4.3) .

Applying the time differentiation rule in equation (4.3) to the partitioned eigenstrain and eigen-separation in equation (4.20) yields

$$\begin{aligned} \frac{d\mu_{kl}^{(\alpha)}}{dt} &= \dot{\mu}_{kl}^{(\alpha)} + \frac{1}{\eta}\mu_{kl}^{(\alpha)\prime} = f_{kl}^{(\alpha)}\left(\varepsilon^{(\alpha)},\tilde{s}^{(\alpha)}\right) \\ \frac{d\delta_{\breve{n}}^{(\xi)}}{dt} &= \dot{\delta}_{\breve{n}}^{(\xi)} + \frac{1}{\eta}\delta_{\breve{n}}^{(\xi)\prime} = f_{\breve{n}}^{(\xi)}\left(t_{\breve{n}}^{(\xi)},\breve{s}^{(\xi)}\right) \end{aligned} \tag{4.21}$$

From (4.21) it follows that the leading order partitioned eigenstrains and eigen-separations do not depend on fast-time coordinate, i.e.

$$\begin{aligned} \mu_{kl}^{(\alpha)}\left(x,t,\tau\right) &= \widehat{\mu}_{kl}^{(\alpha)}\left(x,t\right) + O\left(\eta\right) \\ \delta_{\hat{n}}^{(\xi)}\left(x,t,\tau\right) &= \widehat{\delta}_{\hat{n}}^{(\xi)}\left(x,t\right) + O\left(\eta\right) \end{aligned} \tag{4.22}$$

Likewise the leading order coarse-scale eigenstrain can be expressed as a function of the slow timescale coordinate t

$$\mu_{kl}^{c}\left(x,t,\tau\right) = \widehat{\mu}_{kl}^{c}\left(x,t\right) + O\left(\eta\right) \tag{4.23}$$

The coarse-scale equilibrium equation and the constitutive equation along with the initial and boundary conditions of the slow-evolving IBVP are obtained by time averaging the coarse-scale governing equations in (4.19) over fast time coordinate τ_o

$$\begin{aligned}
&\left\langle \sigma_{ij}^{c} \right\rangle_{,j}(x,t)+\left\langle b_{i}^{c} \right\rangle(x,t)=0 \quad \text{on} \quad \Omega\times[0,N],\\
&\left\langle \sigma_{ij}^{c} \right\rangle(x,t)=L_{ijkl}^{c}(x)\left(\left\langle \varepsilon_{kl}^{c} \right\rangle(x,t)-\widehat{\mu}_{kl}^{c}(x,t)\right) \quad \text{on} \quad \Omega\times[0,N],\\
&\left\langle \varepsilon_{ij}^{c} \right\rangle(x,t)=\left\langle u_{\left(i,x_j\right)}^{c} \right\rangle(x,t) \quad \text{on} \quad \Omega\times[0,N],\\
&\left\langle u_{i}^{c} \right\rangle(x,t)=\left\langle \overline{u}_{i}^{c} \right\rangle(x,t) \quad \text{on} \quad \partial\Omega^{u}\times[0,N],\\
&\left\langle \sigma_{ij}^{c} \right\rangle(x,t)n_j=\left\langle \overline{t}_{i}^{c} \right\rangle(x,t) \quad \text{on} \quad \partial\Omega^{t}\times[0,N].
\end{aligned} \tag{4.24}$$

To complete the definition of the coarse-scale-slow-time IBVP in (4.24), the partitioned eigenstrain $\dot{\widehat{\mu}}_{kl}^{(\alpha)}(x,t)\Big|_{K}$, and eigen-separation $\dot{\widehat{\delta}}_{\hat{n}}^{(\xi)}(x,t)\Big|_{K}$ growth rate over a single load cycle are calculated using finite difference method as follows

$$\begin{aligned}
\dot{\widehat{\mu}}_{kl}^{(\alpha)}(x,t)\Big|_{t=K} &= \mu_{kl}^{(\alpha)}(x,t=K,\tau=\tau_0)-\mu_{kl}^{(\alpha)}(x,t=K-1,\tau=0)\\
\dot{\widehat{\delta}}_{\hat{n}}^{(\xi)}(x,t)\Big|_{t=K} &= \widehat{\delta}_{\hat{n}}^{(\xi)}(x,t=K,\tau=\tau_0)-\widehat{\delta}_{\hat{n}}^{(\xi)}(x,t=K-1,\tau=0)
\end{aligned} \tag{4.25}$$

The phase eigenstrains and eigen-separations over Δt_K cycles from the current load cycle K can be approximated by employing the Euler's integration scheme

$$\begin{aligned}
\widehat{\mu}_{kl}^{(\alpha)}(x,t)\Big|_{t=K+\Delta t} &= \widehat{\mu}_{kl}^{(\alpha)}(x,t)\Big|_{t=K}+\dot{\widehat{\mu}}_{kl}^{(\alpha)}(x,t)\Big|_{t=K}\Delta t_K\\
\widehat{\delta}_{\hat{n}}^{(\xi)}(x,t)\Big|_{t=K+\Delta t} &= \widehat{\delta}_{\hat{n}}^{(\xi)}(x,t)\Big|_{t=K}+\dot{\widehat{\delta}}_{\hat{n}}^{(\xi)}(x,t)\Big|_{t=K}\Delta t_K
\end{aligned} \tag{4.26}$$

The relation in (4.26) is termed as the *predicto*r. The block cycle size Δt_K is chosen such that the maximum phase eigenstrains and eigen-separations are kept sufficiently small. The block cycle size is calculated as:

$$\Delta t_K=\operatorname{int}\left\{\max_{x_I\in\Theta^{(\beta)},\breve{x}_I\in S^{(\xi)}}\left(\Delta\widehat{\mu}_a/\left\|\Delta\widehat{\mu}^{(\beta)}\right\|,\Delta\widehat{\delta}_a/\left\|\Delta\widehat{\delta}^{(\xi)}\right\|\right)\right\} \tag{4.27}$$

where $\Delta\hat{\mu}_a$ and $\Delta\hat{\delta}_a$ are user-defined allowable phase eigenstrain and eigen-separation increments; $\left\|\Delta\hat{\mu}^{(\beta)}\right\|$ and $\left\|\Delta\hat{\delta}^{(\xi)}\right\|$ are the eigenstrain and eigen-separation increments obtained in a single cycle; $x_I \in \Theta^{(\beta)}$ and $\breve{x}_I \in S^{(\xi)}$ denote quadrature points in the phase and interface partitions, respectively.

The equilibrium equations in (4.19) will be violated if the eigenstrains and eigen-separations in (4.26) are only evolved while keeping the rest of the response fields unchanged. This inconsistency can be alleviated by performing a non-linear finite analysis at the end of the load cycle to equilibrate the discrete equilibrium equations, the process being termed as *consistency adjustment*.

A predictor-corrector scheme as described in Section 4.2 is employed to evaluate the eigenstrains and eigen-separations.

Given the above initial value of the block size Δt_K predict the eigenstrain and eigen-separation as

$$\begin{aligned}
\hat{\mu}_{kl}^{(\alpha)}(x,t)\Big|_{t=K+\Delta t_K}^{cor} &= \hat{\mu}_{kl}^{(\alpha)}(x,t)\Big|_{t=K} + \frac{\Delta t_K}{2}\left(\dot{\hat{\mu}}_{kl}^{(\alpha)}(x,t)\Big|_{t=K} + \dot{\hat{\mu}}_{kl}^{(\alpha)}(x,t)\Big|_{t=K+\Delta t_K}\right) \\
\hat{\delta}_{\breve{n}}^{(\xi)}(x,t)\Big|_{t=K+\Delta t_K}^{cor} &= \hat{\delta}_{\breve{n}}^{(\xi)}(x,t)\Big|_{t=K} + \frac{\Delta t_K}{2}\left(\dot{\hat{\delta}}_{\breve{n}}^{(\xi)}(x,t)\Big|_{t=K} + \dot{\hat{\delta}}_{\breve{n}}^{(\xi)}(x,t)\Big|_{t=K+\Delta t_K}\right)
\end{aligned} \tag{4.28}$$

Again, the relation in (4.28) is termed as the *corrector*. If the difference between the predictor in (4.26) and corrector in (4.28) is sufficiently small then the step is accepted and the aforementioned consistency adjustment is performed. Else, the block size is halved and the predictor-corrector step is repeated.

The governing equations for the coarse-scale-fast-time IBVP are obtained by subtracting the governing equations for the slow time scale IBVP in (4.24) from (4.19) , which yields the following linear strong form over $\Omega\times[0,\tau_0]$

$$\begin{aligned}
&\sigma^{c*}_{ij,j}(x,\tau)+b^{c*}_i(x,\tau)=0 \quad on \quad \Omega\times[0,\tau_0],\\
&\sigma^{c*}_{ij}(x,\tau)=L^{c}_{ijkl}(x)\varepsilon^{c*}_{kl}(x,\tau) \quad on \quad \Omega\times[0,\tau_0],\\
&\varepsilon^{c*}_{ij}(x,\tau)=u^{c*}_{(i,j)}(x,\tau) \quad on \quad \Omega\times[0,\tau_0],\\
&u^{c*}_i(x,\tau)=\overline{u}^{c*}_i(x,\tau) \quad on \quad \partial\Omega^u\times[0,\tau_0],\\
&\sigma^{c*}_{ij}(x,\tau)n_j=\overline{t}^{c*}_i(x,\tau) \quad on \quad \partial\Omega^t\times[0,\tau_0].
\end{aligned} \tag{4.29}$$

The constitutive equations in (4.24) and (4.29) are two way coupled. The fast timescale IBVP in (4.29) is solved at every time step of the slow timescale IBVP. Modeling of damage induced by fatigue and the numerical implementation aspects are given in Section 4.4 and Section 4.5 respectively.

4.4 Fatigue Damage Model

In cyclic loading, the damage accumulation due to fatigue depends on damage accumulation history, cyclic load amplitude and frequency, material properties, and environmental effects. In the present work, we employ continuum damage based fatigue model [27, 99]. By this approach we define a pseudo damage parameter $\hat{\omega}^{(\eta)}(x,t)\in[0,1]$ at a given time t as

$$\hat{\omega}^{(\eta)}(x,t)=\Phi\left(\left\{\vartheta^{(\eta)}(x,t)-\vartheta^{(\eta)}_{ini}\right\}_+\right), \qquad \frac{\partial\Phi\left(\left\{\vartheta^{(\eta)}(x,t)-\vartheta^{(\eta)}_{ini}\right\}_+\right)}{\partial\vartheta^{(\eta)}}\geq 0 \tag{4.30}$$

where $\vartheta^{(\eta)}$ is the phase equivalent strain (see [27, 99] for definition); $\vartheta_{ini}^{(\eta)}$ denotes the phase equivalent strain at onset of damage; $\Phi^{(\eta)}$ is the damage evolution law for each phase partition. The operator $\{\cdot\}_+$ denotes the positive part, i.e. $\{\cdot\}_+ = sup\{0,\cdot\}$. The phase damage parameter $\omega^{(\eta)}$ for quasistatic loading is defined as

$$\omega^{(\eta)}(x,t) = \max\left\{\hat{\omega}^{(\eta)}(x,t)\middle|\left(\tau \le t\right)\right\} \tag{4.31}$$

By incorporating the gauge function [112] defined as

$$\phi = \frac{\hat{\omega}^{(\eta)}}{\omega^{(\eta)}} = \frac{\Phi^{(\eta)}}{\omega^{(\eta)}} \tag{4.32}$$

the rate form of the phase damage law can be expressed as

$$\dot{\omega}^{(\eta)}\left(x,t\right) = \begin{cases} 0 & \vartheta^{(\eta)} < \vartheta_{ini}^{(\eta)} \\ \left(\dfrac{\Phi^{(\eta)}}{\omega^{(\eta)}}\right)^{\gamma^{(\eta)}} \dfrac{\partial \Phi^{(\eta)}}{\partial \bar{\vartheta}^{(\eta)}} \left\{\dot{\vartheta}^{(\eta)}\right\}_+ & \vartheta^{(\eta)} \ge \vartheta_{ini}^{(\eta)} \end{cases} \tag{4.33}$$

where $\gamma^{(\eta)}$ is the fatigue law material parameter for phase partition η; $\dfrac{\partial \Phi^{(\eta)}}{\partial \vartheta^{(\eta)}}\left\{\dot{\vartheta}^{(\eta)}\right\}_+$ represents the instantaneous quasistatic damage accumulation due to the phase equivalent strain $\vartheta^{(\eta)}$.

4.5 Implementation of the Space-Time Multiscale Homogenization Model

In this Section we focus on the implementation of the unified space-time multiscale homogenization model for high temperature CMC material system. The fibrous composite material microstructure comprises of matrix and tow phases. For simplicity, attention is restricted to evolution of damage in the phases only, assuming the interfaces to be perfectly bonded. Prior to the nonlinear analysis, the partitioned elastic strain influence functions, the eigenstrain influence functions [31-33] are pre-computed by solving the RVE problem.

4.5.1 Integration of Spatial Homogenization Model

The implementation of the reduced order spatial homogenization formulation involves evaluating the phase strains, eigen-fields and updating the phase stresses and the coarse-scale stresses. At any given slow time *t*, the coarse-scale strain $\varepsilon^{c}_{mn}\big|_t$, and the coarse-scale strain increment $\Delta\varepsilon^{c}_{mn}$ are known at the beginning of the load increment. The goal is to update the overall coarse-scale strain ε^{c}_{mn}, the phase strain $\varepsilon^{(\eta)}_{mn}$, the phase damage parameter $\omega^{(\eta)}$, the damage phase equivalent strain $\overline{\vartheta}^{(\eta)}$, the phase stresses $\sigma^{(\eta)}_{mn}$ and the overall coarse-scale stress σ^{c}_{mn}. The update algorithm is outlined below.

(i) Update the overall coarse scale strain $\varepsilon^{c}_{mn} = \varepsilon^{c}_{mn}\big|_t + \Delta\varepsilon^{c}_{mn}$

(ii) Solve the nonlinear equation (2.30) to evaluate the strain fields in the phases at the fine scale. Compute the phase damage equivalent strain $\vartheta^{(\eta)}$

(iii) Check if the process is inelastic, i.e. $\vartheta^{(\eta)} > \vartheta^{(\eta)}_{ini}$. If process is inelastic, update the phase damage parameter $\omega^{(\eta)}$ by integrating equation (4.33) using backward Euler scheme such that

$$\aleph \equiv \omega^{(\eta)} - \omega^{(\eta)}\Big|_t - \left[\frac{\Phi^{(\eta)}}{\omega^{(\eta)}}\right]^{\gamma^{(\eta)}}\Bigg|_{t+\Delta t} \left[\frac{\partial \Phi^{(\eta)}}{\partial \vartheta^{(\eta)}}\right]\Bigg|_{t+\Delta t} \left(\vartheta^{(\eta)} - \vartheta^{(\eta)}\Big|_t\right) = 0 \qquad (4.34)$$

The above equation is nonlinear in $\omega^{(\eta)}$ and is solved using the Newton iteration as

$${}^{i+1}\omega^{(\eta)} = {}^{i}\omega^{(\eta)} - \left[\left(\frac{\partial \aleph^{(\eta)}}{\partial \omega^{(\eta)}}\right)^{-1} \aleph^{(\eta)}\right]\Bigg|_{{}^{i}\omega^{(\eta)}} \qquad (4.35)$$

where the left superscript denotes iteration count.

(iv) If the process is elastic, then $\omega^{(\eta)} = \omega^{(\eta)}\Big|_{t}$

(v) Update the phase eigenstrain $\mu_{mn}^{(\eta)}$ using the constitutive relation in (2.34)

(vi) Update the coarse-scale stress σ_{mn}^{c} using equation (2.38)

(vii) For an implicit solver compute the coarse scale consistent tangent tensor using equation (2.44)

A detailed schematic of the two scale reduced order spatial homogenization model is depicted in Figure 36 below.

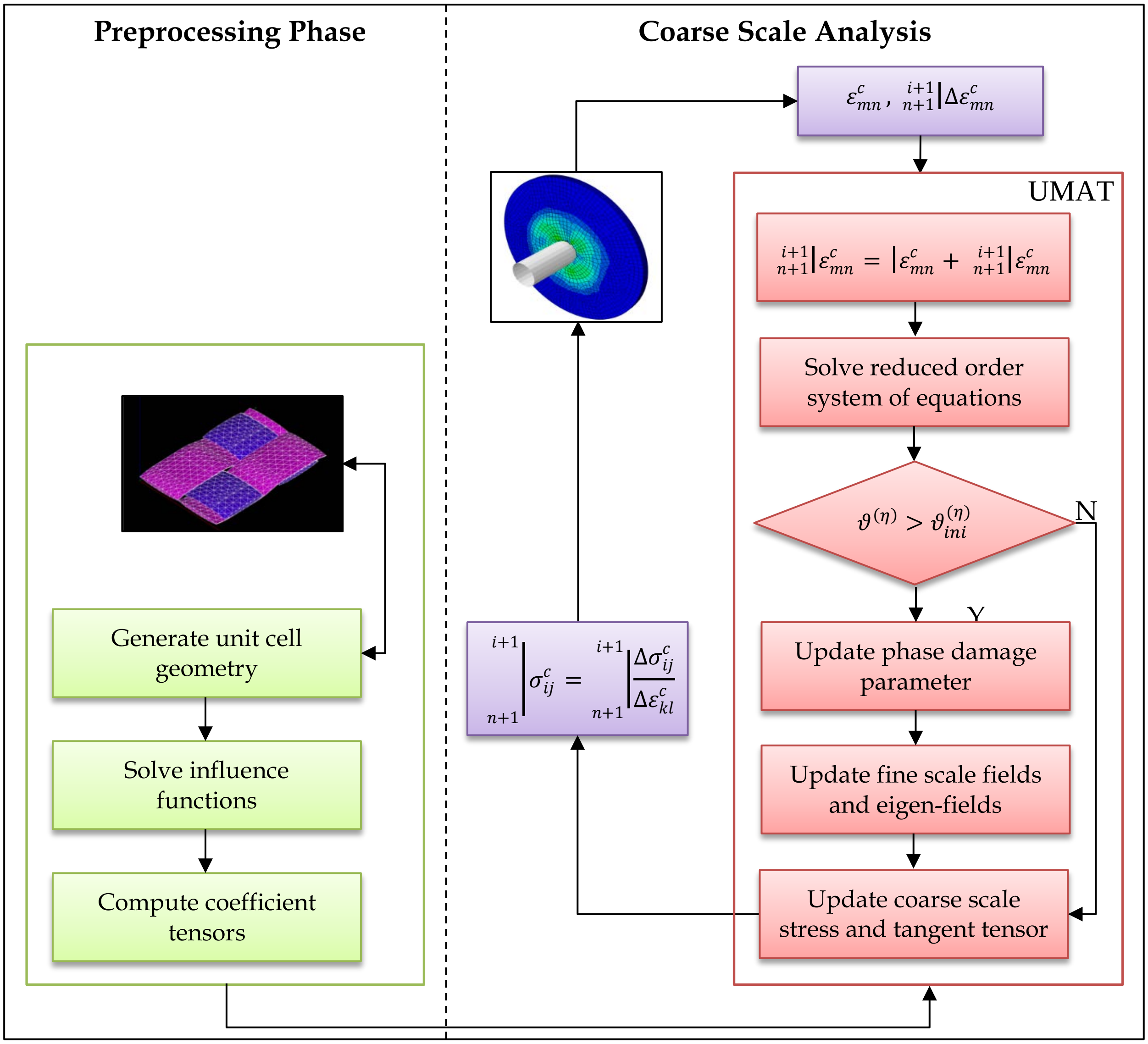
Preprocessing Phase
Coarse Scale Analysis
$\varepsilon^c_{mn}, \ {}^{i+1}_{n+1}|\Delta\varepsilon^c_{mn}$
UMAT
${}^{i+1}_{n+1}|\varepsilon^c_{mn} = |\varepsilon^c_{mn} + {}^{i+1}_{n+1}|\varepsilon^c_{mn}$
Solve reduced order system of equations
$\vartheta^{(\eta)} > \vartheta^{(\eta)}_{ini}$
N
Y
Update phase damage parameter
Update fine scale fields and eigen-fields
Update coarse scale stress and tangent tensor
${}^{i+1}_{n+1}\Big|\sigma^c_{ij} = {}^{i+1}_{n+1}\Big|\frac{\Delta\sigma^c_{ij}}{\Delta\varepsilon^c_{kl}}$
Generate unit cell geometry
Solve influence functions
Compute coefficient tensors

Figure 36: Schematic of the two scale reduced order homogenization model

4.5.2 Integration of Temporal Homogenization Model

Consider time *t* in the slow time scale at the beginning of a load cycle K-1, where the fine scale fields and coarse-scale fields are known at time *t*. Perform an incremental finite element analysis for one load cycle as mentioned in Section 4.5.1, wherein the coarse-scale strain $\varepsilon^c_{mn}\big|_{K-1}$, the coarse-scale strain increment $\Delta\varepsilon^c_{mn}$, the phase damage parameter $\omega^{(\eta)}\big|_{K-1}$ and the phase strain $\varepsilon_{mn}^{(\eta)}\Big|_{K-1}$ are known at the beginning of the load cycle. To update the phase damage parameter $\omega^{(\eta)}\Big|_{K}$ it is necessary to integrate the phase damage parameter in equation (4.33) over the loading path as

$$\int_{t}^{t+\tau_0} \dot{\omega}^{(\eta)}\left(x,t\right)dt = \int_{t}^{t+\tau_0} \left(\frac{\Phi^{(\eta)}}{\omega^{(\eta)}}\right)^{\gamma^{(\eta)}} \frac{\partial \Phi^{(\eta)}}{\partial \vartheta^{(\eta)}} \left\langle \dot{\vartheta}^{(\eta)} \right\rangle_{+} \tag{4.36}$$

where t is the slow time scale coordinate at the beginning of the load cycle and τ_0 is the load cycle period. Since the phase damage growth rate over a single cycle is very small the damage growth rate over a number of cycles may be approximated as

$$\frac{d\omega^{(\eta)}}{dt}(x,t)\Bigg|_{t=K} \approx \int_{t}^{t+\tau_0} \dot{\omega}^{(\eta)} dt \equiv \Delta\omega^{(\eta)}\Big|_{t=K} = \omega^{(\eta)}\Big|_{K} - \omega^{(\eta)}\Big|_{K-1} \tag{4.37}$$

The above equation is similar to equation (4.25) wherein the eigenstrain is a function of the coarse-scale strain and the phase damage parameter.

Similar to equation (4.26) the phase damage over a block size Δt_K is computed using the forward Euler integration rule

$$\omega^{(\eta)}\Big|_{(K+\Delta t_K)} = \omega^{(\eta)}\Big|_{K} + \Delta t_K \Delta\omega^{(\eta)} \tag{4.38}$$

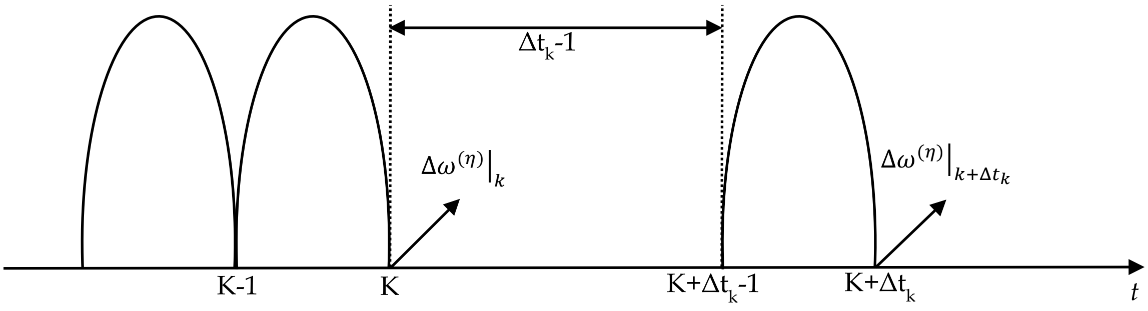

Figure 37: Adaptive block scheme for fatigue life estimation

To ensure consistency of the solution, it is necessary to equilibrate the discrete equilibrium equations at the end of the load cycle. The criterion for choosing the block cycle Δt_K is specified in equation (4.27). To control the accuracy of the block cycle scheme the phase damage parameter is also calculated based on the average growth rates at $\Delta\omega^{(\eta)}\big|_K$ and $\Delta\omega^{(\eta)}\big|_{(K+\Delta t_K)}$ as illustrated in Figure 37.

$$\omega^{(\eta)}\Big|_{(K+\Delta t_K)}^{cor} = \omega^{(\eta)}\Big|_K + \frac{\Delta t_K}{2}\left(\Delta\omega^{(\eta)}\Big|_K + \Delta\omega^{(\eta)}\Big|_{(K+\Delta t_K)}\right) \tag{4.39}$$

If the difference between the predictor (4.38) and corrector (4.39) is small the block cycle size is accepted and the fatigue life is updated as

$$t_{\max} = n + \sum_{K=1}^{n} \Delta t_K ; \quad \Delta t_K \geq 0 \tag{4.40}$$

where *n* is the number of the cycle blocks in the loading history. If the difference between the predicted and corrected values is large, then the block cycle size is halved and the predictor-corrector algorithm is repeated. The predictor-corrector integration algorithm is summarized below.

(i) Let time *t*, be the time in the loading history corresponding to $(K-1)^{th}$ cycle.

(ii) Perform an incremental finite element analysis for one load cycle as mentioned in Section 4.5.1 with the coarse-scale strain as $\varepsilon^c_{mn}\big|_{K-1}$ and the phase damage parameter as $\omega^{(\eta)}\big|_{K-1}$. The computed phase damage at the end of the load cycle is denoted by $\omega^{(\eta)}\big|_{K}$

(iii) Calculate the initial block cycle size Δt_K in equation (4.27).

(iv) Compute the phase damage parameters $\omega^{(\eta)}\big|_{(K+\Delta t_K)}$ and $\omega^{(\eta)}\big|^{cor}_{(K+\Delta t_K)}$ using the forward Euler integration in equation (4.38).

(v) Check for convergence

$$maxGauss\left\{\left| \omega^{(\eta)}\big|_{(K+\Delta t_K)} - \omega^{(\eta)}\big|^{cor}_{(K+\Delta t_K)} \right|\right\} \le err \tag{4.41}$$

where err is the user-defined error tolerance

(vi) If criterion in (4.41) is satisfied, update damage parameter by $\omega^{(\eta)}\big|_{(K+\Delta t_K)}$, fine scale fields and eigen-fields and fatigue life $t_{\max}$ in equation (4.40).

(vii) Perform consistency adjustment by first computing the phase stresses $\sigma^{(\eta)}_{mn}\big|_K$ followed by coarse-scale stress $\sigma^c(x)\big|_K$. Equilibrate the discrete equilibrium equations at the coarse scale. Repeat steps 1-8 for the next load cycle K+1.

(viii) If criterion in (4.41) is not satisfied then, halve the time step, $\Delta t_K = \Delta t_K / 2$, and repeat the above steps until equation (4.41) is satisfied.

The schematic of the implementation of the unified space-time multiscale formulation is depicted in Figure 38 below.

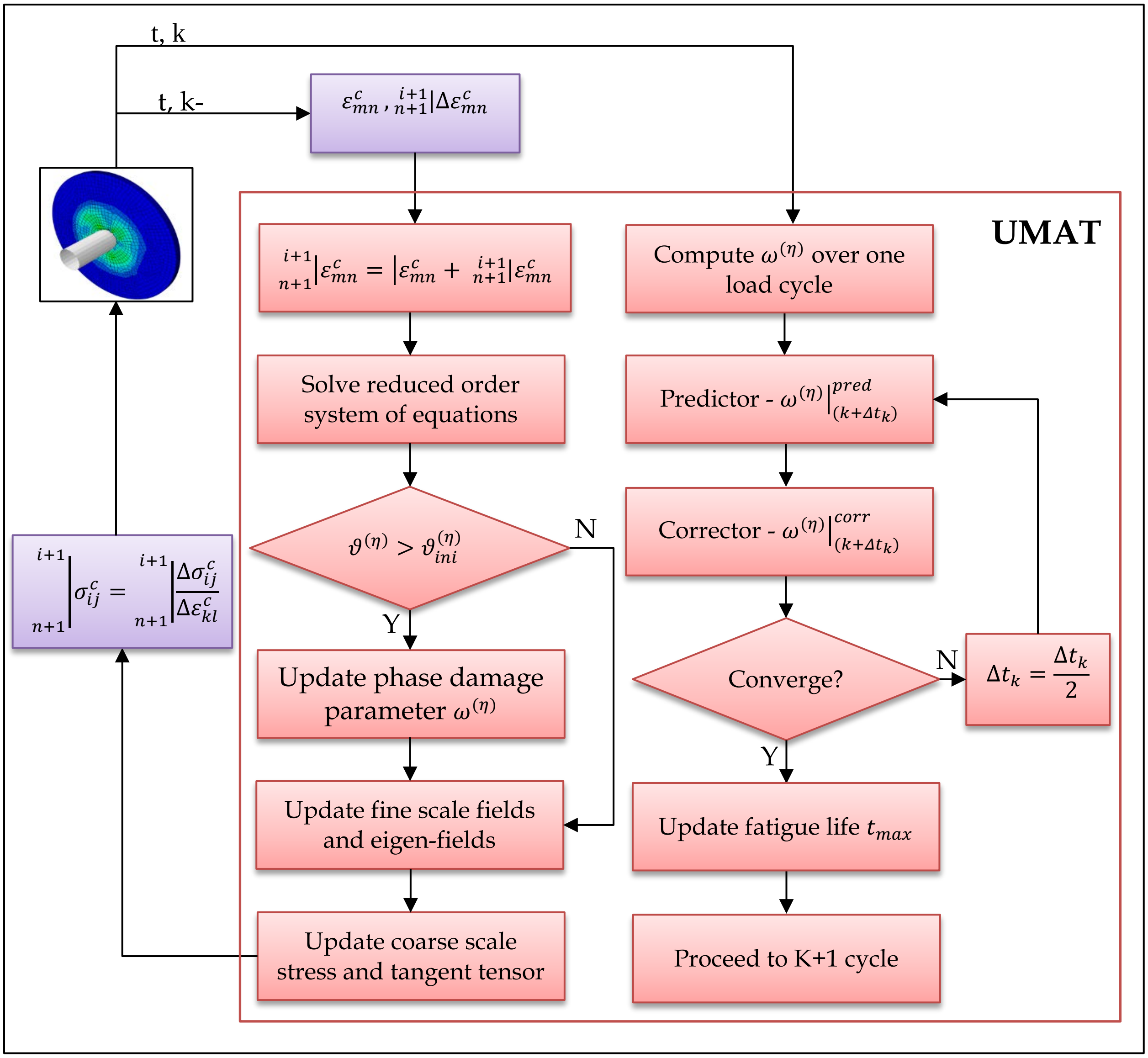
t, k
t, k-
$\varepsilon^c_{mn}, {}^{i+1}_{n+1}|\Delta\varepsilon^c_{mn}$
UMAT
${}^{i+1}_{n+1}|\varepsilon^c_{mn} = |\varepsilon^c_{mn} + {}^{i+1}_{n+1}|\varepsilon^c_{mn}$
Compute $\omega^{(\eta)}$ over one load cycle
Solve reduced order system of equations
Predictor - $\omega^{(\eta)}|^{pred}_{(k+\Delta t_k)}$
Corrector - $\omega^{(\eta)}|^{corr}_{(k+\Delta t_k)}$
$\vartheta^{(\eta)} > \vartheta^{(\eta)}_{ini}$
N
Y
${}^{i+1}_{n+1}|\sigma^c_{ij} = {}^{i+1}_{n+1}|\frac{\Delta\sigma^c_{ij}}{\Delta\varepsilon^c_{kl}}$
Converge?
N
$\Delta t_k = \frac{\Delta t_k}{2}$
Y
Update phase damage parameter $\omega^{(\eta)}$
Update fine scale fields and eigen-fields
Update fatigue life t_{max}
Update coarse scale stress and tangent tensor
Proceed to K+1 cycle

Figure 38: Schematic of the unified multi space-time homogenization framework

4.6 Validation of the Space-Time Multiscale Homogenization Model

In this section, the validation of the unified space-time multiscale formulation for fatigue life analysis of a six-layer, five harness satin weave, CMC is presented. The validation study consists of two stages. In the first phase the fatigue damage model described in Section 4.4 is validated against experimental uniaxial tensile test results of the CMC material system at various elevated temperatures. The second stage consists of validation of the fatigue life prediction model described in Section 4.5.2. The microstructure of the composite is assumed to be a two-phase periodic material consisting of tows and matrix. The unit cell of the ceramic composite is given in Figure 39.

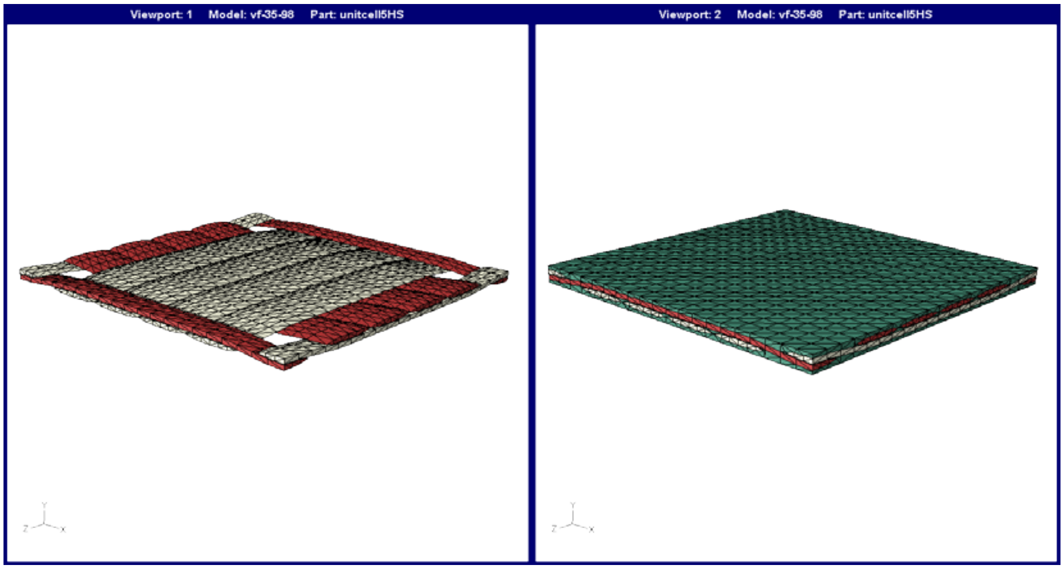
Viewport: 1 Model: vf-35-98 Part: unitcell5HS
Viewport: 2 Model: vf-35-98 Part: unitcell5HS

Figure 39: Unit cell model (21767 elements, 4298 nodes)

4.6.1 Validation of Fatigue Damage Model

Prior to making the fatigue life predictions it is necessary to validate the fatigue damage model and optimize the phase elastic and inelastic properties in order to match the coarse scale response with the experimental response. We consider an isotropic linear damage model for matrix and tow phases with phase damage variables $\omega^{(mat)}, \omega^{(tow)}$ being piecewise-continuous function of phase damage equivalent strains $\vartheta^{(mat)}, \vartheta^{(tow)}$ respectively, as shown in Figure 40.

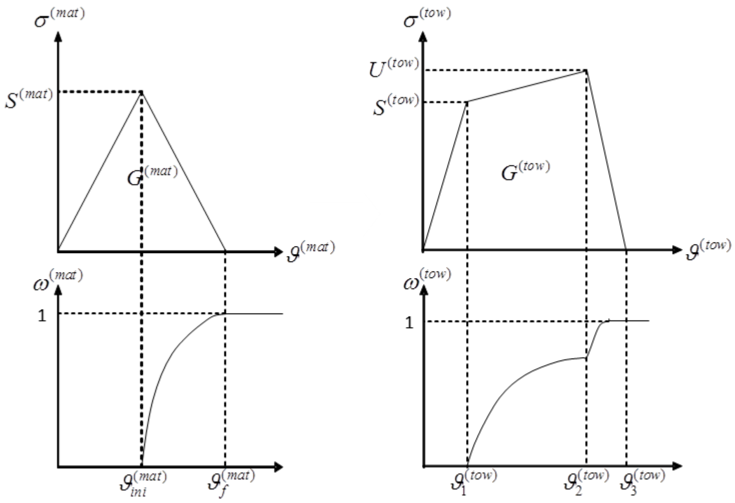

Figure 40: Piecewise damage evolution functions for matrix phase (left) and tow phase (right)

The piecewise linear damage model for matrix phase is defined as:

$$\omega^{(mat)} = \begin{cases} 0 & \vartheta^{(mat)} < \vartheta_{ini}^{(mat)} \\ \omega_{\max}^{(mat)} \dfrac{\vartheta^{(mat)} - \vartheta_{ini}^{(mat)}}{\vartheta_{f}^{(mat)} - \vartheta_{ini}^{(mat)}} & \vartheta_{ini}^{(mat)} \le \vartheta^{(mat)} \le \vartheta_{f}^{(mat)} \\ \omega_{\max}^{(mat)} & \vartheta^{(mat)} > \vartheta_{f}^{(mat)} \end{cases} \tag{4.42}$$

where

$$\vartheta_{ini}^{(mat)} = S^{(mat)} / E^{(mat)}$$

$$\vartheta_{f}^{(mat)} = \left(-S^{(mat)} + \sqrt{24 G^{(mat)} E^{(mat)} - 3\left(S^{(mat)}\right)^2} \right) / 2E^{(mat)}$$

$$\vartheta^{(mat)} = max \left\{ \sqrt{\sum_{I=1}^{3} \left(\left\{ \varepsilon_I^{(mat)}(t) \right\}_+ \right)^2} \right\}$$

and $\varepsilon_I^{(mat)}$, $S^{(mat)}$, $G^{(mat)}$ and $E^{(mat)}$ denote the maximum principal eigenstrain, the yield stress, the strain energy density, and the elastic modulus in the matrix phase, respectively.

The piecewise linear damage model for the tow phase is defined as:

$$\omega^{(tow)} = \begin{cases} 0 & \vartheta^{(tow)} < \vartheta_1 \\ 1 - \left(\dfrac{U^{(tow)} - S^{(tow)}}{E^{(tow)}}\right)\left[\left(\dfrac{U^{(tow)}}{U^{(tow)} - S^{tow)}} - \dfrac{\vartheta_2}{\vartheta_2 - \vartheta_1}\right)\dfrac{1}{\vartheta^{(tow)}} + \dfrac{1}{\vartheta_2 - \vartheta_1}\right] & \vartheta_1 \le \vartheta^{(tow)} < \vartheta_2 \\ 1 - \dfrac{U^{(tow)}}{E^{(tow)}}\left[\left(\dfrac{\vartheta_3}{\vartheta_3 - \vartheta_2}\right)\vartheta^{(tow)} - \dfrac{1}{\vartheta_3 - \vartheta_2}\right] & \vartheta_2 \le \vartheta^{(tow)} < \vartheta_3 \\ 1 & \vartheta^{(tow)} \ge \vartheta_3 \end{cases} \tag{4.43}$$

where $\vartheta_1 = S^{(tow)} / E^{(tow)}$ and $\vartheta^{(tow)} = max\left\{\sqrt{\sum_{I=1}^{3}\left(\left\{\varepsilon_I^{(tow)}(t)\right\}_+\right)^2}\right\}$

The optimization of the phase material properties is conducted by solving an inverse problem wherein the error between the experimental observation and simulation is minimized

$$min \quad \frac{1}{2}F(x)^T F(x) = \frac{1}{2}\sum_{i=1}^{a} w_i\left[exp\_data_i - sim\_data_i(x)\right]^2 \tag{4.44}$$

where w_i denotes weights reflecting the confidence level in various observations.

First, a quasi-static uniaxial tensile test is performed to characterize quasistatic material parameters. The coarse scale finite element model of the uniaxial tensile test is presented in Figure 41.

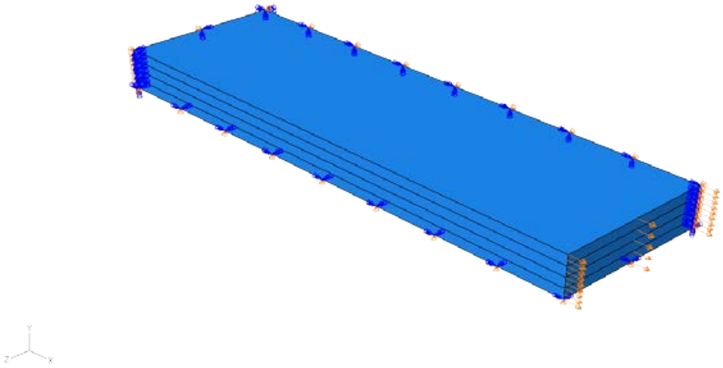

Figure 41: ¼th simulation model of eight-layer, five harness satin weave, ceramic composite

The matrix and tow phase properties were optimized for temperatures 2100F, 2300F and 2400F. Once these properties have been characterized the simulation results agree very well with the experimental results for all temperatures considered as shown in Figure 42. The evolution of damage in the tows and the matrix is shown in Figure 43 to Figure 45.

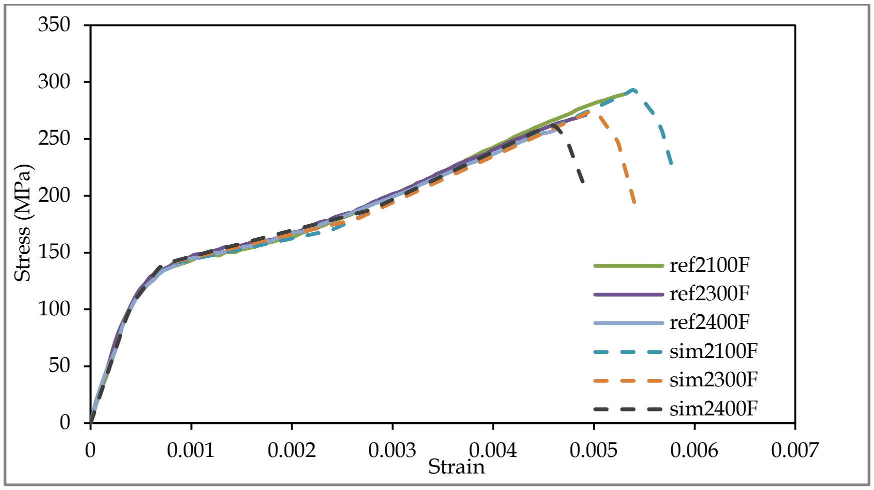

Figure 42: Comparison between experimental and simulation stress-strain curves

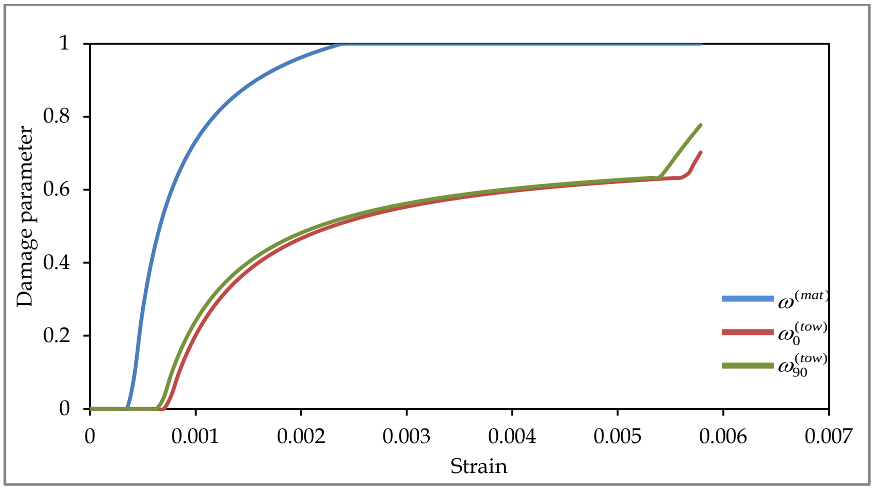

Figure 43: Damage evolution as a function of the phase equivalent strain at 2100F

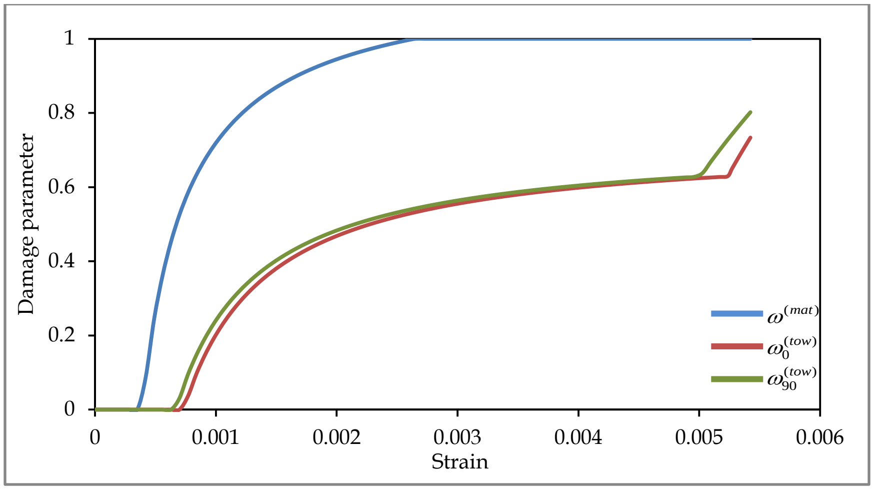

Figure 44: Damage evolution as a function of the phase equivalent strain at 2300F

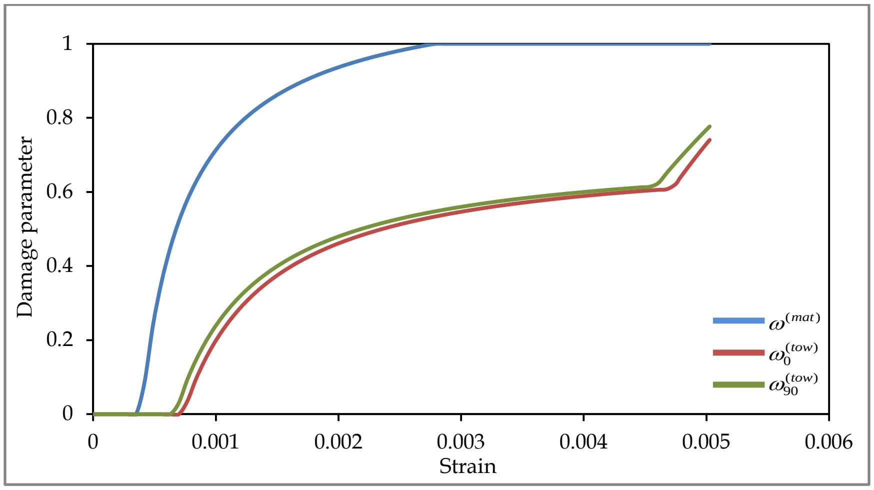

Figure 45: Damage evolution as a function of the phase equivalent strain at 2400F

4.6.2 Validation of Fatigue Life Prediction Model

The power law exponent $\gamma^{(\eta)}$ in equation (4.33) for each phase controls the damage growth rate. In this Section we optimize the exponent $\gamma^{(\eta)}$ to match the simulation response with the response of experiments conducted at a low frequency of 1Hz and a high frequency of 60Hz for varying load amplitudes and temperatures. We employ a bilinear discretization of $\gamma^{(\eta)}$ in the space of load frequency (1Hz, 60Hz), amplitude (83MPa, 97MPa, 124MPa) and temperature (2100F, 2300F and 2500F). The test coupon is set to fail when the damage in either of matrix phase or tow phases reaches a critical value.

Comparison between the simulation and experimental results are presented in Figure 46 to Figure 55. The results indicate that failure in the matrix phase occurs prior to failure in the tows. The dependence of $\gamma^{(mat)}$ on loading frequency, amplitude and temperature is depicted in Figure 49 and Figure 50 for the low cycle fatigue and in Figure 54 and Figure 55 for the high cycle fatigue. Several observations can be made. It can be seen that for the 1Hz cyclic load case, the exponent $\gamma^{(\eta)}$ is less sensitive to the temperature variations at smaller load amplitudes. However for the 60Hz case the exponent $\gamma^{(\eta)}$ is sensitive to the temperature variations even at low load amplitudes.

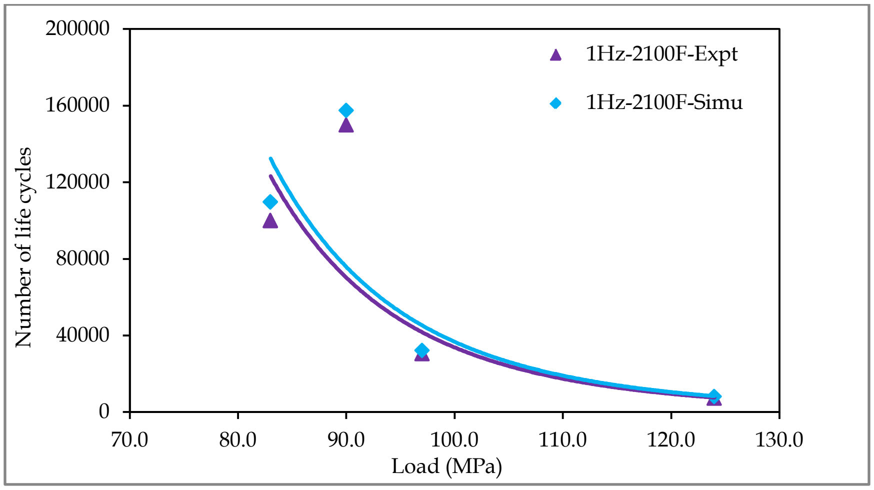

Figure 46: Simulation vs experimental results at 1Hz and 2100F

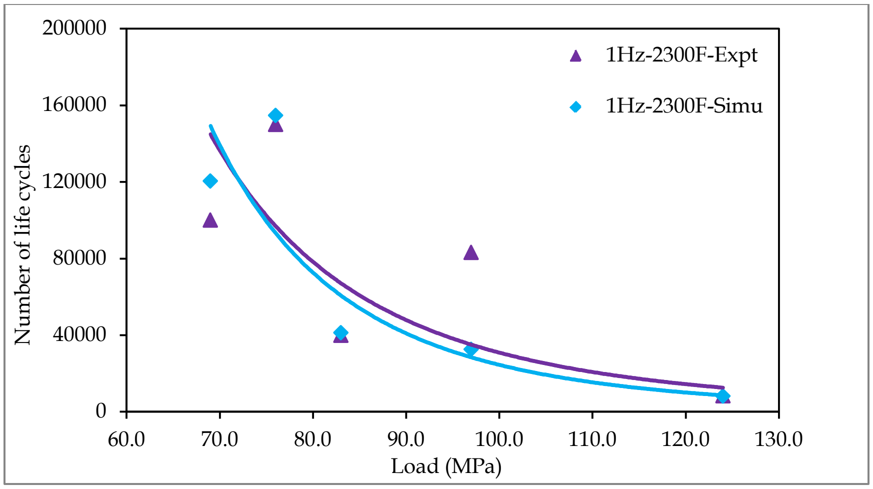

Figure 47: Simulation vs experimental results at 1Hz and 2300F

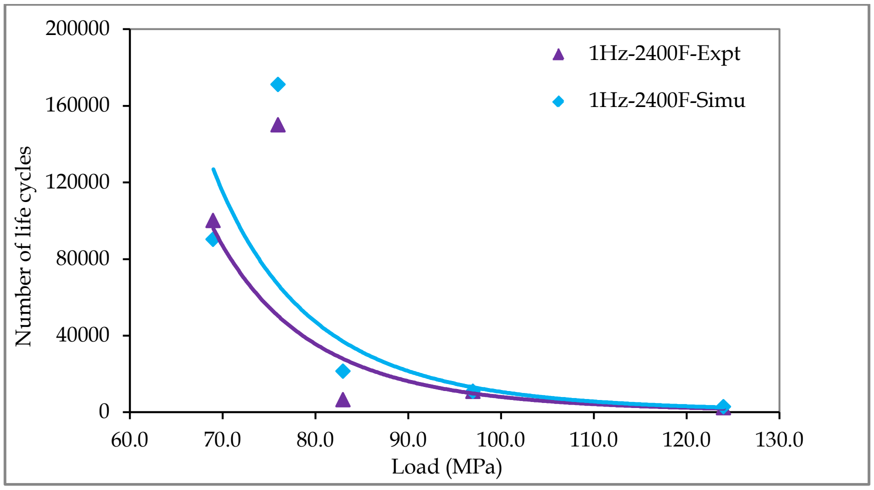

Figure 48: Simulation vs experimental results at 1Hz and 2400F

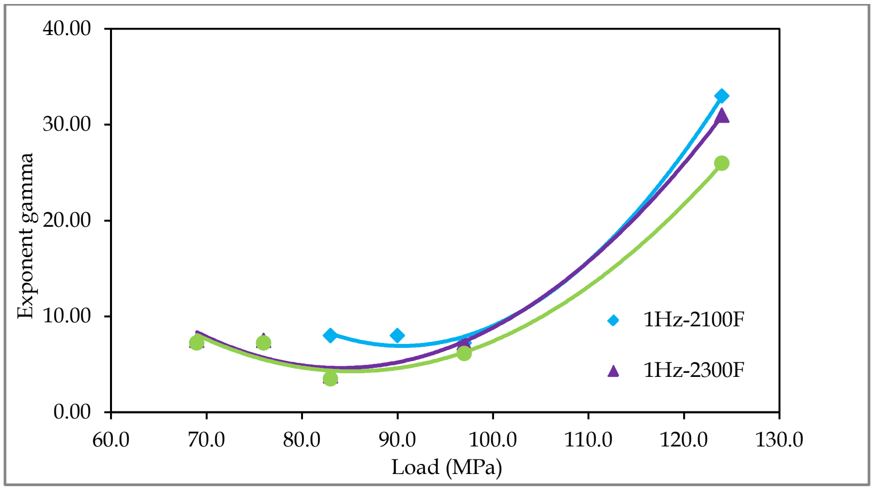

Figure 49: Gamma exponent vs load for varying temperatures at 1Hz

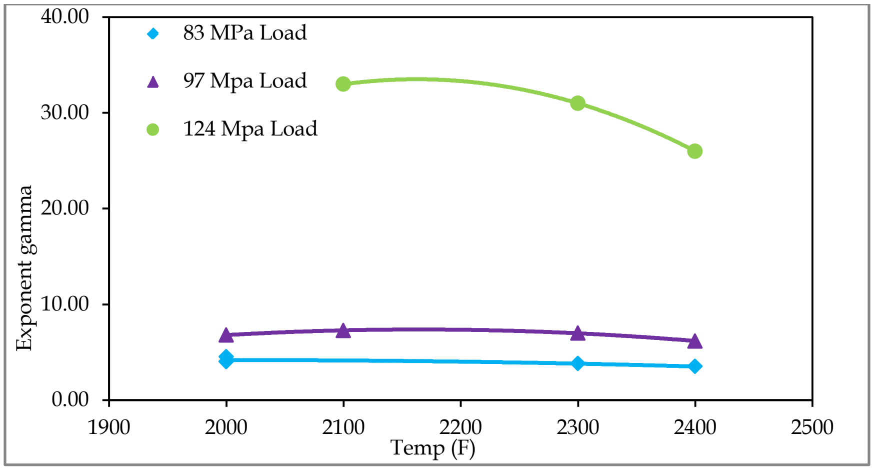

Figure 50: Gamma exponent vs temperature for varying loads at 1Hz

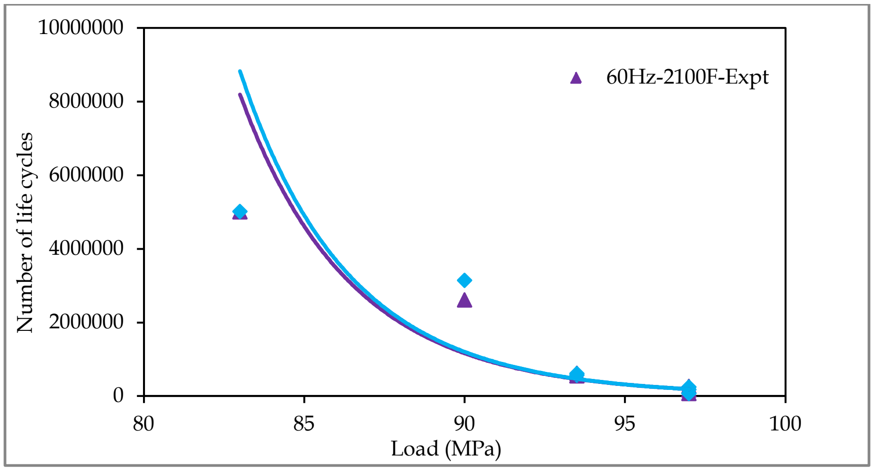

Figure 51: Simulation vs experimental results at 60Hz and 2100F

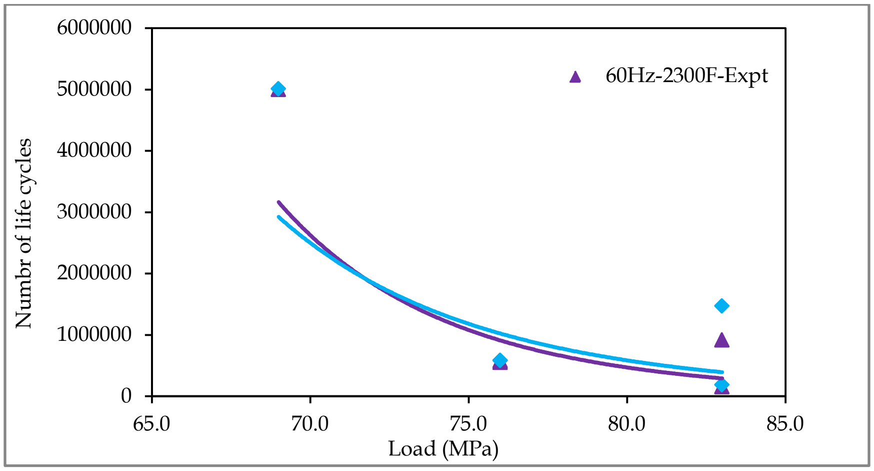

Figure 52: Simulation vs experimental results at 60Hz and 2300F

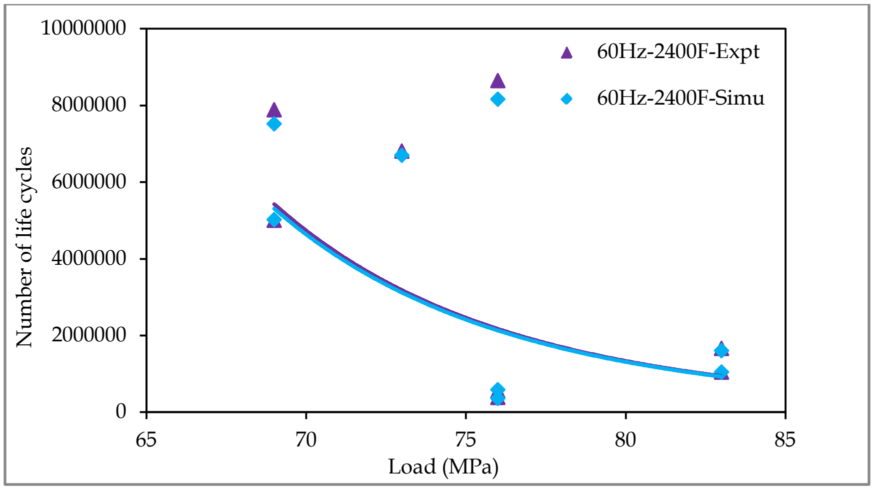

Figure 53: Simulation vs experimental results at 60Hz and 2400F

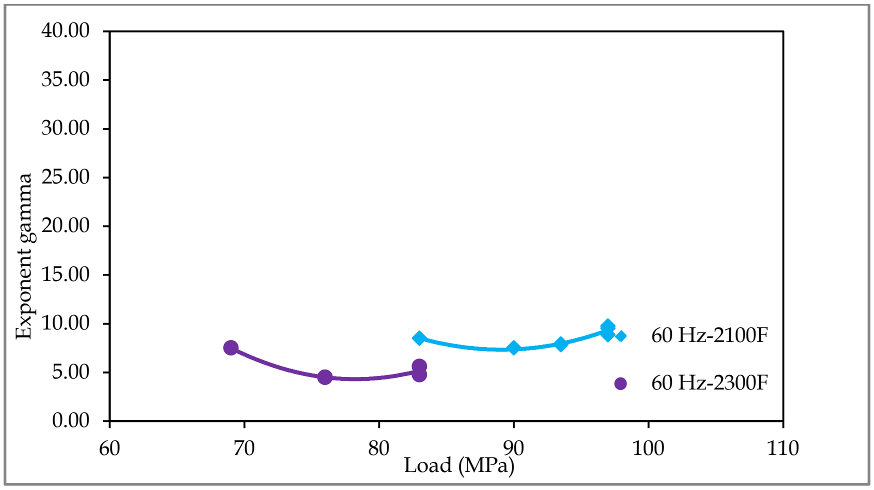

Figure 54: Gamma exponent vs load for various temperatures at 60Hz

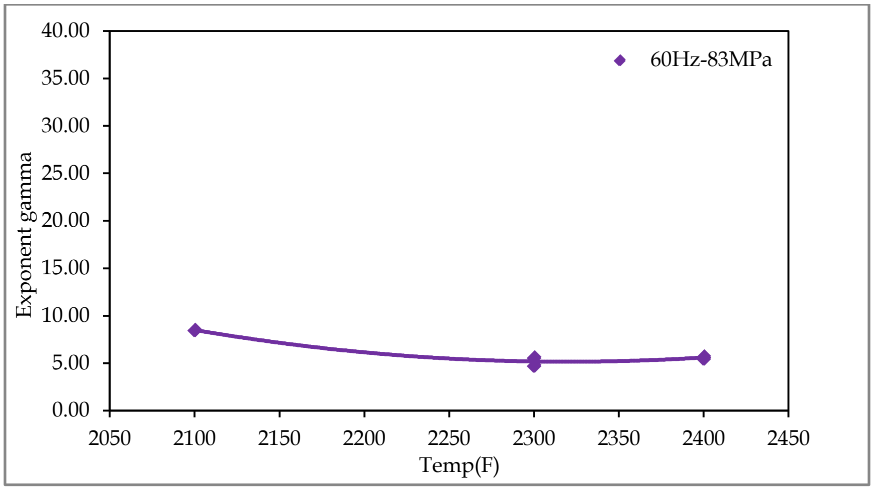

Figure 55: Gamma exponent vs temperature for various loads at 60 Hz

4.7 Discussion

The fatigue damage model does an excellent job of fitting the tensile behavior of the five harness satin fabric CMC and quite a good job of fitting the fatigue behavior. More importantly, the behavior of the damage rate parameter seems consistent with the mechanical behavior of the ceramic composite. However, the extent of the cyclic damage captured by the current model and any time dependent damage that is not explicitly modeled is unclear. This uncertainty is due to the fact that these are short duration tests, about million plus cycles in 5 hours for the 60Hz case. The duration presumably emphasizes "mechanical" damage, and the current model captures the change in strength due to the increasing temperature. Above 2300F, temperature increases do not change the strength significantly, resulting in similar fatigue lives.

Looking at the details of the results, for a frequency of one Hertz, Figure 50 shows that the gamma parameter is primarily a function of load amplitude, showing very little dependence upon the influence of temperature. There is some impact of temperature at higher load amplitudes. Again, recall the relatively short duration of the 1 Hertz tests. At this frequency, the longest test is about two days. Thus, the occurrence of time dependent damage progression is modest. At 60 Hertz frequency and load amplitudes lesser than 100 MPa, the behavior of gamma is same when compared to the 1Hz case as depicted in Figure 54.

Figure 55 shows a decrease in the gamma exponent as the temperature increases from 2100F to 2300F, and then is approximately constant for a further 100F increase. At this load of 83 MPa, the composite matrix will show some amount of cracking, thus providing entry for the environment and potential time dependent damage. At the low temperature, the damage rate is not as severe but increasing temperature increases the damage, reaching some saturation between 2300 and 2400F. This mechanism is consistent with the model results shown in Figure 50 for the 1 Hertz fatigue.

In summary, the model captures the monotonic and cyclic damage behavior in a CMC material. By incorporating the monotonic behavior into the cyclic model, the model is capable of describing the fatigue damage in a manner that is consistent with the damage mechanisms observed in the ceramic matrix composites. The cyclic model is calibrated from the results of fatigue experiments with high and low frequency triangular waveforms at varying load amplitudes and temperatures. These experiments are relatively short in duration, therefore limiting the opportunity for occurrence of time dependent damage. Further data is required to determine how the model can be extended to other waveforms including hold times and slower frequencies. It is anticipated that such an extension might require an explicit time dependent function.

4.8 Conclusions

In this chapter, the assumption of slow progression of damage and subsequent degradation of material properties in comparison to the fast time scale cyclic loading allowed us to separate the time scales. The temporal homogenization formulation was developed in Section 4.2. The reduced order spatial and temporal homogenization models were integrated into a unified formulation in Section 4.3. The unified space-time multiscale homogenization formulation was validated for fatigue life analysis of ceramic matrix composites. A continuum damage mechanics based model was employed for modeling the fatigue induced damage and progression. The damage evolution in the matrix and tow phases was modeled with piecewise-continuous functions of the equivalent strains in the phases. Predictions show good agreement with experimental results. The model is consistent with the damage mechanisms observed for the composite undergoing monotonic and high frequency cycling. This methodology may be implemented in the development of a structural design tool for CMC hot flow path components.

PART V

MULTISCALE-MULTIPHYSICS HOMOGENIZATION

Chapter 5

Multiscale-Multiphysics Homogenization for Heterogeneous Materials

In this chapter the kinetics of moisture diffusion in fiber reinforced thermoplastics and the influence of moisture on physical and mechanical properties are studied. A coupled-multiphysics model is developed to capture the complex behavior of thermoplastic material systems in the presence of moisture. The coupled-multiphysics model is integrated with the spatial homogenization model to develop a unified multiscale-multiphysics theory to analyze problems consisting of multiple length scales and coupled-multiple physics problems. The unified framework is validated for analyzing moisture diffusion and degradation of physical and mechanical properties of glass and carbon fiber filled thermoplastic material systems.

5.1 Introduction

If one was to try and pinpoint the birth of composites in the automotive sector, then the 1953 General Motors Motorama would be a good candidate. It was at this event that the Chevrolet Corvette was first unveiled [113]. While General Motors is considered to be a pioneer in utilization of polymer matrix composites in automotive industry, there has been little widespread adoption within the mass production sector. However, there is ample of evidence that this state of affairs is rapidly changing. Recent DOT report [114] identified weight reduction through lightweight materials as one of the best ways to achieve the reduction of energy consumption, lower emissions, and improve safety. Lovins and Cramer [115] and Jackson and Schlesinger [116] estimated that fuel economy would improve 5% to 7% for every 10% vehicle weight reduction and a CO_2 emissions reduction of 20 kg for every kg of vehicle weight reduction. With 75% of vehicle gas (energy) consumption directly related to factors associated with vehicle weight, the potential benefits of weight reduction will enable smaller engine and battery, with corresponding cost and/or performance benefits.

The enormous gains offered by polymer matrix composites for automotive applications are well documented [117]. Yet, their lack of predictability in automotive fluid environment and operating atmospheres (e.g. distilled water, saltwater, high humidity, windshield washer, engine coolant, motor oil, brake fluid, gasoline, battery acid) has often resulted in overdesign and thus limited their insertion in load bearing components since the overdesigned component may not yield any design advantages. There are several reasons for this state of affairs: (i) existence of multiple spatial scales and multiple coupled physical processes including, such as thermal, mechanical and moisture diffusion; and (ii) costly environmental degradation experiments that require long time exposure of the test specimens to varied levels of humidity and temperature conditions.

Among the variants of thermoplastics, short fiber thermoplastics have been increasingly used in the automotive industry as they are less dense than traditional materials. Their usage is specifically intended to fill the gap in the mechanical properties offered by continuous-long fiber composites primary used as structural members and the mechanical properties offered by unreinforced polymer products used as non-load bearing members. Glass and carbon short fibers are mainly used as the filling medium with polyamides (PA/Nylon) or polyphthalamides (PPA), commonly known as partially aromatic polyamides being the base material. Their applications are mainly in body parts: door panels, hoods, bonnets, bumpers; engine parts including cam covers, engine mounts, fuel tanks, fuel cells and interior trims including molded seats. They enjoy such a great demand due to the factors like manufacturing ease, versatility, low cost, corrosion resistance and superior mechanical, thermal and electrical properties.

Polyamides of semi-crystalline composition are known to absorb moisture due to their hydrophilic characteristics. Experimental studies for PA-6, PA-66 and PA-46 report an equilibrium moisture content varying in the range from 1.2 wt.% to 2.5 wt.% at 50% RH and

$23\ ^{o}C$ temperatures and about 8 wt.% to 9 wt.% upon reaching saturation conditions [118-121]. The moisture is first absorbed in to the micro and macro cracks/voids and eventually reaches the areas surrounding the fiber matrix interfaces. The absorbed moisture breaks the inter-catenary polymer-polymer hydrogen bonds to form water-polymer bonds. The net effect is plasticization of the matrix leading to molecular mobilization of the structural units. The absorbed moisture induces swelling in the matrix whereas the fibers remain impermeable resulting in a differential stress state at the interface, eventually weakening the interfacial strength.

The mechanical and physical properties of thermoplastics are mainly dependent upon the molecular mobility of the structural chains [122]. The temperature at which the molecular chains acquire mobility is called the glass transition temperature T_g. Therefore the mobilization of the structural chains due to moisture ingression causes a monotonic decrease in the glass transition temperature [123, 124]. The Young's modulus is dependent upon the concentration of the inter-catenary hydrogen bonds (7). Since the absorbed moisture breaks the inter-catenary hydrogen bonds a reversible loss in strength and stiffness, consistent with the decrease in Tg has also been reported by [125, 126].

The present experimental practices to evaluate environmental degradation of thermoplastics involve long time exposure of the test specimens to varied levels of humidity and temperature conditions. More often, these experimental methods involve tremendous cost and time; the setups are hard to conduct and generally fail to shed enough light on the complex behavior that the material system exhibits in the presence of moisture. It is therefore necessary to develop computational tools that offer accurate prediction and optimization capabilities to further expand the realm of applications of thermoplastic materials. This necessitates a thorough understanding of the complex mechanical behavior of the constituents comprising the microstructure in the presence of coupled physical processes, the resulting internal stress states due to relative differences in the physical and mechanical properties of the constituent phases, the non-uniform degradation of the constituent phase properties and the strong coupling that exists between the evolving microstructure and the macro scale response.

A considerable amount of research efforts including analytical methods, single and multiscale methods have been devoted towards developing such numerical tools. Gerad *et al.* [127, 128] studied the coupling between chemical leaching in underground cementitious structures in the presence of water and the progressive mechanical damage that occurs. Ulm *et al.* [129] developed the homogenization based chemo-mechanics theory to study the effect of chemical leaching on the structural integrity of concrete structures. Oskay and Haney [130] studied the effect of extreme mechanical and environmental loading on titanium structures using a single scale thermo-chemo-mechanical model. Ozdemir *et al.* [131]studied the coupling between thermal and mechanical fields using the multiscale homogenization approach. Terada and Kurumatani [132] developed a two scale diffusion-deformation model to analyze micro crack propagations and aging in quasi brittle solids due to diffusion of scalar fields. Yu and Fish[133] studied the coupling between multiple physical processes in thermo-viscoelastic composites at multiple spatial and temporal scales. Kuznetsov and Fish [134] developed a coupling scheme between electrical and mechanical field in heterogeneous solids.

In this chapter we develop a computationally efficient multiscale-multiphysics framework aimed at predicting mechanical response of thermoplastic composites subjected to different levels of moisture. In Section 5.2 the effects of moisture on the physical and mechanical properties of polyamides is discussed. In Section 5.3, the mathematical model of the coupled mechanical deformation - moisture diffusion process is formulated at the micro-scale based on the observed experimental data. The spatial homogenization (upscaling) procedure is described in Section 5.4. Computational complexity of analyzing the coupled physical processes at multiple scales is reduced via model reduction scheme, originally introduced for the mechanical fields. Section 5.5 enumerates the implementation aspects of the multiscale-multiphysics model. Details of the experimental program are outlined in Section 5.6 and the model is validated in Section 5.7

5.2 Effects of Moisture on the Properties of Polyamides

Polyamides are susceptible to moisture absorption. The absorbed moisture breaks the inter-catenary polymer-polymer hydrogen bonds to form water-polymer bonds. The net effect is plasticization of the matrix leading to mobilization of the structural units. The mobilization of the structural chains causes a decrease in the glass transition temperature. The breaking of the inter-catenary hydrogen bonds also leads to a reversible loss in strength and stiffness, consistent with the decrease in T_g. In the following paragraphs the theory of kinetics of moisture diffusion and the subsequent degradation of the physical and mechanical properties is enumerated. Formulations for the maximum moisture content and the observed decrease in the glass transition temperature, stiffness and strength of short fiber thermoplastics are also presented.

5.2.1 Effect of Moisture on the Glass Transition Temperature of Polyamides

The amorphous regions in hydrophilic polymers like PA-6 and PA-66/6 are known to absorb moisture that leads in mobilization of the polymer structural chains. This increase in mobility of the chains due to increased moisture content causes the glass transition temperature of the polymer to decrease as represented by the peak of the $\tan\,\delta$ curves in Figure 56 and Figure 57 respectively.

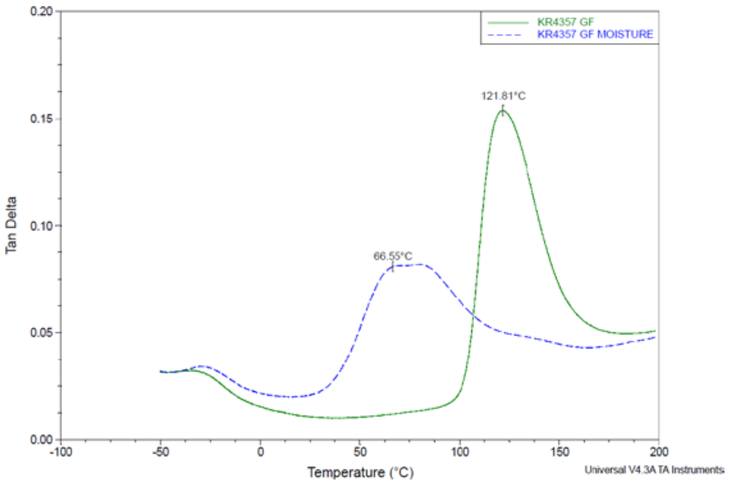

Figure 56: Tg of Ultramid® T KR4357 G6 in dry state and moisture conditioned state [121]

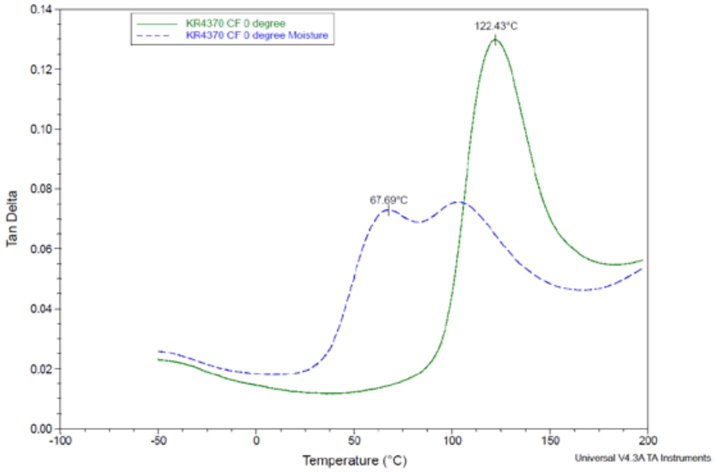

Figure 57: Tg of Ultramid® T KR4370 C6 in dry state and moisture conditioned state [121]

Typically the microstructure of polyamides comprises of two phases namely the crystalline phase and the amorphous phase. The moisture is assumed to diffuse in the amorphous whereas the crystalline regions are considered to be completely inaccessible to moisture. The monotonic decrease in T_g due to an increase in the moisture content c for a typical polyamide is shown in Figure 58. Based on the assumptions made above, Reimschuessel [122] suggests the following relation between moisture content c and the glass transition temperature T_g

$$T_g = \left(\Delta T_g\right)_0 \exp\left\{-\left[\ln\left(\Delta T_g\right)_0\right] c / \tau c_l\right\} + T_{gl} \tag{5.1}$$

where $\left(\Delta T_g\right)_o = T_{go} - T_{gl}$ and $\tau = (c_l - \delta)/c_l$; T_{go} is the glass transition temperature in the dry polymer; c_l corresponds to the maximum amount of moisture absorbed that directly interacts with all of the amide functions available in the amorphous region at which $dT_g / dc \to 0$; T_{gl} is the limiting glass temperature at corresponding moisture content c_l.

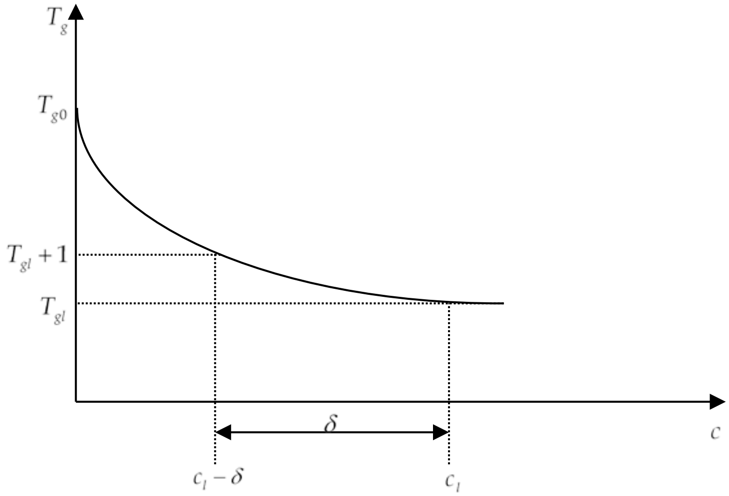

Figure 58: Schematic representation of the $T_g(w)$ relationship [122]

If we consider the glass transition temperature $T_{gl} + 1$ and its conjugate moisture content $c_l - \delta$ as shown in above figure, then the equation for δ can be written as

$$\delta = c_l - c\left\{1 - \left[\ln(T_g - T_{gl})\right] / \left[\ln(T_{g0} - T_{gl})\right]\right\}^{-1} \tag{5.2}$$

In order to evaluate the decrease in the glass transition temperature T_g by utilizing the relation in equation (5.1), we need to develop a formulation for the maximum moisture content c_l.

5.2.2 Formulation for Maximum Moisture Content

In the following paragraphs the formulation for the maximum moisture content in polyamide based material systems is formulated.

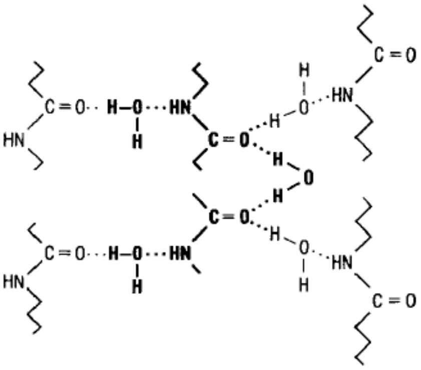

Figure 59: Interaction of amide groups with absorbed moisture in PA-6 [118]

The concentration of accessible amide groups (NHCO) in PA-6 with a crystallinity factor of α is given by

$$\begin{aligned}\left[NHCO\right]_{accessible} &= (1-\alpha)\left[NHCO\right]_{total} \\ \left[NHCO\right]_{total} &= S(P_n - 1) = M_p - S\end{aligned} \tag{5.3}$$

where S is the number of polymer molecules, P_n is the number average degree of polymerization and M_p is the total number of monomer segments. In the event of a high degree of polymerization $P_n \gg 1$; the number of available polymer molecules is very low $S \ll M_p$, following which the total number of amide groups per gram of polymer is given as

$$\left[NHCO\right]_{total} = 8.85e-03 / \text{gm of PA-6} \tag{5.4}$$

Next, we use the physics of the moisture absorption process to arrive at a relation between the accessible amide groups and the maximum moisture content c_l. The mechanism of absorption of water as suggested by Puffr and Sebenda [118] entails successive adsorption of three molecules of water for every two neighboring amide groups and results in an interaction as depicted in Figure 59.

$$c_l = 18*(3/2)*\left[NHCO\right]_{accessible} \tag{5.5}$$

Substituting equation (5.3) (a) in equation (5.5) yields

$$c_l = 0.239(1-\alpha) \tag{5.6}$$

where $\alpha = 0.4$ is the crystallinity factor. Having computed c_l the suppression of the glass transition temperature by moisture ingression may be computed by equation (5.10).

5.2.3 Effect of Moisture on Strength and Stiffness of Polyamides

Another effect of the mobilization of the polymer chains consistent with decrease in the glass transition temperature is the irreversible mechanism that leads to loss of elastic modulus and strength. The decrease in elastic modulus and strength of PA-6 due to moisture ingression is depicted in Figure 60(a) and (b) respectively.

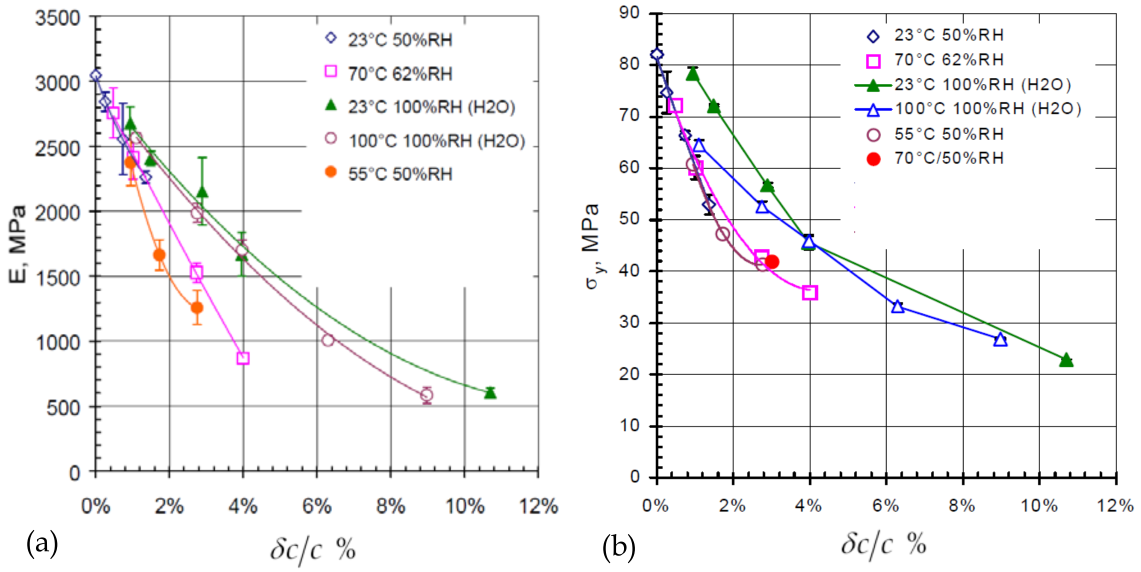

Figure 60: Plot depicting decrease in modulus and strength of nylon-6 due to moisture ingression [121]

The relationship between elastic modulus and moisture content given by Reimschuessel [122] is

$$E = \left(E' - E_l\right)\exp\left\{-\left[\ln\left(E' - E_l\right)\right]c/\varepsilon c_l\right\} + E_l \tag{5.7}$$

where E' is the modulus at $c = 0$, E_l is the modulus at $c = c_l$ and ε is a material parameter.

The relationship in above equation is completely analogous to the relation between T_g and the moisture content given in equation (5.1).

In the present work the relationship between the strength and moisture content is approximated by the following relation which is analogous to equation (5.7)

$$S = \left(S' - S_l\right)\exp\left\{-\left[\ln\left(S' - S_l\right)\right]c/\phi c_l\right\} + S_l \tag{5.8}$$

where S' is the modulus at $c = 0$, S_l is the modulus at $c = c_l$ and ϕ is a material parameter..

5.3 Coupled Multiphysics Model

Consider a heterogeneous nonlinear solid media on a composite domain Ω^{ζ} with boundary $\partial\Omega^{\zeta}$ as shown in Figure 61. The superscript ζ implies the dependence of coarse scale response on the fine scale fields. The microstructure of a composite material is assumed to be statistically homogeneous with local periodicity. The unit cell domain is denoted by Θ. For simplicity, small deformations are considered.

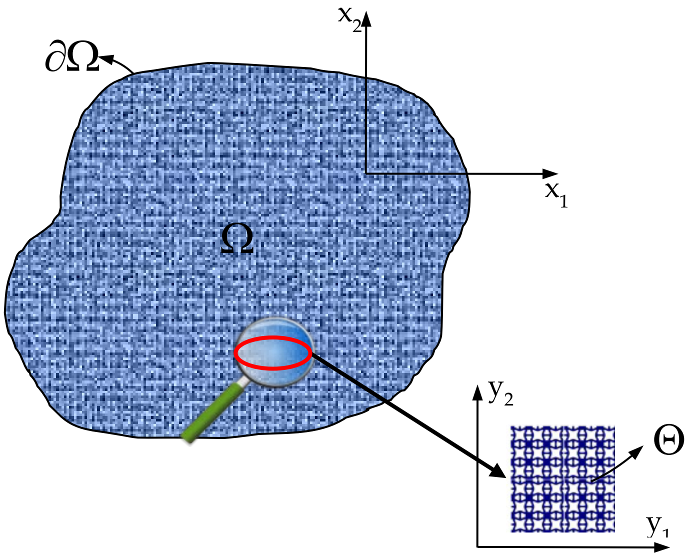

Figure 61: Illustration of the coarse and fine scale fields

Consider the strong form of the governing equations of the coupled mechanical-diffusion problem on the composite domain Ω^{ζ}

$$
\begin{aligned}
&\sigma_{ij,j}^{\zeta} + b_i^{\zeta} = 0 && \text{on } \Omega^{\zeta} \\
&\sigma_{ij}^{\zeta} = L_{ijkl}^{\prime\zeta}\left[\varepsilon_{kl}^{\zeta} - \mu_{kl}^{I\zeta}\right] && \text{on } \Omega^{\zeta} \\
&\varepsilon_{ij}^{\zeta} = u_{(i,j)}^{\zeta} \equiv \frac{1}{2}\left(u_{i,j}^{\zeta} + u_{j,i}^{\zeta}\right) && \text{on } \Omega^{\zeta} \\
&J_{i,i}^{\zeta} + \dot{c}^{\zeta} = 0 && \text{on } \Omega^{\zeta} \\
&J_i^{\zeta} = -D_{ik}^{\prime\zeta}\left(c_{,k}^{\zeta} - \eta_k^{\zeta}\right) && \text{on } \Omega^{\zeta}
\end{aligned}
\tag{5.9}
$$

subject to the following initial and boundary conditions

$$
\begin{aligned}
&u_i^{\zeta}(x,t) = \hat{u}_i^{\zeta}(x,t) \quad x \in \Omega^{\zeta}; t = 0 \\
&u_i^{\zeta}(x,t) = \overline{u}_i(x,t) \quad x \in \partial\Omega^{u}; t > 0 \\
&\sigma_{ij}^{\zeta}(x,t) n_j(x) = \overline{t}_i\ (x,t) \quad x \in \partial\Omega^{t}; t > 0 \\
&c^{\zeta}(x,t) = c_0(x,t);\ x \in \Omega^{\zeta}\ ;\ t = 0 \\
&c^{\zeta}(x,t) = \overline{c}\ (x,t);\ x \in \partial\Omega^{c}\ ;\ t > 0 \\
&J_n^{\zeta}(x,t) = \overline{J}_n(x,t) \quad x \in \partial\Omega^{J};\ t > 0
\end{aligned}
\tag{5.10}
$$

where the two primary variables are the displacements u_i^{ζ} and moisture concentration c^{ζ} ; μ_{kl}^{ζ} is an eigenstrain arising from inelastic deformation, thermal and moisture effects; η_k^{ζ} is the eigenconcentration gradient; J_i^{ζ} and σ_{ij}^{ζ} are moisture flux and stress, respectively; $D_{ij}^{\prime\zeta}$ and $L_{ijkl}^{\prime\zeta}$ denote the initial (in dry conditions) Fick's and Hooke's law, respectively. In the following we assume that the boundary $\partial\Omega$ is smooth with $n_j(x)$ being the normal to the boundary; $\overline{c}^{\zeta}$ and $\overline{u}_i$ are the prescribed concentration and displacement defined on $\partial\Omega^{c}$ and $\partial\Omega^{u}$, respectively; $\overline{J}_n$ and $\overline{t}_i$ are the prescribed flux and traction defined on $\partial\Omega^{J}$ and $\partial\Omega^{t}$, respectively, such that $\partial\Omega^{c} \cup \partial\Omega^{J} = \partial\Omega, \quad \partial\Omega^{c} \cap \partial\Omega^{J} = 0$ and $\partial\Omega^{u} \cup \partial\Omega^{t} = \partial\Omega, \quad \partial\Omega^{u} \cap \partial\Omega^{t} = 0$. The superimposed dot and comma followed by a subscript denote temporal and spatial derivatives, respectively.

The moisture diffusion and mechanical deformation are two-way coupled. Diffusivity is enhanced by hydrostatic strain. The mechanical problem is affected by moisture content in three ways:

(i) The Young modulus of a polymer reduces with higher moisture content as shown in Figure 60(a)

(ii) The strength of the polymer reduces as well with increase in moisture content as can be seen in Figure 60 (b)

(iii) The presence of moisture also induces swelling

The relationship between elastic modulus and moisture content proposed by Reimschuessel [122] in the context of multiple length scales is restated as

$$E^{\zeta} = \left(E'^{\zeta} - E_l\right)\exp\left\{-\left[\ln\left(E'^{\zeta} - E_l\right)\right]c^{\zeta} / \varepsilon c_l\right\} + E_l \tag{5.11}$$

where E'^{ζ} is the Young's modulus at $c^{\zeta} = 0$, E_l is the modulus at $c^{\zeta} = c_l$ and $\varepsilon = 0.15$ is a material parameter that has been calibrated based on Figure 60(a).

The relationship between the polymer strength and moisture content is approximated similarly to the relation in (5.11) as

$$S^{\zeta} = \left(S'^{\zeta} - S_l\right)\exp\left\{-\left[\ln\left(S'^{\zeta} - S_l\right)\right]c^{\zeta} / \varepsilon c_l\right\} + S_l \tag{5.12}$$

The two way coupled multiphysics model is defined as

$$
\begin{aligned}
&\sigma_{ij}^{\zeta} = L_{ijkl}'^{\zeta}\left(\varepsilon_{kl}^{\zeta} - \mu_{kl}^{\zeta}\left(c^{\zeta}\right)\right)\\
&\mu_{kl}^{\zeta}\left(c^{\zeta}\right) = \mu_{kl}^{in}\left(S^{\zeta}\left(c^{\zeta}\right)\right) + \mu_{kl}^{el}\left(E^{\zeta}\left(c^{\zeta}\right)\right) + \mu_{kl}^{s}\left(c^{\zeta}\right)\\
&\mu_{kl}^{el}\left(E^{\zeta}\left(c^{\zeta}\right)\right) = \left(I_{klij} - \left(L_{klmn}'^{\zeta}\right)^{-1} L_{mnij}^{\zeta}\left(E^{\zeta}\left(c^{\zeta}\right)\right)\right)\varepsilon_{ij}^{\zeta}\\
&\mu_{ij}^{s}\left(c^{\zeta}\right) = \delta_{ij}\beta c^{\zeta}\\
&\eta_{k}^{\zeta} = \left(1 - \gamma\left(\varepsilon_{kk}^{\zeta}\right)\exp\left(\alpha c^{\zeta}\right)\right)c_{,k}^{\zeta}
\end{aligned}
\tag{5.13}
$$

where $\mu_{kl}^{in}\left(S^{\zeta}\left(c^{\zeta}\right)\right)$ is an eigenstrain arising from mechanical loading with diffusion-dependent strength, $\mu_{kl}^{el}\left(E^{\zeta}\left(c^{\zeta}\right)\right)$ is an eigenstrain arising due to moisture dependent Young's modulus; $\mu_{kl}^{s}\left(c^{\zeta}\right)$ is a hygroscopic strain induced by material swelling; $L_{mnij}^{\zeta}\left(E^{\zeta}\left(c^{\zeta}\right)\right)$ denotes moisture-dependent Hooke's law; η_{k}^{ζ} is the eigen-concentration gradient of the non-Fickian deformation-dependent diffusion model; α and β are model parameters; $\gamma\left(\varepsilon_{kk}^{\zeta}\right)$ encapsulates the deformation-dependent diffusion, such that $\gamma\left(\varepsilon_{kk}^{\zeta} = 0\right) = 1$ and $\gamma\left(\varepsilon_{kk}^{\zeta} \to \infty\right) \to \infty$.

Remark 1: In case of constant moisture conditions, the eigenstrain arising due to moisture dependent Young's modulus $\mu_{kl}^{el}\left(E^{\zeta}\left(c^{\zeta}\right)\right)$ can be removed. Instead $L_{ijkl}'^{\zeta}$ would represent Hooke's law at the predefined moisture conditions.

Remark 2: It is a trivial exercise to show that the constitutive equation of the moisture diffusion can be expressed as

$$
\begin{aligned}
&J_{i}^{\zeta} = D_{ij}'^{\zeta} c_{,j}^{\zeta}\\
&D_{ij}^{\zeta} = D_{ij}'^{\zeta}\ \gamma\left(\varepsilon_{kk}^{\zeta}\right)\ \alpha\ \exp\left(\beta c^{\zeta}\right)
\end{aligned}
\tag{5.14}
$$

where D_{ij}^{ζ} is nonlinear diffusivity.

5.4 Unified Multiscale-Multiphysics Homogenization

In the present manuscript the size of a periodic unit cell domain Θ is assumed to be infinitesimally small compared to the characteristic length of the coarse-scale domain Ω. This formalism can be described by the asymptotic homogenization theory. Let x be the coarse-scale position vector in the coarse scale domain Ω and $y_i = x_i / \zeta$ be the fine-scale position vector in unit cell domain Θ where $0 < \zeta \ll 1$. All physical quantities are assumed to have two explicit dependencies: one on the coarse-scale coordinate x and the second one, on the fine-scale coordinate y. Using the classical formalism any periodic function can be represented as $f^{\zeta}(x) \equiv f(x, y(x)) \equiv f(x, y(x) + k\hat{y})$.

The indirect spatial derivatives of the response function $f^{\zeta}(x)$ can be calculated by the chain rule as

$$f^{\zeta}{}_{,i} = \underbrace{\frac{\partial f(x,y)}{\partial x_i}}_{f_{,x_i}} + \frac{1}{\zeta}\underbrace{\frac{\partial f(x,y)}{\partial y_i}}_{f_{,y_i}} \tag{5.15}$$

The displacement field $u_i^{\zeta} = u_i\left(x,y,t\right)$ and moisture concentration $c^{\zeta} = c\left(x,y,t\right)$ are approximated in terms of double-scale asymptotic expansions on $\Omega \times \Theta$ as

$$c^{\zeta} = c^{c}(x,t) + \zeta c^{1}(x,y,t) + O(\zeta^{2}) \tag{5.16}$$

$$u_i^{\zeta} = u_i^{c}(x,t) + \zeta u_i^{1}(x,y,t) + O(\zeta^{2}) \tag{5.17}$$

where the leading order terms $c^{c}(x,t)$ and $u_i^{c}(x,t)$ represent the coarse-scale field. The asymptotic expansions for the strain and concentration gradient are obtained by taking spatial derivatives of the displacement field $u_i^{\zeta} = u_i\left(x,y,t\right)$ and moisture concentration $c^{\zeta} = c\left(x,y,t\right)$

$$\varepsilon_{ij}^{\zeta}(x,y,t) = \underbrace{\varepsilon_{ij}^{c}(x,t) + u_{(i,y_j)}^{(1)}(x,y,t)}_{\varepsilon_{ij}^{f}(x,y,t)} + O\left(\zeta\right) \tag{5.18}$$

$$c^{\zeta}_{,i}(x,y,t) = \underbrace{c^{c}_{,x_i}(x,t) + c^{(1)}_{,y_i}(x,y,t)}_{c^{f}_{,x_i}(x,y,t,\tau)} + O(\zeta\ ) \tag{5.19}$$

The asymptotic equations for stress and concentration flux are given as

$$\sigma^{\zeta}_{ij}(x,y,t,\tau) = \underbrace{\sigma^{(0)}_{ij}(x,y,t)}_{\sigma^{f}_{ij}(x,y,t)} + O\left(\zeta\ \right) \tag{5.20}$$

$$J^{\zeta}_{i}(x,y,t,\tau) = \underbrace{J^{(0)}_{i}(x,y,t)}_{J^{f}_{i}(x,y,t)} + O(\zeta\ ) \tag{5.21}$$

where the superscript *f* denotes fine scale fields. The fine-scale stresses and fluxes are related to the fine scale strains ε^{f}_{ij} and concentration gradients $c^{f}_{,i}$ by utilizing constitutive equations in (5.9)(b) and (e) and (5.13)

By substituting the asymptotic expansions in equation (5.16) to (5.21) into the strong form in (5.9) and enforcing the chain rule (5.15), yields the governing equations at the coarse scale and fine scale.

$$\text{Fine-scale}: \begin{cases} J^{f}_{i,y_j} = 0 \\ \sigma^{f}_{ij,y_j} = 0 \\ \varepsilon^{f}_{kl} = \varepsilon^{c}_{kl} + u^{(1)}_{(k,y_l)} \\ c^{f}_{,i} = c^{c}_{,x_i} + c^{(1)}_{,y_i} \\ J^{f}_{i} = -D'_{ik}\left(c^{f}_{,k} - \eta^{f}_{k}\right) \\ \sigma^{f}_{ij} = L_{ijkl}\left(\varepsilon^{f}_{kl} - \mu^{f}_{kl}\right) \\ \mu^{f}_{kl} = \mu^{\zeta}_{kl}\left(c^{\zeta}\right) = \mu^{in}_{kl}\left(S^{\zeta}\left(c^{f}\right)\right) + \mu^{el}_{kl}\left(E^{\zeta}\left(c^{f}\right)\right) + \mu^{s}_{kl}\left(c^{f}\right) \\ \mu^{el}_{kl}\left(E^{\zeta}\left(c^{f}\right)\right) = \left(I_{klij} - \left(L'^{\zeta}_{klmn}\right)^{-1} L^{\zeta}_{mnij}\left(E^{\zeta}\left(c^{f}\right)\right)\right)\varepsilon^{f}_{ij} \\ \mu^{s}_{ij} = \delta_{ij}\beta c^{f} \\ \eta^{f}_{k} = \left(1 - \gamma\left(\varepsilon^{f}_{jj}\right)\exp\left(\alpha c^{f}\right)\right)c^{f}_{,k} \\ u^{(1)}_{i}(x,y), c^{(1)}(x,y) \quad y - periodic \end{cases} \tag{5.22}$$

The coarse-scale fields are defined as an average of the leading order (or fine-scale) fields computed over the unit cell domain as

$$\text{Coarse-scale}: \begin{cases} J^c_{i,x_i} = \dot{c}^c \\ \sigma^c_{ij,x_j} + b^c_i = \rho^c \ddot{u}^c_i \\ \sigma^c_{ij} = \dfrac{1}{|\Theta|}\displaystyle\int_\Theta \sigma^f_{ij}\, d\Theta \\ J^c_i = \dfrac{1}{|\Theta|}\displaystyle\int_\Theta J^f_i\, d\Theta \\ u^c_i(x,t) = \overline{u}^c_i(x,t) & x \in \partial\Omega^u, t > 0 \\ c^c(x,t) = \overline{c}^c(x,t) & x \in \partial\Omega^c, t > 0 \\ u^c_i(x,t) = \hat{u}_i(x,t) & x \in \Omega, t = 0 \\ c^c(x,t) = c_0(x,t) & x \in \Omega\ ;\ t = 0 \\ \sigma^c_{ij}(x,t)n_j = \overline{t}^c_i(x,t) & x \in \partial\Omega^t, t > 0 \\ J^c_n(x,t) = \overline{J}^c_n(x,t) & x \in \partial\Omega^J, t > 0 \end{cases} \tag{5.23}$$

5.4.1 Residual-Free Fields and Model Reduction

To reduce the computational cost associated with multiple solutions of the unit cell problem in (5.22), a model reduction scheme originally developed for a single physical process [33, 35, 50-52] is employed. The model reduction technique is based on the construction of residual free scalar and vector fields. The fine scale perturbation of the displacement field $u^{(1)}_i$ is constructed to satisfy the unit cell equilibrium equations for arbitrary coarse scale strains and fine scale eigenfields

$$u^{(1)}_i(x,y,t) = H^{kl}_i(y)\varepsilon^c_{kl}(x,t) + \int_\Theta \tilde{h}^{kl}_i(y,\tilde{y})\, \mu^f_{kl}(x,\tilde{y},t)d\tilde{\Theta} + \int_S \breve{h}^{\breve{n}}_i(y,\breve{y})\, \delta^f_{\breve{n}}(x,\breve{y},t)d\breve{S} \tag{5.24}$$

H^{kl}_i, $\tilde{h}^{kl}_i$, and $\breve{h}^{\breve{n}}_i$ are the influence functions for coarse-scale strain, fine-scale eigenstrain, and fine-scale eigenseparation, respectively.

Likewise the fine scale moisture concentration $c^{(1)}$ is constructed to satisfy the fine scale diffusion equations arbitrary coarse-scale concentration gradients and fine-scale eigenfields as follows

$$c^{(1)}(x,y) = H^{i}(y)\ c^{c}_{,i}(x,t) + \int_{\Theta} h^{i}(y,\tilde{y})\ \eta^{f}_{i}(x,\tilde{y},t)d\Theta \tag{5.25}$$

$H^{i}(y)$ is the coarse scale concentration gradient influence function and $h^{i}(y,\tilde{y})$ is the fine scale eigen concentration gradient influence function. Substituting (5.24) and (5.25) in (5.22) yields

$$\left(L_{ijkl}(y) \begin{pmatrix} \left(I_{klmn} + H^{mn}_{(k,y_l)}\right)\varepsilon^{c}_{mn}(x,t) + \left(\int_{\Theta} \tilde{h}^{mn}_{(k,y_l)}(y,\tilde{y})\ \mu^{f}_{mn}(x,\tilde{y},t)d\tilde{\Theta} - \mu^{f}_{kl}(x,y,t)\right) \\ +\int_{S} \breve{h}^{\breve{n}}_{(k,y_l)}(y,\hat{y})\ \delta^{f}_{\breve{n}}(x,\breve{y})d\breve{S} \end{pmatrix} \right)_{,y_j} = 0 \tag{5.26}$$

$$\left(-D'_{ij}\ (y)\left(\left(I_{jk} + H^{k}_{,y_j}(y)\right)c^{c}_{,k}(x,t) + \left(\int_{\Theta} h^{k}_{,y_j}(y,\tilde{y})\ \eta^{f}_{k}(x,\tilde{y},t)d\Theta - \eta^{f}_{j}(x,y,t) \right)\right)\right)_{,y_j} = 0 \tag{5.27}$$

The eigenstrains, eigen-separations and eigen-concentration gradients are discretized in terms of phase eigenstrains $\mu^{(\alpha)}_{kl}$, phase eigenseparation $\delta^{(\alpha)}_{\breve{n}}$ and phase eigenconcentration gradients $\eta^{(\alpha)}_{k}$ over phase domain $\Theta^{(\alpha)}$

$$\begin{aligned} \mu^{f}_{ij}(x,y,t) &= \sum_{\alpha=1}^{n} \tilde{N}^{(\alpha)}(y)\mu^{(\alpha)}_{kl}(x,t); \\ \delta^{f}_{\breve{n}}(x,y,t) &= \sum_{\xi=1}^{m} \breve{N}^{(\xi)}(y)\delta^{(\xi)}_{\breve{n}}(x,t) \end{aligned} \tag{5.28}$$

$$\eta^{f}_{k}(x,y,t) = \sum_{\alpha=1}^{n} \tilde{N}^{(\alpha)}(y)\eta^{(\alpha)}_{i}(x,t) \tag{5.29}$$

The shape functions $\tilde{N}^{(\alpha)}(y)$ for eigenstrain and eigen-concentration gradient are chosen to be $C^{-1}(\Theta)$ as the eigenfields need to satisfy the condition of continuity. The eigenseparation shape functions are chosen to be $C^0(S)$ functions as the cracks (displacement jumps) need to be continuous across the interfaces. Additionally the shape functions need to satisfy the partition of unity condition.

The average eigenstrains, eigen-separations and eigen-concentration gradients are defined as

$$\begin{aligned} \mu_{ij}^{(\alpha)} &= \int_{\Theta} \tilde{\varphi}^{(\alpha)} \mu_{ij}^{f} \, d\Theta \\ \delta_{\breve{n}}^{(\xi)} &= \int_{S} \breve{\varphi}^{(\zeta)} \delta_{\overset{\frown}{n}}^{f} \, dS \\ \eta_i^{(\alpha)} &= \int\limits_{\Theta} \tilde{\varphi}^{(\alpha)} \eta_i^{f} \, d\Theta \end{aligned} \tag{5.30}$$

The weight functions $\tilde{\varphi}^{(\alpha)}$ and $\breve{\varphi}^{(\zeta)}$ should satisfy the condition of positivity and normalization. A piecewise constant approximation for the eigenstrain and eigen-separation shape functions and weight functions yields

$$\begin{aligned} &\tilde{N}^{(\alpha)}(y) = \begin{cases} 1 & y \in \Theta^{(\alpha)} \\ 0 & y \in \Theta^{(\alpha)} \end{cases}, \quad \tilde{\varphi}^{(\alpha)}(y) = \tilde{N}^{(\alpha)}(y) / \left|\Theta^{(\alpha)}\right| \\ &\breve{N}^{(\xi)}(y) = \begin{cases} \sum\limits_{A \in S^{(\xi)}} N_A^f(y) & y \in S^{(\xi)} \\ 0 & y \notin S^{(\xi)} \end{cases}, \quad \breve{\varphi}^{(\zeta)}(y) = \begin{cases} 1 / \left|S^{(\zeta)}\right| & \mathit{if} \quad y \in S^{(\beta)} \\ 0 & \mathit{elsewhere} \end{cases} \end{aligned} \tag{5.31}$$

Substituting the discretization in (5.28) to (5.31) into (5.26) and (5.27), and requiring the unit cell equilibrium to be satisfied for arbitrary ε_{kl}^{c}, $\mu_{kl}^{(\alpha)}$, $\delta_{\breve{n}}^{(\xi)}$, $c_{,k}^{c}$ and $\eta_k^{(\alpha)}$ yields the following strong form of the influence functions.

$$\begin{aligned}
&\left\{L_{ijkl}\left(y\right)\left[I_{klmn}+H_{\left(k,y_l\right)}^{mn}\left(y\right)\right]\right\}_{,y_j}=0\\
&\left\{L_{ijkl}\left(y\right)\left[P_{kl}^{mn(\alpha)}\left(y\right)-I_{klmn}^{(\alpha)}\left(y\right)\right]\right\}_{,y_j}=0\\
&\left\{L_{ijkl}\left(y\right)Q_{kl}^{\breve{n}(\xi)}\left(y\right)\right\}_{,y_j}=0 \;\; with \;\; \delta_{\breve{n}}^{f}\left(\hat{y}\right)=\breve{N}^{(\xi)}\left(\hat{y}\right)\\
&\left\{D'_{ij}\left(y\right)\left[\delta_{jk}+H_{,y_j}^{k}\left(y\right)\right]\right\}_{,y_i}=0\\
&\left\{D'_{ij}\left(y\right)\left[P_{j}^{k(\alpha)}(y)-I_{jk}^{(\alpha)}(y)\right]\right\}_{,y_i}=0
\end{aligned} \tag{5.32}$$

subjected to periodicity conditions

where

$$\begin{aligned}
&P_{ij}^{mn(\alpha)}\left(y\right)=\int_{\Theta^{(\alpha)}}\tilde{h}_{\left(i,y_j\right)}^{mn}\left(y,\tilde{y}\right)d\tilde{\Theta}\\
&Q_{ij}^{\breve{n}(\xi)}\left(y\right)=\int_{S}\breve{h}_{\left(i,y_j\right)}^{\breve{n}}\left(y,\hat{y}\right)\breve{N}^{(\xi)}\left(\breve{y}\right)d\breve{S}\\
&P_{j}^{k(\alpha)}(y)=\int\limits_{\Theta}h_{,y_j}^{k}\left(y,\hat{y}\right)\tilde{N}(y)d\Theta
\end{aligned} \tag{5.33}$$

The strong form of the influence function problems (5.32) can be solved by the Galerkin approximation based finite element method.

5.4.2 Reduced Order System of Equations

The residual-free strain field at the fine scale is obtained by substituting equations (5.28) and (5.24) into equation (5.22)(c)

$$\varepsilon_{ij}^{f}(x,y,t)=E_{ij}^{kl}\left(y\right)\varepsilon_{kl}^{c}(x,t)+\sum_{\alpha=1}^{n}P_{ij}^{kl(\alpha)}\left(y\right)\mu_{kl}^{(\alpha)}(x,t)+\sum_{\xi=1}^{m}Q_{ij}^{\breve{n}(\xi)}\left(y\right)\;\delta_{\breve{n}}^{(\xi)}(x,t) \tag{5.34}$$

where $E_{ij}^{kl}\left(y\right)=I_{ijkl}+H_{\left(i,y_j\right)}^{kl}\left(y\right)$

Averaging the residual-free strain field over partition domain $\Theta^{(\beta)}$ yields

$$\varepsilon_{ij}^{(\beta)}(x,t)-\sum_{\alpha=1}^{n}P_{ij}^{kl(\beta\alpha)}\;\mu_{kl}^{(\alpha)}(x,t)-\sum_{\xi=1}^{m}Q_{ij}^{\breve{n}(\beta\xi)}\;\delta_{\breve{n}}^{(\xi)}(x,t)=E_{ij}^{kl(\beta)}\varepsilon_{kl}^{c}(x,t) \tag{5.35}$$

where $*^{(\beta)} \equiv \frac{1}{\left|\Theta^{(\beta)}\right|}\int_{\Theta^{(\beta)}} *d\Theta$

Likewise the reduced order residual free fine-scale traction $t_{\breve{n}}^{(\eta)}$ along the interface is obtained by averaging $\sigma_{ij}^{f}\breve{n}_j$ over the interface partition, which yields

$$-\sum_{\alpha=1}^{n} C_{\breve{n}}^{kl(\eta\alpha)}\mu_{kl}^{(\alpha)}(x,t) + t_{\breve{n}}^{(\eta)}(x,t) - \sum_{\xi=1}^{m} D_{\breve{n}}^{\breve{m}(\eta\xi)}\delta_{\breve{m}}^{(\xi)}(x,t) = T_{\breve{n}}^{kl(\eta)}\varepsilon_{kl}^{c}(x,t) \tag{5.36}$$

where

$$\begin{aligned} C_{\hat{m}}^{kl(\alpha)} &= a_{\hat{m}i}L_{ijpq}\left(y\right)\left[P_{pq}^{kl(\alpha)}\left(y\right) - I_{pqkl}^{(\alpha)}\right]\hat{n}_j\left(y\right) \\ D_{\hat{m}\hat{n}}^{(\xi)} &= a_{\hat{m}i}L_{ijpq}\left(y\right)Q_{pq}^{\breve{n}(\xi)}\left(y\right)\breve{n}_j\left(y\right) \\ T_{\hat{m}}^{kl} &= a_{\hat{m}i}L_{ijpq}\left(y\right)E_{pq}^{kl}\left(y\right)\breve{n}_j\left(y\right) \\ *^{(\eta)} &\equiv \frac{1}{\left|S^{(\eta)}\right|}\int_{S^{(\eta)}} *dS \end{aligned} \tag{5.37}$$

The fine scale residual free concentration gradient field is obtained by substituting equations (5.29) and (5.25) into equation (5.22)(d)

$$c_{,i}^{f}(x,y,t) = E_i^j(y)c_{,j}^{c}(x,t) + \sum_{\alpha=1}^{n} P_i^{j(\alpha)}(y)\eta_j^{(\alpha)}(x,t) \tag{5.38}$$

where $E_i^j(y) = \delta_{ij} + H_{,y_i}^{j}(y)$

Averaging the residual-free strain field over partition domain $\Theta^{(\beta)}$ yields

$$c_{,i}^{\beta}(x,t) = E_i^{j(\beta)}c_{,j}^{c}(x,t) + \sum_{\alpha=1}^{n} P_i^{j(\beta,\alpha)}\eta_j^{(\alpha)}(x,t) \tag{5.39}$$

where $*^{(\beta)} \equiv \frac{1}{\left|\Theta^{(\beta)}\right|}\int_{\Theta^{(\beta)}} *d\Theta$

The reduced order coarse scale stress and flux fields are obtained by averaging the fine scale field over the unit cell domain

$$\begin{aligned}
&\sigma^{c}_{ij}(x,t) = L^{c}_{ijkl}\varepsilon^{c}_{kl}(x,t) + \sum_{\alpha=1}^{n} A^{c(\alpha)}_{ijkl}\ \mu^{(\alpha)}_{kl}(x,t) + \sum_{\xi=1}^{m} B^{c(\xi)}_{ij\breve{n}}\ \delta^{(\xi)}_{\breve{n}}(x,t) \\
&J^{c}_{i}(x,t) = -D^{c}_{ij}c^{c}_{,j}(x,t) - \sum_{\alpha=1}^{n} A^{c(\alpha)}_{ik}\eta^{(\alpha)}_{k}(x,t)
\end{aligned} \tag{5.40}$$

where

$$\begin{aligned}
L^{c}_{ijkl} &= \frac{1}{|\Theta|}\int_{\Theta} L_{ijmn}(y)E^{kl}_{mn}(y)\, d\Theta \\
A^{c(\alpha)}_{ijkl} &= \frac{1}{|\Theta|}\int_{\Theta} L_{ijmn}(y)\left[P^{kl(\alpha)}_{mn}(y) - I^{(\alpha)}_{mnkl}\right] d\Theta \\
B^{c(\xi)}_{ij\breve{n}} &= \frac{1}{|\Theta|}\int_{\Theta} L_{ijmn}(y)Q^{\breve{n}(\xi)}_{mn}(y)\, d\Theta \\
D^{c}_{ij} &= \frac{1}{|\Theta|}\int_{\Theta} D'_{ik}(y)E^{j}_{k}(y)\, d\Theta \\
A^{c(\alpha)}_{ij} &= \frac{1}{|\Theta|}\int_{\Theta} D'_{ik}(y,t)S^{j(\alpha)}_{k}(y)\, d\Theta
\end{aligned} \tag{5.41}$$

The influence function problems in equations (5.32) and the coefficient tensors appearing in equations (5.35), (5.37),(5.39) and (5.41) are pre-computed in the preprocessing phase. At each iteration of the coarse scale nonlinear problem, the phase strains (5.35), concentration gradients (5.39) and the eigen-fields are updated. Finally, the coarse scale stress and flux are updated using equation (5.40).

5.5 Implementation of the Multiscale-Multiphysics Homogenization Model

In this section the aspects of the multiscale-multiphysics software architecture are discussed. The code structure consists of the following two phases.

Preprocessing Phase

- Generate the short fiber unit cell using the modified RSA algorithm
- Solve the scalar (diffusion) and vector (deformation) field influence function problems and compute the coefficient tensors

Coupled Macro Analysis Phase

- Solve the scalar and vector field reduced order system of equations and update fine scale fields

  Update the coarse scale stress and coarse scale flux

The preprocessing phase was implemented in MDS [135]. Abaqus was used as the solver at the coarse scale. The functionality of Abaqus to analyze coupled heat transfer-displacement problems was utilized to conduct the coupled moisture diffusion-deformation analysis. The scalar field formulation was implemented in UMATHT and the vector field formulation was implemented in UMAT. The respective coarse scale quantities of interest are passed by ABAQUS into the UMATHT and UMAT user subroutines at every gauss and every load increment. The reduced order systems of equations for the scalar and vector fields are solved to update the fine scale eigen-fields. The coarse scale stress and flux are computed and passed back to Abaqus to equilibrate the system of equations at the coarse scale. The implementation of the unified multiscale-multiphysics formulation is illustrated in Figure 62 below.

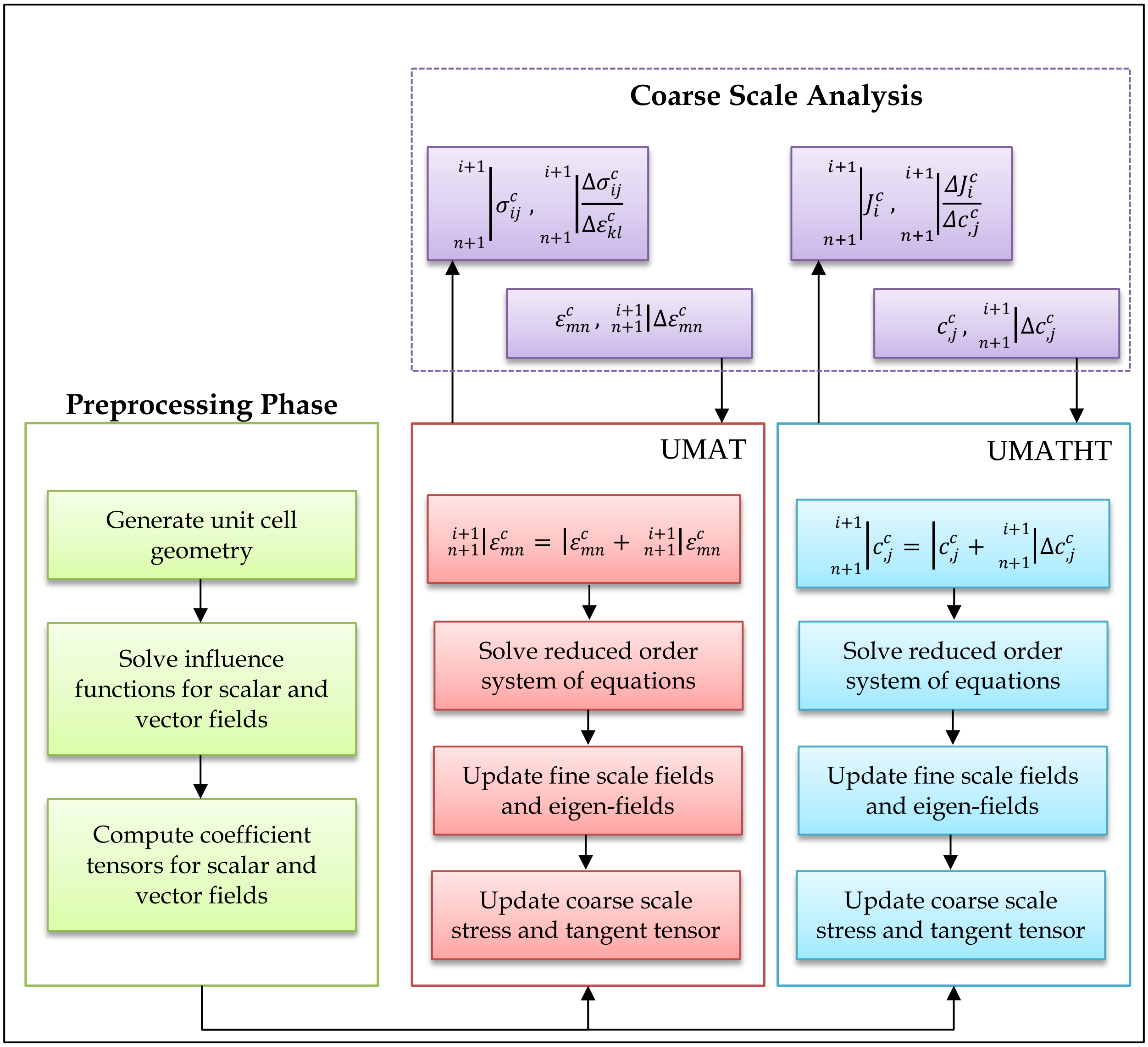
Coarse Scale Analysis
$^{i+1}_{n+1}|\sigma^c_{ij}$, $^{i+1}_{n+1}|\frac{\Delta\sigma^c_{ij}}{\Delta\varepsilon^c_{kl}}$
$^{i+1}_{n+1}|J^c_i$, $^{i+1}_{n+1}|\frac{\Delta J^c_i}{\Delta c^c_{,j}}$
ε^c_{mn} , $^{i+1}_{n+1}|\Delta\varepsilon^c_{mn}$
$c^c_{,j}$, $^{i+1}_{n+1}|\Delta c^c_{,j}$
Preprocessing Phase
Generate unit cell geometry
Solve influence functions for scalar and vector fields
Compute coefficient tensors for scalar and vector fields
UMAT
$^{i+1}_{n+1}|\varepsilon^c_{mn} = |\varepsilon^c_{mn} + {}^{i+1}_{n+1}|\varepsilon^c_{mn}$
Solve reduced order system of equations
Update fine scale fields and eigen-fields
Update coarse scale stress and tangent tensor
UMATHT
$^{i+1}_{n+1}|c^c_{,j} = |c^c_{,j} + {}^{i+1}_{n+1}|\Delta c^c_{,j}$
Solve reduced order system of equations
Update fine scale fields and eigen-fields
Update coarse scale stress and tangent tensor

Figure 62: Schematic of the unified multiscale-multiphysics formulation

5.6 Experimental Program

This section presents a brief overview of the experimental program at General Motors. The experiments involved two material systems namely 30% by weight filled short glass fiber thermoplastics (BASF, Ultramid® T KR4357 G6) and 30% by weight filled short carbon fiber thermoplastics (BASF, Ultramid® T KR4357 C6). The experimental program involved exposing samples of fiber reinforced polyamide materials to varying humidity and temperature conditions. Multiple humidifying conditions were evaluated in order to determine the dependence of the water absorption on temperature and humidity levels. The volumetric expansion of the samples and the gravimetric uptake of water were measured. Once samples reached the equilibrium state under given conditions, the mechanical properties of the material systems were measured and compared with mechanical properties in the Dry As Molded (DAM) state to evaluate the degradation of material properties. The mechanical testing involved uniaxial tensile tests and three point bending tests. The details of the experimental program are presented in Figure 63.

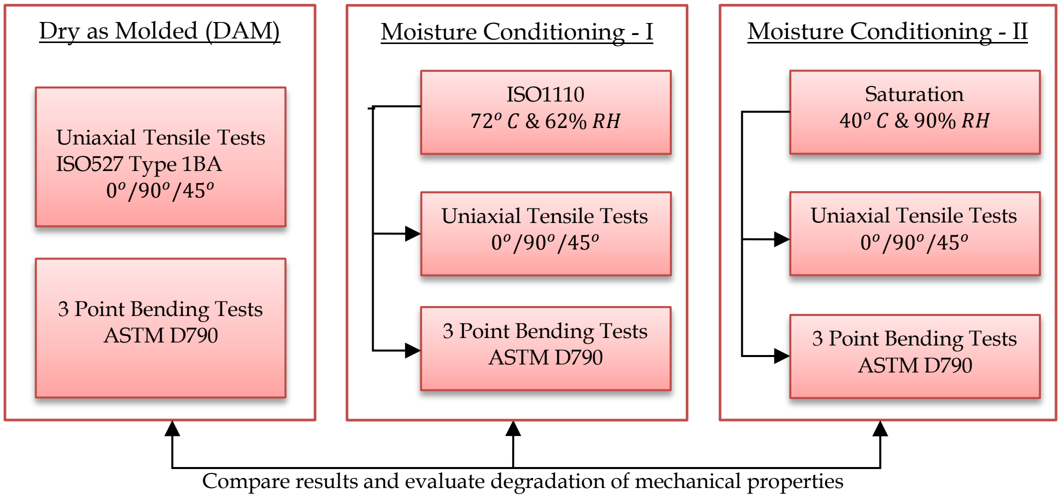
Dry as Molded (DAM)
Uniaxial Tensile Tests ISO527 Type 1BA $0^o/90^o/45^o$
3 Point Bending Tests ASTM D790
Moisture Conditioning - I
ISO1110 $72^o\ C$ & $62\%\ RH$
Uniaxial Tensile Tests $0^o/90^o/45^o$
3 Point Bending Tests ASTM D790
Moisture Conditioning - II
Saturation $40^o\ C$ & $90\%\ RH$
Uniaxial Tensile Tests $0^o/90^o/45^o$
3 Point Bending Tests ASTM D790
Compare results and evaluate degradation of mechanical properties

Figure 63: Details of the experimental program

5.7 Validation of the Multiscale-Multiphysics Homogenization Model

In this section, the validation of the unified multiscale-multiphysics formulation for studying the degradation of physical and mechanical properties due to moisture uptake in glass fiber filled (BASF Ultramid® T KR4357 G6) and carbon fiber filled (BASF Ultramid® T KR4370 C6) thermoplastic material system is presented. The validation study consists of two stages namely the preprocessing stage and the macro analysis stage as illustrated in Figure 62 above.

The experimental results of moisture conditioning at $72^{o}C$ & 62% RH as per ISO1110 were used to identify the diffusion model parameters appearing in equation(5.13). The experimental results of the uniform field uniaxial tensile tests were used to identify the elastic and inelastic mechanical properties of the material in the dry as molded (DAM) state and the moisture conditioned state (as per ISO1110). The three point bending test results were used to validate the multiscale-multiphysics unified framework. The microstructure geometry details for the two material systems are summarized in Table 1.

Table 1: Details of the microstructure of the two material systems

Material	Fiber Weight %	Fiber Volume %	Fiber diameter (micron)	Fiber length (micron)	Resin
Glass Fiber SFT BASF Ultramid® T KR4357 G6	30	16	17	125	partially aromatic polyamide
Carbon Fiber SFT BASF, Ultramid® T KR4370 C6	30	22	8	125	partially aromatic polyamide

Studies by Bailey and Rzepka [136] and Toll and Anderson [137, 138] suggest that during the injection molding process, majority of the fibers (~60-65%) align along the melt flow front and the rest (~35-40%) along the cross flow direction giving rise to an orthotropic properties. In the present work, we adopt the terminology wherein the melt flow front direction is referred to as 0^0 orientation and the cross flow direction is referred to as 90^0 orientation. In order to evaluate the orthotropic properties, samples are cut from an injection molded plaque along 0^0 and 90^0 and subjected to uniaxial tensile testing

The modified RSA algorithm [53] described in Chapter 3 was used to generate the unit cell geometries for the two material systems. Utilizing the preferential orientation feature of the RSA algorithm the fibers were constrained to orient along 0^0 and 90^0 with an allowable deviation of ±5^0 so that the unit cell geometry captures the distribution of the fibers found in the test samples. The unit cell finite element meshes for the two material systems are shown in Figure 5. The x-axis in Figure 64 represents the direction of the flow front (0^0 orientation) and the y-axis represents the cross-flow direction (90^0 orientation).

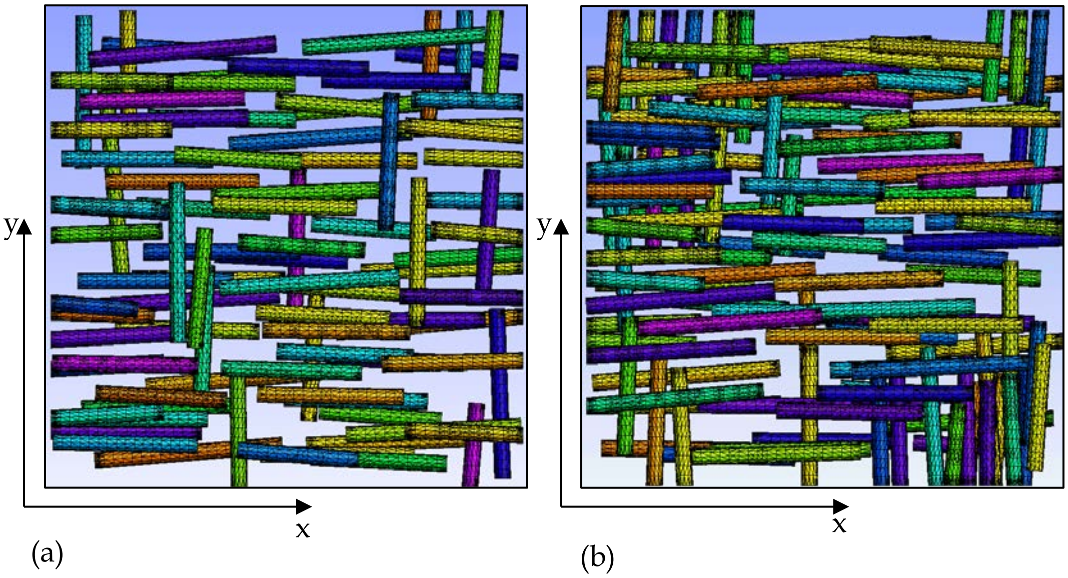

Figure 64 : Unit cell geometry (a) glass fiber filled (BASF, Ultramid® T KR4357 G6) (b) carbon fiber filled polyamide systems (BASF, Ultramid® T KR4370

5.7.1 Moisture Conditioning as per ISO1110 (70C & 62% RH)

A two scale reduced order scalar field homogenization simulations were conducted for the two materials systems. The preprocessing phase was implemented in MDS that involved solving the scalar field influence function problems and the coefficient tensors. Abaqus was used as the macro solver with the homogenization formulation implemented in the user material subroutine UMATHT. The simulations were conducted for three types of specimens namely a tensile specimen, a flex specimen and an impact specimen. The moisture diffusivity was analyzed for partially aromatic polyamide based resin phase whereas the fibers were assumed to be impermeable. A non-linear least squares problem was solved to optimize the material parameters appearing in equation (5.13). The moisture uptake plots for the glass fiber filled thermoplastic material system are presented in Figure 65 to Figure 67.

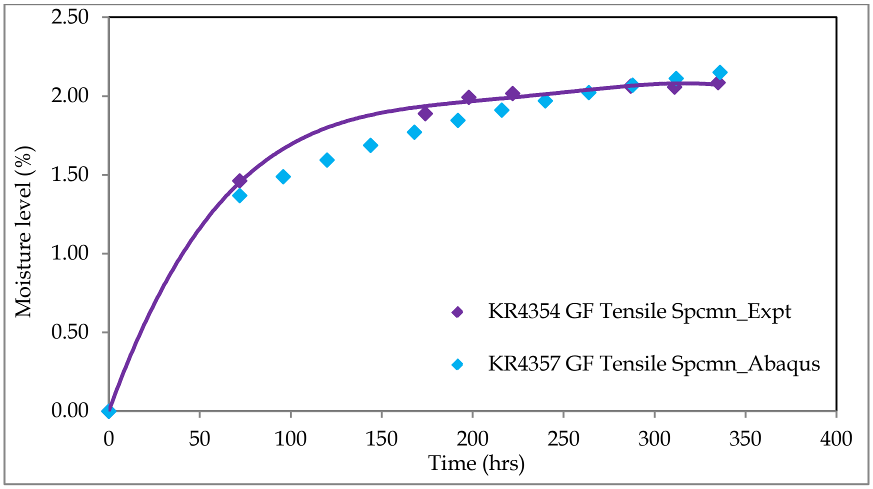

Figure 65: Moisture uptake for glass fiber filled (BASF, Ultramid® T KR4357 G6) tensile specimen

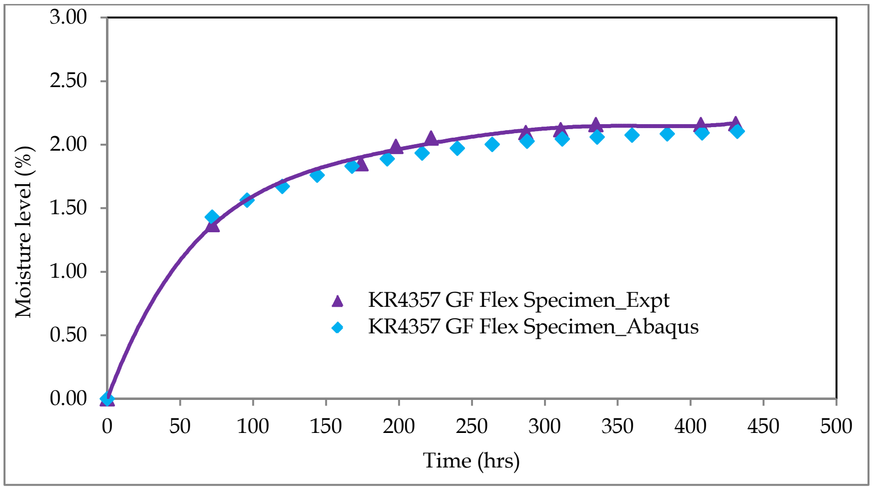

Figure 66: Moisture uptake for glass fiber filled (BASF, Ultramid® T KR4357 G6) flex specimen

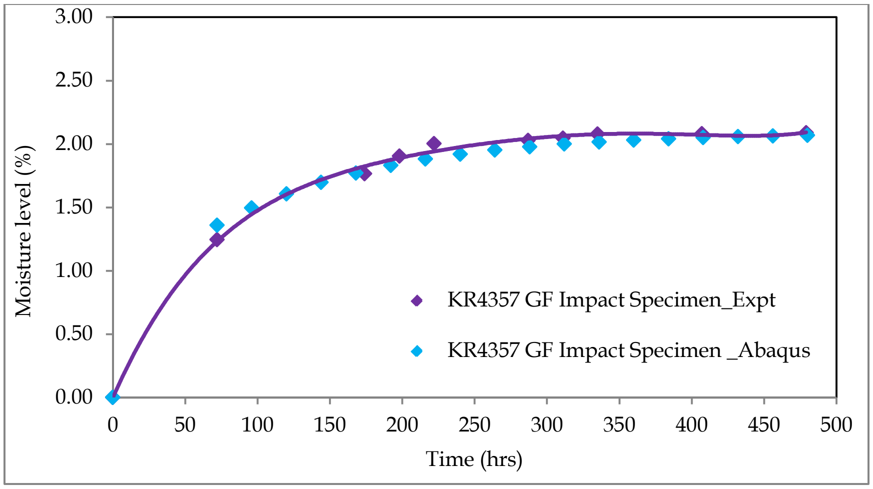

Figure 67: Moisture uptake for glass fiber filled (BASF, Ultramid® T KR4357 G6) impact specimen

The moisture uptake plots for the 30% by weight carbon fiber filled thermoplastic material system are shown in Figure 68 to Figure 70 below

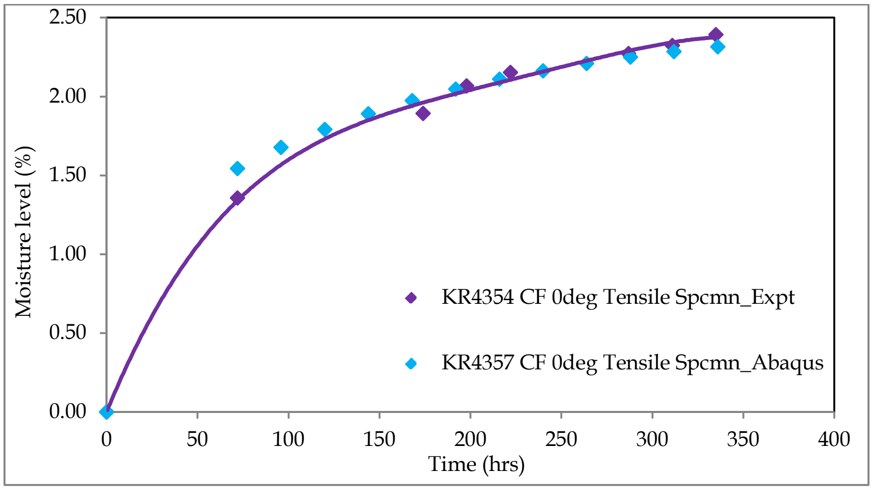

Figure 68: Moisture uptake for carbon fiber filled (BASF, Ultramid® T KR4370 C6) tensile specimen

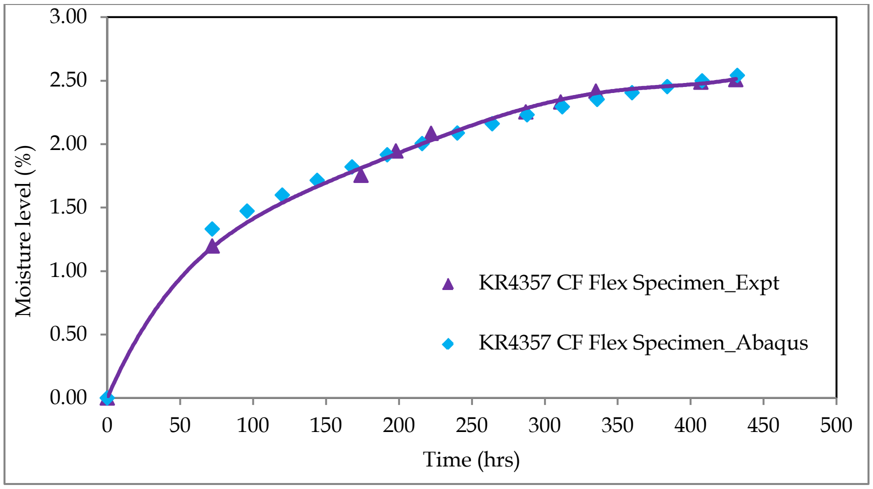

Figure 69: Moisture uptake for carbon fiber filled (BASF, Ultramid® T KR4370 C6) flex specimen

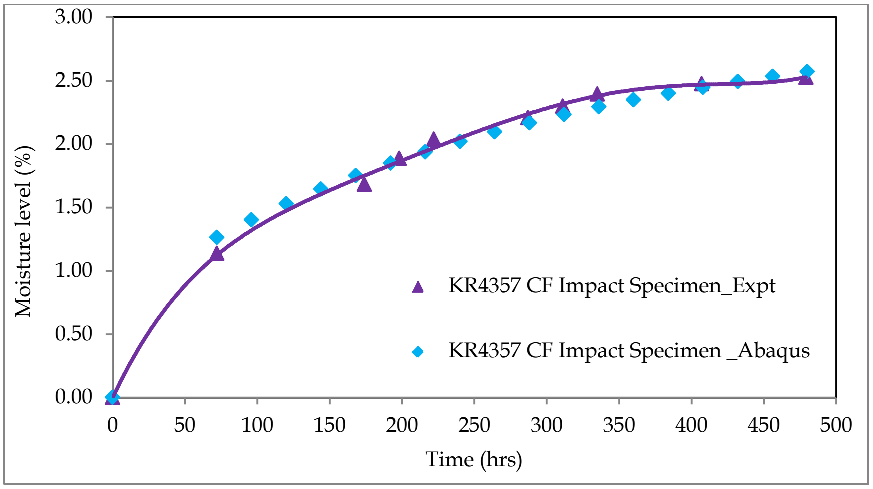

Figure 70: Moisture uptake for carbon fiber filled (BASF, Ultramid® T KR4370 C6) impact specimen

5.7.2 Uniaxial Tensile Tests for Dry As Molded Conditions (ISO 527-2)

A piecewise continuum damage mechanics model was used to model the constitutive behavior of the resin (Figure 71) whereas the fibers were assumed to be linear elastic. The material elastic and inelastic properties for the glass fiber (BASF, Ultramid® T KR4357 G6) and carbon fiber (BASF, Ultramid® T KR4370 C6) filled specimens in the Dry as Molded (DAM) state were identified from uniaxial tensile test simulations as per ISO 527-2 specifications. The model parameters of resin are summarized in

Table 2. The results obtained for the two material systems were found to be in good agreement with the experimental results. The uniaxial tensile test results for the dried glass fiber filled thermoplastic samples are presented in Figure 72 and Figure 73.

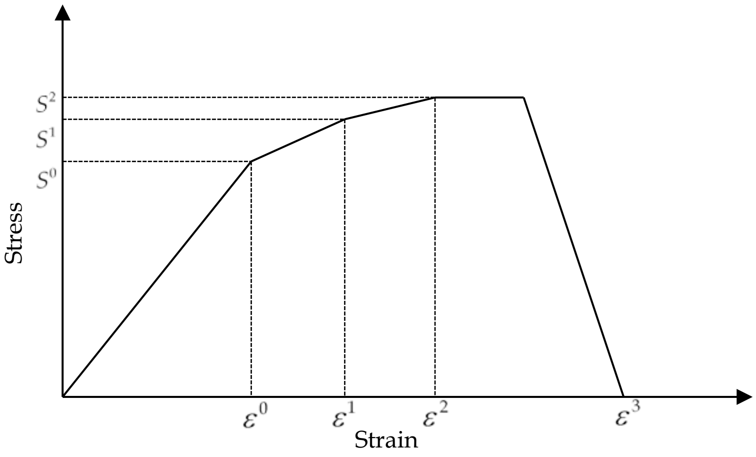
S^2
S^1
S^0
Stress
ε^0
ε^1
ε^2
ε^3
Strain

Figure 71: Schematic of the three-piece linear damage model

Table 2: Parameters of the resin mechanical model

E (GPa)	ν	S^0 (MPa)	S^1 (MPa)	ε^1 (%)	S^2 (MPa)	ε^2 (%)	ε^3 (%)	C
3.5	0.3	40.0	65.0	3.5	70.0	5.0	5.5	0

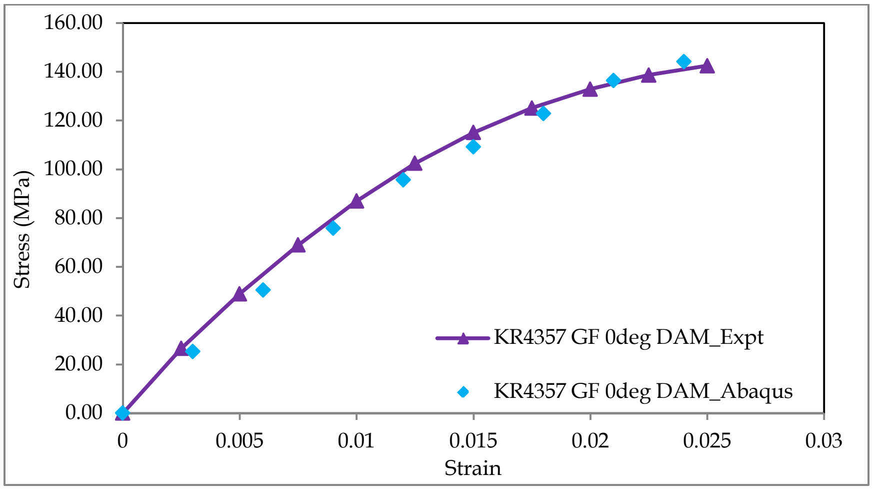

Figure 72: Stress-Strain plot for glass fiber filled (BASF, Ultramid® T KR4357 G6) 0^0 specimen

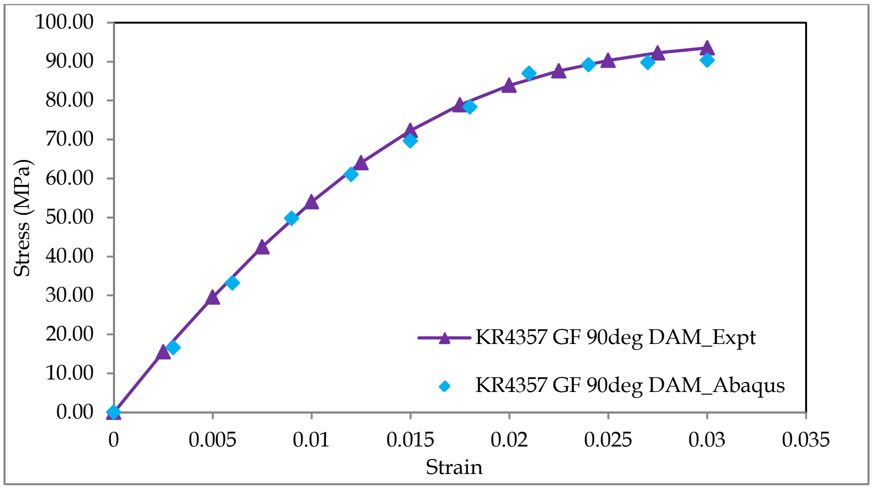

Figure 73: Stress-Strain plot for glass fiber filled (BASF, Ultramid® T KR4357 G6) 90^0 specimen

The uniaxial tensile test results for the dried carbon fiber filled thermoplastic samples are presented in Figure 74and Figure 75.

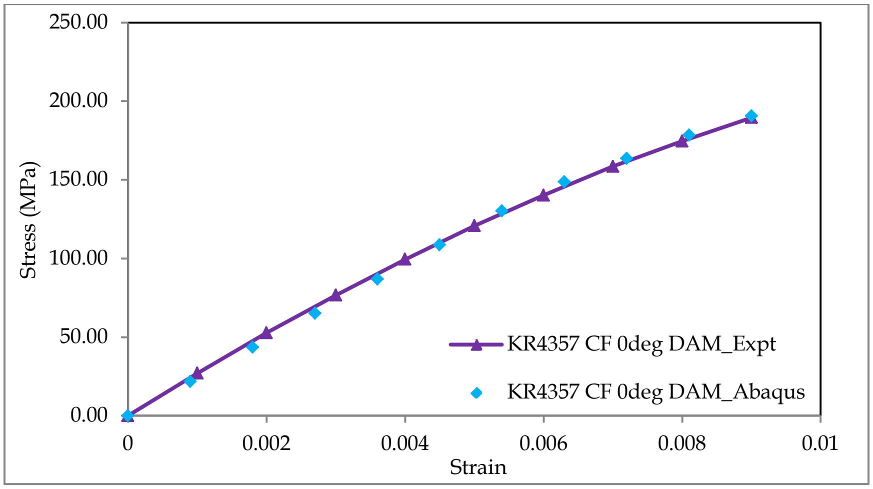

Figure 74: Stress-Strain plot for carbon fiber filled (BASF, Ultramid® T KR4370 C6) 0^0 specimen

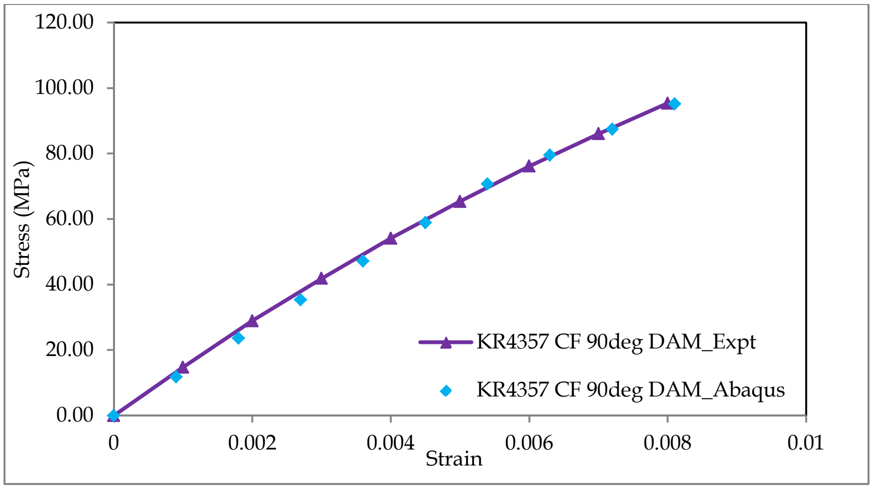

Figure 75: Stress-Strain plot for carbon fiber filled (BASF, Ultramid® T KR4370 C6) 90^0 specimen

5.7.3 Sequential Diffusion-Mechanical Problem

Sequentially coupled simulations were conducted for both the glass fiber (BASF, Ultramid® T KR4357 G6) and carbon fiber (BASF, Ultramid® T KR4370 C6) filled thermoplastic material systems. In the first step the specimen were subjected to moisture ingression as per ISO1110 specifications. The decrease in the elastic modulus and strength of the resin phase due to moisture ingression was computed. The coefficient tensors for the vector field problem were recomputed based on the decreased/updated elastic properties of the resin phase. In the second step the specimen were subjected to uniaxial tensile load and the material elastic and inelastic properties in the moisture conditioned state (ISO1110) were characterized by solving a nonlinear least squares problem. The uniaxial tensile test results for the glass fiber filled thermoplastic material systems are shown in Figure 76 and Figure 77.

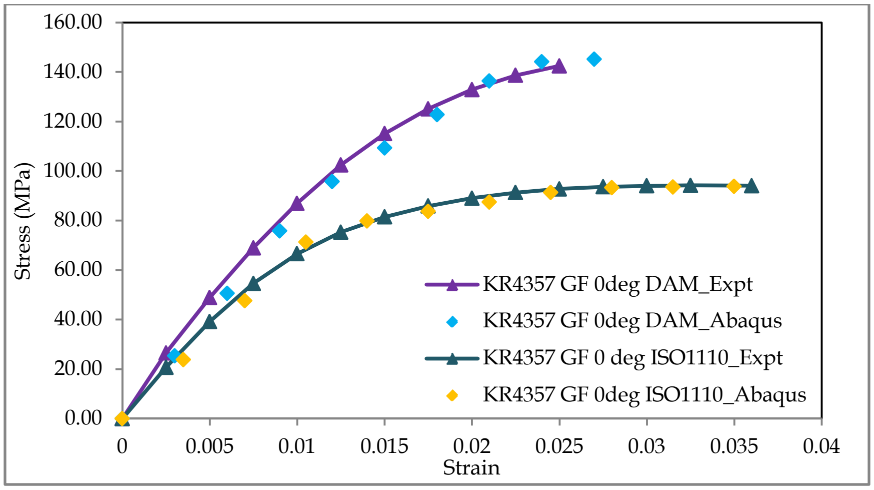

Figure 76: Uniaxial tensile test results for KR4357 GF 0^0 specimen

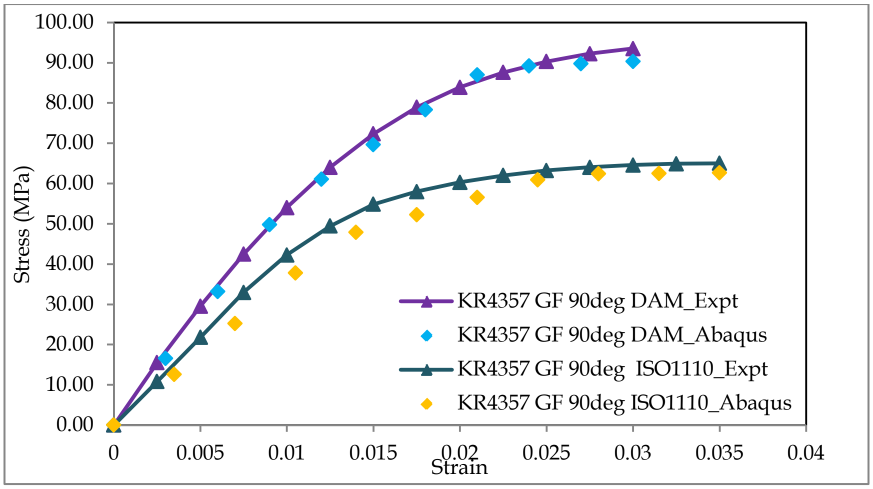

Figure 77: Uniaxial tensile test results for KR4357 GF 90^0 specimen

The uniaxial tensile test results for the carbon fiber filled thermoplastic material systems are shown in Figure 78 and Figure 79.

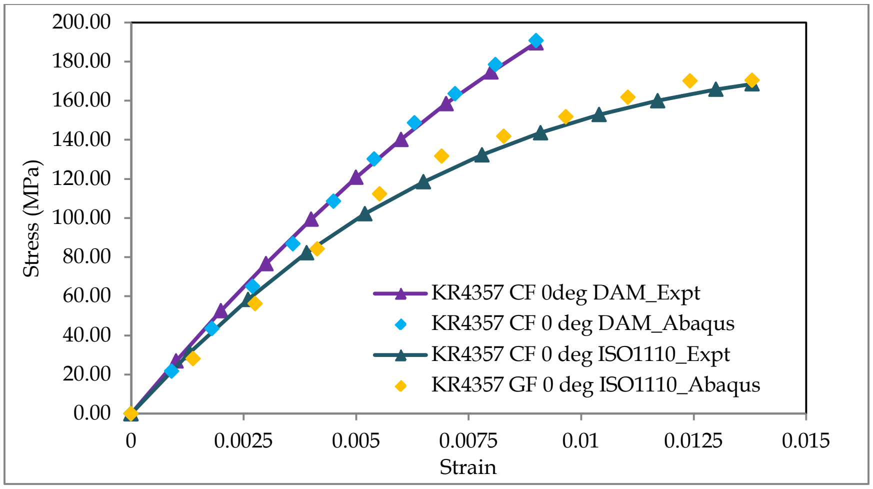

Figure 78: Uniaxial tensile test results for KR4357 CF 0^0 specimen

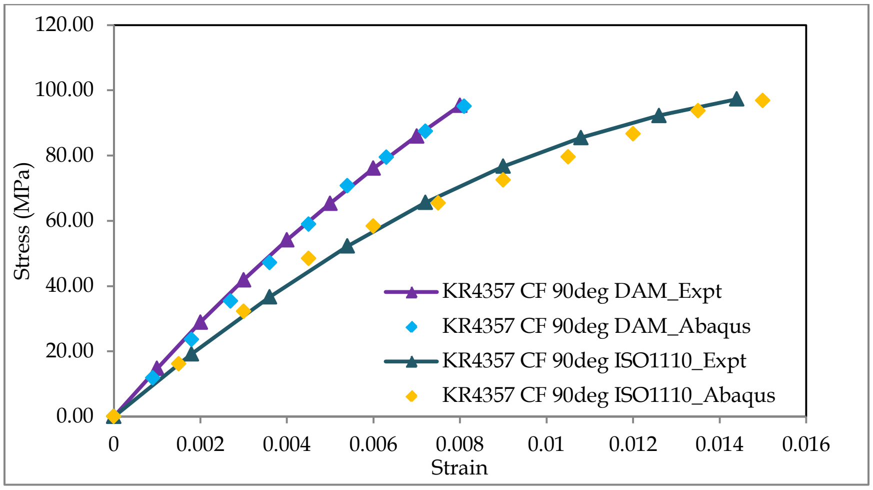

Figure 79: Uniaxial tensile test results for KR4357 CF 90^0 specimen

As is evident from the figures above, the presence of moisture in the resin causes a reduction in the strength and the stiffness of both the glass fiber filled and carbon fiber filled thermoplastic materials. The reduction in the stiffness for the glass fiber filled material is about 13% whereas a 28% reduction in strength is observed in the in-plane directions $(0^o \ \& \ 90^o)$. For the carbon fiber filled material system, a reduction of 19% in the elastic modulus is observed in the in-plane directions whereas the reduction in the strength is below 10%. The relatively less environmental degradation of mechanical properties of the carbon fiber filled material system may be attributed to the higher volume fraction of the impermeable carbon fibers in comparison to the volume fraction of the glass fibers. Additionally, it is also envisaged that the interfaces between the carbon-fiber and resin absorb lesser amounts of moisture than the interfaces in the glass fiber filled material system. The presence of moisture also increases the ductility in both the material systems.

5.7.4 Three Point Bending Test

In this section the three-point bending simulation results for the glass fiber filled thermoplastics are presented. The three point bending simulations were run to validate the scalar and vector field material models used in the coupled multiscale-multiphysics simulations as enumerated in section 5.7.5. The experiments were conducted by General Motors as per ASTM D790 specifications. The sizes of the specimens were 100 mm in length, 25 mm in wide and 3.2 mm in height. A schematic representation of the three-point bending test is presented in Figure 80.

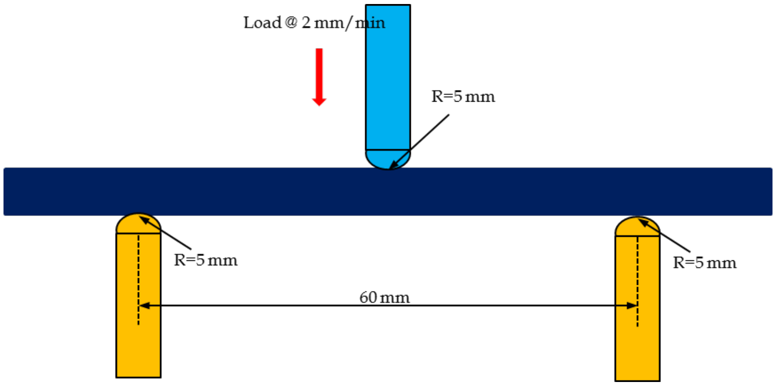

Figure 80: Schematic of the 3-point bending test (ASTM D790)

Abaqus was used as the coarse scale solver for running the three point bending simulations. The finite element model is shown in Figure 81. The simulation program involved running three point bending tests for specimens in the DAM state and moisture conditioned state (ISO1110) followed by comparison of the simulations results with the experimental results to validate the unified multiscale-multiphysics model. The model contained 7112 continuum elements with 7 elements through the thickness.

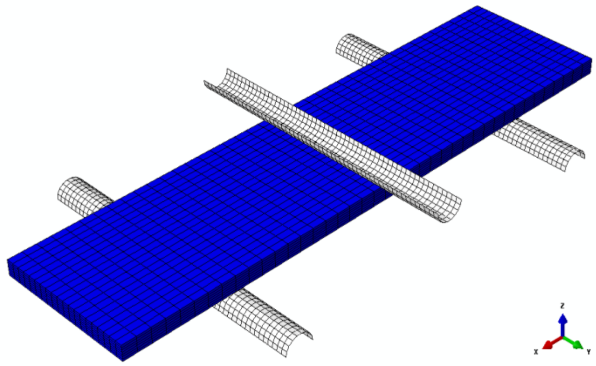

Figure 81: Finite element model of the 3-point bending test (ASTM D790)

The contour plot and the force-displacement plot for the glass fiber filled material in DAM state are presented in Figure 82 and Figure 83 respectively. The maximum deflection is about 8mm at a peak force of 550 N. The simulation results match well with the experimental results thereby validating the material models for the DAM samples.

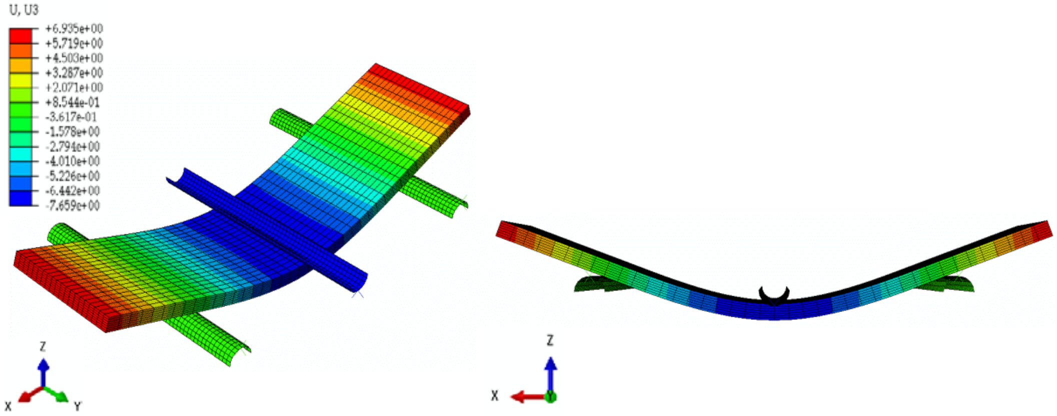
U, U3
+6.935e+00
+5.719e+00
+4.503e+00
+3.287e+00
+2.071e+00
+8.544e-01
-3.617e-01
-1.578e+00
-2.794e+00
-4.010e+00
-5.226e+00
-6.442e+00
-7.659e+00
Z
X
Y
Z
X

Figure 82: Contour plot of the displacements for Ultramid® T KR4357 G6 0^0 samples in DAM state

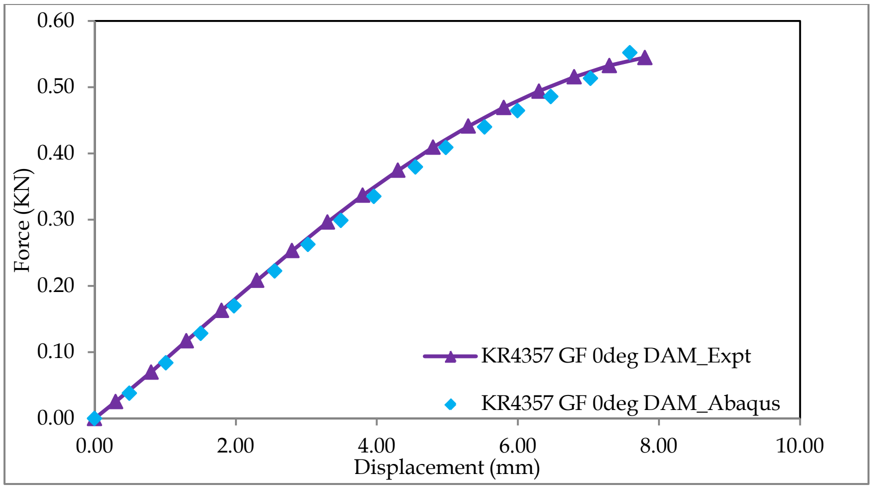

Figure 83: Plot of force-displacement for Ultramid® T KR4357 G6 0^0 samples in DAM state

The contour plot and the force-displacement plot for the moisture conditioned glass fiber thermoplastic samples are presented in Figure 84 and Figure 85 respectively. The maximum deflection is about 10mm at a peak force of 395 N. The increased ductility due to presence of moisture results in a tensile dominant mode of failure. A reduction in strength and stiffness are evident form the simulation results. A 22% decrease in the flexural modulus and 28% decrease in peak force at failure are recorded and they match well with the experimental observations.

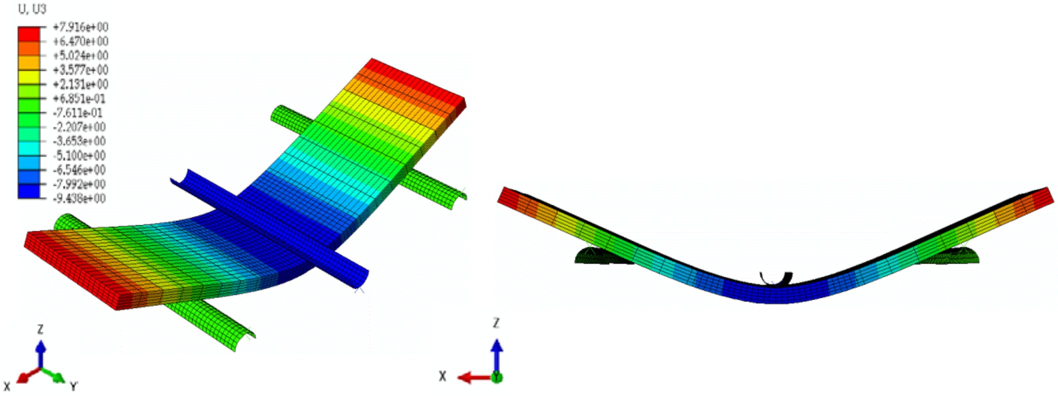
U, U3
+7.916e+00
+6.470e+00
+5.024e+00
+3.577e+00
+2.131e+00
+6.851e-01
-7.611e-01
-2.207e+00
-3.653e+00
-5.100e+00
-6.546e+00
-7.992e+00
-9.438e+00
Z
X
Y
Z
X

Figure 84: Contour plot of the displacements for Ultramid® T KR4357 G6 0^0 samples in moisture conditioned state

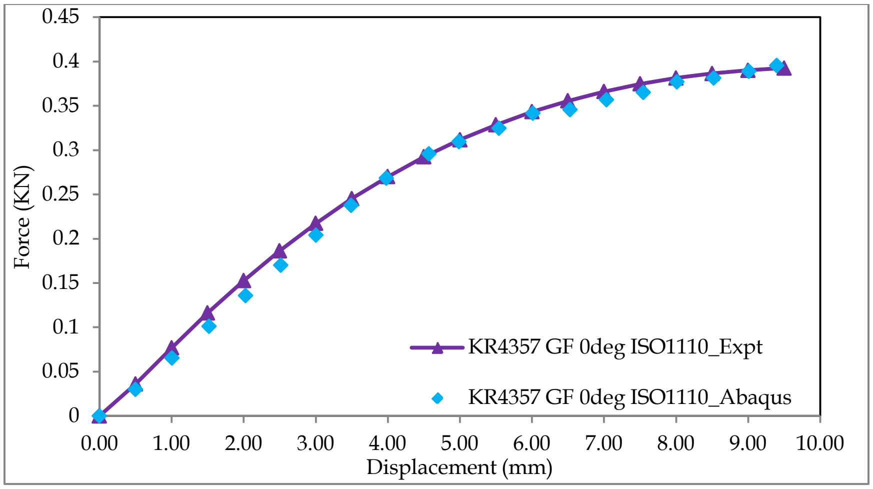

Figure 85: Plot of force-displacement for Ultramid® T KR4357 G6 0^0 samples in moisture conditioned state

The contour plot and the force-displacement plot for the glass fiber filled material in DAM state for the 90° samples are presented in Figure 86 and Figure 87 respectively. The maximum deflection is about 9mm at a peak force of 280 N. The contour plot and the force-displacement plot for the moisture conditioned glass fiber thermoplastic 90° samples are presented in Figure 88 and Figure 89 respectively. The maximum deflection is about 10mm at a peak force of 170 N. A 36% decrease in the flexural modulus and 39% decrease in peak force at failure are recorded and the simulation results match well with the experimental observations.

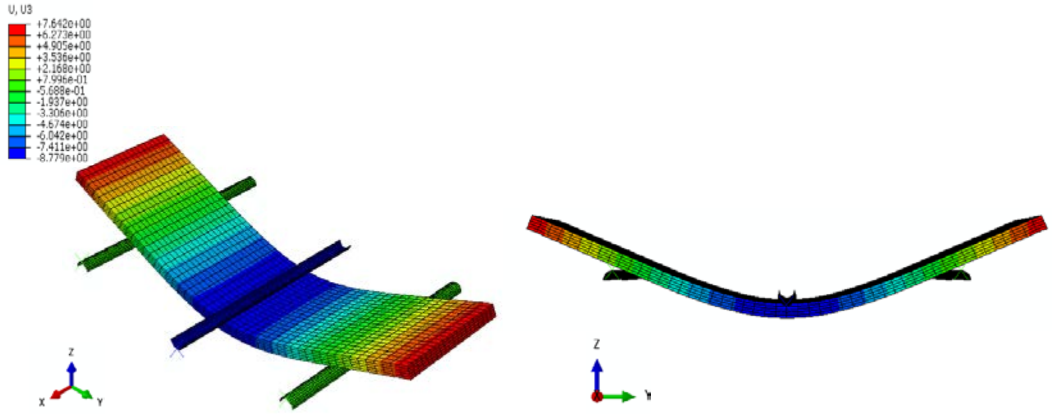
U, U3
+7.642e+00
+6.273e+00
+4.905e+00
+3.536e+00
+2.168e+00
+7.996e-01
-5.688e-01
-1.937e+00
-3.306e+00
-4.674e+00
-6.042e+00
-7.411e+00
-8.779e+00
Z
X
Y
Z
Y

Figure 86: Contour plot of the displacements for Ultramid® T KR4357 G6 90^0 samples in DAM state

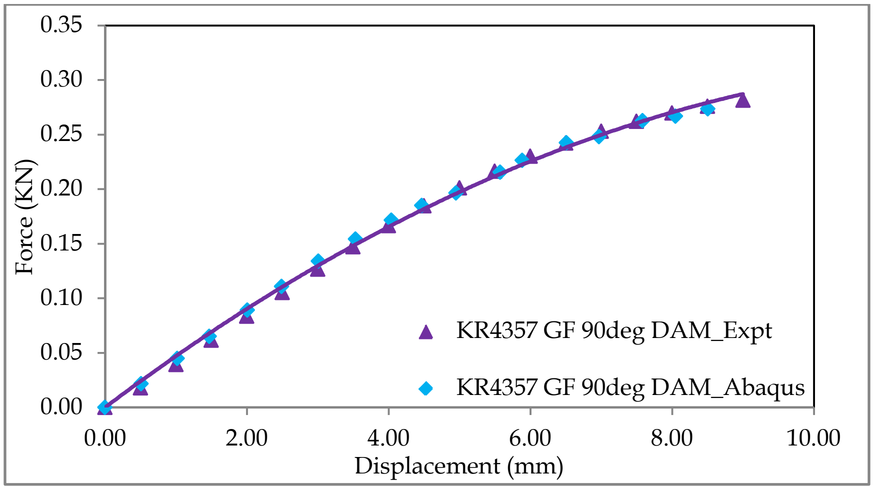

Figure 87: Plot of force-displacement for Ultramid® T KR4357 G6 90^0 samples in DAM state

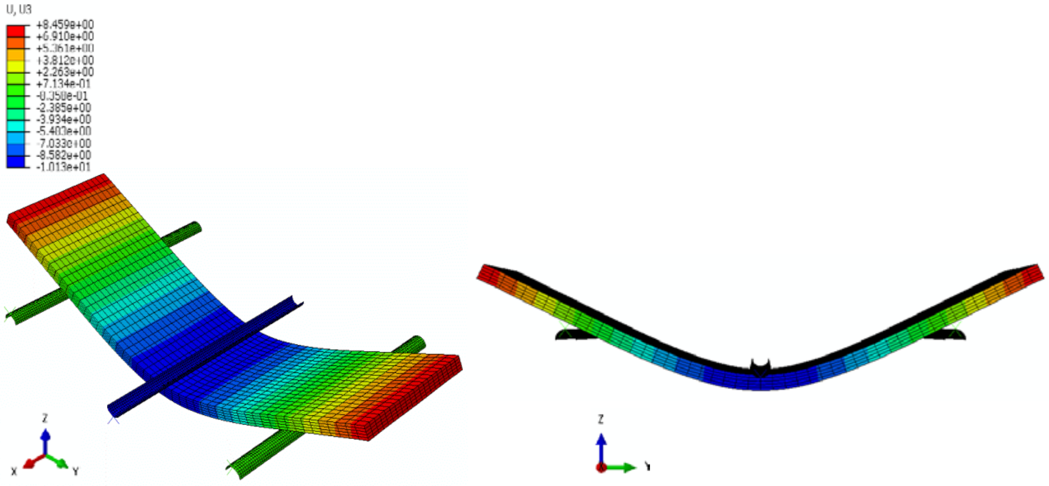
U, U3
+8.459e+00
+6.910e+00
+5.361e+00
+3.812e+00
+2.263e+00
+7.134e-01
-8.358e-01
-2.385e+00
-3.934e+00
-5.403e+00
-7.033e+00
-8.582e+00
-1.013e+01
Z
X
Y
Z
Y

Figure 88: Contour plot of the displacements for Ultramid® T KR4357 G6 90^0 samples in moisture conditioned state

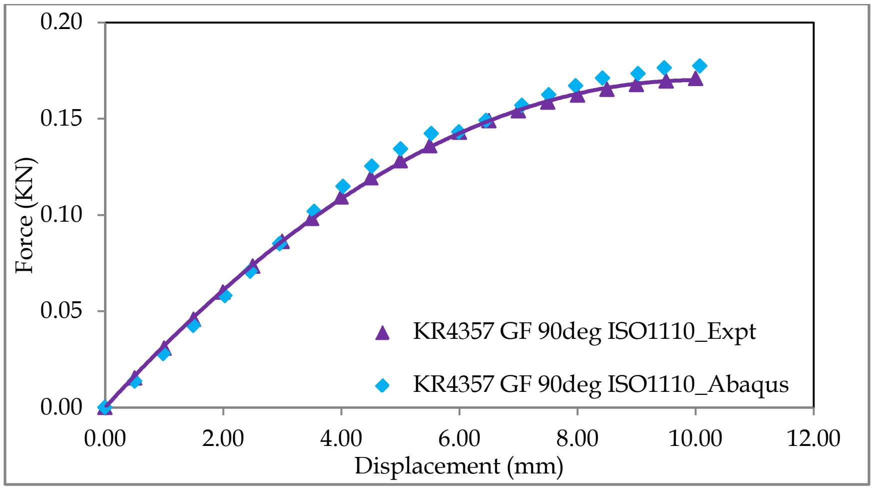

Figure 89: Plot of force-displacement for Ultramid® T KR4357 G6 90^0 samples in moisture conditioned state

5.8 Conclusion

In this chapter A novel computationally efficient multiscale-multiphysics framework was developed for the coupled moisture diffusion - mechanical problem at two relevant scales. The formulation was implemented in MDS with Abaqus as a coarse-scale solver. The model was validated for the 30% by weight filled glass fiber and carbon fiber reinforced thermoplastic composites. The moisture conditioning and uniaxial tension experiments were utilized to characterize the diffusion and mechanical properties at a fine scale. These properties were then used to validate the formulation in a series of three-point bend tests at different moisture conditions and fiber orientations. The proposed formulation has been found to be in good agreement with the experiments conducted by General Motors.

References

1. Composites/Plastics, A.c. 2013; Available from: http://composite.about.com.
2. Voight, W., *Lehrbuch der Krystallphysik*. 1910, Berlin: Teubner.
3. Reuss, V., A., Journal of Applied Mathematics and Mechanics, 1929. **9**(55).
4. Eshelby, J., D., *The determination of the field of an ellipsoidal inclusion and related problems.* Proceedings of Royal Society London, 1957. **241**: p. 376-396.
5. Hashin, Z., *The elastic moduli of heterogeneous materials.* Journal of Applied Mechanics, 1962. **29**: p. 143-150.
6. Budiansky, B., *On the elastic moduli of some hetrogeneous materials.* Journal of Mechanics and Physics of Solids, 1965. **13**: p. 223-227.
7. Mori, T. and K. Tanaka, *Average stress in the matrix and average elastic energy of materials with misfitting inclusions.* Acta Metallurgia, 1973. **21**: p. 571-574.
8. Hill, R., *A self-consistent mechanics of composite materials.* Journal of Mechanics and Physics of Solids, 1965. **13**: p. 357-372.
9. Christensen, R.M. and K.H. Lo, *Solution for effective shear properties in three phase sphere and cylinder models.* Journal of Mechanics and Physics of Solids, 1979. **27**: p. 315-330.
10. Hashin, Z. and S. Shtrikman, *A variational approach to the theory of the elastic behaviour of multiphase materials.* Journal of Mechanics and Physics of Solids, 1963. **11**: p. 127-140.
11. Hashin, Z., *Analysis of composite materials. A survey.* journal of Mechanics and Physics of Solids, 1983. **50**: p. 481-505.
12. Willis, J., R., *Variational and related methods for the overall properties of composites.* Advanced Applied Mechanics, 1981. **21**: p. 1-78.

13. Ponte Castaneda, P. and P. Suquet, *Nonlinear Composites.* Advanced Applied Mechanics, 1998. **34**: p. 171-302.

14. Bensoussan, A., J.L. Lions, and G. Papanicolaou, *Asymptotic analysis for periodic structures*. 1978: North-Holland.

15. Sanchez-Palencia, E., *Non-homogeneous media and vibration theory*. 1980, Berlin: Springer-Verlag.

16. Bakhvalov, N.S. and G. Panasenko, *Homogenization: Averaging processes in periodic media*. Vol. 36. 1989, London: Kluwer Academic Publishers.

17. J.M.Guedes and N.Kikuchi, *Preprocessing and postprocessing for materials based on the homogenization method with adaptive finite element methods.* Computer methods in applied mechanics and engineering, 1990. **83**: p. 143-198.

18. Terada, K. and N. Kikuchi, *Nonlinear homogenization method for practical applications.* Computational Methods in Micromechanics, ASME, AMD - 212/MD, 1995. **62**: p. 1-16.

19. Ghosh, S., K. Lee, and S. Moorthy, *Multiple scale analysis of heterogeneous elastic structures using homogenization theory and Voronoi cell finite element method.* International Journal of Solids and Structures, 1995. **32**: p. 27-62.

20. Ghosh, S., K. Lee, and S. Moorthy, *Two scale analysis of heterogeneous elasticplastic materials with asymptotic homogenization and Voronoi cell finite element model.* Computational Methods in Applied Mechanics and Engineering, 1996. **132**: p. 63-116.

21. Smit, R., J., M., W. Brekelmans, A., M.,, and H. Meijer, E., H., *Prediction of the mechanical behavior of nonlinear heterogeneous systems by multilevel finite element modeling.* Computational Methods in Applied Mechanics and Engineering, 1998. **155**: p. 181-192.

22. Miehe, C. and A. Koch, *Computational micro-to-macro transition of discretized microstructures undergoing small strain.* Archive of Applied Mechanics, 2002. **72**: p. 300-317.

23. Michel, J.C., H. Moulinec, and P. Suquet, *Effective properties of composite materials with periodic microstructure: a computational approach.* Computational Methods in Applied Mechanics and Engineering, 1999. **172**: p. 109-143.

24. Feyel, F. and J. Caboche, L., *FE2 multiscale approach for modeling the elastoviscoplastic behavior of long fiber sic/ti composite materials.* Computational Methods in Applied Mechanics and Engineering, 2000. **183**: p. 309-330.

25. Kouznetsova, V., W. Brekelmans, A., M.,, and F. Baaijens, P., T., *An approach to micromacro modeling of heterogeneous materials.* Computational Mechanics, 2001. **27**: p. 37-48.

26. Fish, J., et al., *Computational plasticity for composite structures based on mathematical homogenization: theory and practice.* Comput. Meth. Appl. Mech. Engng., 1997. **148**: p. 53-73.

27. Fish, J., Q. Yu, and K.L. Shek., *Computational damage mechanics for composite materials based on mathematical homogenization.* Int. J. Numer. Meth. Engng., 1999. **45**: p. 1657–1679.

28. Fish, J. and Q. Yu, *Multiscale Damage Modeling for Composite Materials: Theory and Computational Framework.* International Journal for Numerical Methods in Engineering, 2001. **52**: p. 161-192.

29. Dvorak, G., J. and Y. Benveniste, *On transformation strains and uniform fields in multiphase elastic media.* Proceedings of Royal Society A, London, 1992. **437**: p. 291-310.

30. Dvorak, G.J., *Transformation field analysis of inelastic composite materials.* Proceedings: Mathematical and Physical Sciences, 1992. **437**: p. 311-327.

31. Oskay, C., Fish, J., *Eigendeformation-Based Reduced Order Homogenization.* Comp. Meth. Appl. Mech. Engng., 2007. **196**: p. 1216-1243.

32. Yuan, Z.a.F., J., *Multiple Scale Eigendeformation-Based Reduced Order Homogenization.* Comp. Meth. Appl. Mech. Engng., 2009. **198**(21-26): p. 2016-2038.

33. Yuan, Z. and J. Fish, *Multiple scale eigendeformation-based reduced order homogenization.* Comp. Meth. Appl. Mech. Engng., 2009. **198**(21-26): p. 2016-2038.

34. Michopoulos, J., G., J. Fish, and C. Farhat, *Survey on modeling and simulation of multiphysics systems.* Journal of Computing and Information Science in Engineering, 2005. **5**(3): p. 198-213.

35. Yuan, Z. and J. Fish, *Hierarchical model reduction at multiple scales.* International Journal for Numerical Methods in Engineering, 2009. **79**(3): p. 314-339.

36. Ghosh, S. and S. Moorthy, *Elastic-Plastic Analysis of Heterogeneous Microstructures Using the Voronoi Cell Finite Element Method.* Computational Methods in Applied Mechanics and Engineering, 1995. **121**: p. 373-409.

37. Aboudi, J., *A continuum theory for fiber-reinforced elastic-viscoplastic composites.* Journal of Engineering Science, 1982. **20**(55): p. 605-621.

38. Berlyand, L.V. and A.G. Kolpakov, *Network approximation in the limit of small interparticle distance of the effective properties of a high-contrast random dispersed composite.* Archive for Rational Mechanics and Analysis, 2001. **159**: p. 179-227.

39. Moulinec, H. and P. Suquet, *A fast numerical method for computing the linear and nonlinear properties of composites.* C. R. Acad. Sci. Paris - Series II, 1994. **318**: p. 1417-1423.

40. Moulinec, H. and P. Suquet, *A numerical method for computing the overall response of nonlinear composites with complex microstructure.* Comput. Meth. Appl. Mech. Engng, 1998. **157**: p. 69-94.

41. Cusatis, G., A. Mencarelli, and D. Pelessone. in *Proc. of the 2008 ASCE Structures Congress* 2008.

42. Cusatis, G., et al. in *Proceedings of IMECE*. 2007.

43. Bahei-El-Din, A. Rajendran, M., and M. Zikry, A., *A micromechanical model for damage progression in woven composite systems.* International Journal of Solids and Structures, 2004. **41**: p. 2307-2330.

44. Moore, B.C., *Principal component analysis in linear systems: controllability, observability, and model reduction.* IEEE Transactions on Automatic Control, 1981. **26**: p. 17-32.

45. Green, M., *A relative-error bound for balanced stochastic truncation.* IEEE Transactions on Automatic Control, 1988. **33**(10): p. 961-965.

46. GLover., K., *All optimal Hankel-norm approximation of linear multivariable systems and their -error bounds.* International Journal of Control, 1984. **39**: p. 1115-1193.

47. Krysl, P., S. Lall, and J. Marsden, E., *Dimensional model reduction in non-linear finite element dynamics of solids and structures.* International Journal for Numerical Methods in Engineering, 2001. **51**(4): p. 479-504.

48. Laws, N., *On the thermostatics of composite materials.* Journal of Mechanics and Physics of Solids, 1973. **21**(1): p. 9-17.

49. Dvorak, G.J., *On unifrom fields in hetrogeneous media.* Proceedings of Royal Society A, London, 1990. **431**: p. 89-110.

50. Oskay, C. and J. Fish, *Fatigue Life Prediction using 2-Scale Temporal Asymptotic Homogenization.* International Journal for Numerical Methods in Engineering, 2004. **61**(3): p. 329-359.

51. Oskay, C. and J. Fish, *Eigendeformation-Based Reduced Order Homogenization.* Comp. Meth. Appl. Mech. Engng., 2007. **196**: p. 1216-1243.

52. Fish, J., *Multiscale Methods: Bridging the scales in science and engineering*. 2008: Oxford University Press.

53. Bailakanavar, M., et al., *Automated modeling of random inclusion composites.* Engineering with Computers, 2012. **DOI 10.1007/s00366-012-0310-x**.

54. Wentorf, R., Collar, R., Shephard M.S., Fish, J., *Automated modeling for complex woven mesostructures.* Comput. Meth. Appl. Mech. Engng, 1999. **172**(1): p. 273-291.

55. Gusev, A.A., *Representative volume element size for elastic composites: a numerical study.* Journal of Mechanics and Physics of Solids, 1997. **45**: p. 1449-59.

56. Gusev, A.A., Heggli, M., Lusti, H.R., Hine, P.J., *Orientation averaging for stiffness and thermal expansion of short fiber composites.* Advanced Engineering Materials, 2002. **4**(12): p. 931-933.

57. Duschlbauer, D., Bohm, H.J., Pettermann, H.E., *Computational Simulation of Composites Reinforced by Planar Random Fibers: Homogenization and Localization by Unit Cell and Mean Field Approaches* Journal of Composite Materials, 2006. **40**(24): p. 2217–2234.

58. Widom, B., *randomsequential adition of hard spheres to a volume.* Journal of Chemical Physics, 1966. **44**(10): p. 3888-3894.

59. Bohm, H.J., Eckschlager, A., Han, W., , *Multinclusion unit cell models for metal matrix composites with randomly oriented discontinuous reinforcements.* Computational Materials Science, 2002. **25**: p. 42-53.

60. Torquato S., H.H., *Random heterogeneous materials: microstructure and macroscopic properties.* Applied Mechanics Reviews, 2002. **55**(4): p. B62.

61. Williams, S.R., Philipse, A.P., *Random packing of spheres and spherocylinders simulated by mechanical contraction.* Physics review E, 2003. **67**: p. 051301-1-9.

62. Tu, S., T., et al., *Numerical simulationof saturation behavior of physical properties in composites with randomly distributed second phase.* Journal of Composite Materials, 2005. **39**(7): p. 671-631.

63. Kari, S., Berger, H., Gabbert, U., *Numerical evaluation of effective material properties of randomly distributed short cylindrical fiber composites.* Computational Materials Science, 2007. **39**: p. 198-204.

64. Pan, Y., Iorga, L., Pelegri, A.A., *Numerical generation of a random chopped fiber composite RVE and its elastic properties.* Composites Science and Technology, 2008. **68**: p. 2792-2798.

65. Toll, S., *Packing mechanics of fiber reinforcements.* Polymer Engineering and Sciemce, 1998. **38**(18): p. 1337-1350

66. Lubachevsky, B.D., Stillinger, F.H., *Geometric properties of random disk packings.* Journal of Statistical Physics, 1990. **60**: p. 561-583.

67. Stafford DS., J.T., *Unisng level sets for creating virtual random packs of non spherical convex shapes.* Journal of COmputational Physics, 2010. **229**(9): p. 3295-3315.

68. Hinrichsen, E.L., Feder, J., Jossang, T., *Geometry of random sequential adsorption.* Journal of Statistical Physics, 1986. **44**: p. 793-827.

69. Cooper, D.W., *Random sequential packing simulations in three dimensions for spheres.* Physics Review A, 1988. **38**: p. 522-524.

70. Sherwood, J.D., *Packing of spheroids in three-dimensional space by random sequential addition.* Journal of Physics A, 1997. **30**(24).

71. Evans, K.E., Ferrar, M.D., *The packing of thick fibers.* Journal of Physics D, 1989. **22**: p. 354-360.

72. Parkhouse, J.G., Kelly, A., *The random packing of fibers in three dimensions.* Proceedings: Mathematical and Physical Sciences, 1995. **451**(1943): p. 737-746.

73. Evans, K.E., Gibson, A.G., *Prediction of the maximum packing fraction achievable in randomly oriented short fiber-composites.* Composites Science and Technology, 1986. **25**: p. 149-162.

74. Sunday, D., *3D game engine design: a practical approach to real-time computer graphics*. 1 ed. 2000: Morgan Kaufmann.

75. Eberley, D. *Distance between two line segmetns in 3D*. 1999; Available from: http://www.geometrictools.com/.

76. Teller, S. *Closese approach of two lines in 3D*. 2000; Available from: http://people.csail.mit.edu/seth/geomlib/geomlib.html.

77. Eberley, D. *Intersection of convex objects: The method of separating axis*. 2001; Available from: http://www.geometrictools.com/.

78. Ionita, A., Weitsman, Y.J., *On the mechanical response of randomly reinforced chopped-fibers composites: data and model.* Composites Science and Technology, 2006. **66**: p. 2566-2579.

79. Drugan, W.J., Willis, J.R., *A micro-mechanical base nonlocal constitutive equation and estimates of representative volume element size for elastic composites* Journal of Mechanics and Physics of Solids, 1996. **44**(4): p. 497-524.

80. Kanit, T., Forest, S., Galliet, I., Mounoury, V., Jeulin, D., *Determination fo the size of the representative volume element for random composites: statisticaland numerical approach.* International Journal of Solids and Structures, 2003. **40**: p. 3647-3679.

81. Huet, C., *Application of variational concepts to size effects in elastic heterogeneous bodies.* Journal of Mechanics and Physics of Solids, 1990. **38**: p. 813-841.

82. Sab, K., *On the homogenization and simulation of random materials.* European Journal of Mechanics : A/Solids, 1992. **11**: p. 585-607.

83. Ostoja-Starzewski, M., *Random fields of heterogeneous materials.* International Journal of Solids and Structures, 1998. **35**(19): p. 2429-2455.

84. Fish, J. and M. Bailakanavar, *Multiscale fatigue life prediction model for hetrogeneous materials.* International Journal for Numerical Methods in Engineering, 2012. **91**(10): p. 1087-1104.

85. Schutz, W., *A history of fatigue.* Engineering Fracture Mechanics 1996(54): p. 263-300.

86. Albert, W.A.J., *Über treibseile am Harz.* Archive für Mineralogie Geognosie Bergbau und Hüttenkunde, 1838. **10**: p. 215-34.

87. Wöhler, A., *Ueber die Festigkeits-versuche mit Eisen und Stahl.* Zeitschrift für Bauwesen, 1870. **20**: p. 73-106.

88. Paris, P.C. and F.A. Erdogan, *A critical analysis of crack propagation laws.* J. Basic Eng., 1963. **85**: p. 528-534

89. Manson, S.S., *Behaviour of materials under conditions of thermal stress.* Heat Transfer Symposium, University of Michigan Engineering Research Institute, 1953: p. 9-75.

90. Coffin, L.F., *A Study of the effects of cyclic thermal stresses on a ductile metal.* Trans. American Society for Testing and Materials, 1954. **76**: p. 931-950.

91. Chaboche, J.L., *Continuum damage mechanics I: General concepts & II: Damage growth, crack initiation and crack growth.* J. Appl. Mech, 1988. **55**: p. 59-72.

92. Chow, C.L. and Y. Wei, *A model of continuum damage mechanics for fatigue failure.* Int. J. Fatigue, 1991. **50**: p. 301-306.

93. Fatemi, A. and L. Yang, *Cumulative fatigue damage and life prediction theories: a survey of the start of the art for homogeneous materials.* Int. J. Fatigue, 1998. **20**(1): p. 9-34.

94. Pass, M.H.J.W., P.J.G. Schreurs, and W.A.M. Brekelmans, *A continuum approach to brittle and fatigue damage: Theory and numerical procedures.* Int. J. Solids Structures, 1993. **30**(4): p. 579-599.

95. Bhattacharya, B. and B. Ellingwood, *A new CDM-based approach to structural deterioration.* Int. J. Solids Structures, 1999. **36**: p. 1757-1779.

96. Bonora, N. and G.M. Newaz, *Low cycle fatigue life estimation for ductile metals using a nonlinear continuum damage mechanics model.* Int. J. Solids Structures, 1998. **35**(16): p. 1881-1894.

97. Papa, E., *A damage model for concrete subjected to fatigue loading.* Eur. J. Mech. A/Solids, 1993. **12**(3): p. 429-440.

98. Talreja, R., *Fatigue of Composite Materials*. Technomic Publishing Company, Inc., Lancaster, PA. 1987.

99. Fish, J., Yu, Q., *Computational Mechanics of Fatigue and Life Predictions for Composite Materials and Structures.* Comp. Meth. Appl. Mech. Engng., 2002. **191**(4827-4849).

100. Elber, W., *Fatigue crack closure under cyclic tension.* Engng. Fracture Mech., 1970. **2**(37-45).

101. Foreman, R.G., V.E. Keary, and R.M. Engle, *Numerical analysis of crack propagation in cyclic-loaded structures.* J. Basic Engng., 1967. **89**: p. 459–464.

102. Klesnil, M. and P. Lukas, *Influence of strength and stress history on growth and stabilization of fatigue cracks.* Engng. Fracture Mech., 1972. **4**: p. 77-92.

103. Wheeler, O.E., *Spectrum loading and crack growth.* J. Basic Engng., 1972. **94**: p. 181-186.

104. Nguyen, O., et al., *A cohesive model of fatigue crack growth.* Int. J. Fracture, 2001. **110**(4): p. 351-369.

105. Lemaitre, J., Doghri, I. , *A post processor for crack initiation* Comp. Meth. Appl. Mech. Engng., 1994(115): p. 197-232.

106. Billardon, R., *Etude de la rupture par la mecanique de I'endommagement*. 1989, Universite Paris.

107. Paas, M.H.J.W., Schreurs, P.J.G., Brekelmans, W.A.M., *A continuum approach to brittle and fatigue damage: theory and numericalprocedures.* Journal of Solid Structures, 1993. **30**(4): p. 579-599.

108. Yu, Q., Fish J., *Temporal homogenization of viscoelastic and viscoplastic solids subjected to locally periodic loading.* Computational Mechanics, 2002. **29**: p. 199–211.

109. Oskay, J.F.a.C., *Nonlocal Multiscale Fatigue Model.* Mechanics of Advanced Materials and Structures, 2005. **12**(6): p. 485-500.

110. Devulder, A., D. Aubry, and G. Puel, *Two-time scale fatigue modeling: application to damage.* Computational Mechanics, 2010. **45**(6): p. 637-646.

111. Peerlings, R.H.J., Brekelmans, W.A.M., R. de Borst, Geers, M.G.D, *Gradient-enhanced damage modeling of high-cycle fatigue.* International Journal for Numerical Methods in Engineering, 2000(49): p. 1547-1569.

112. Marigo, J.J., *Modelling of brittle and fatigue damage for elastic material by growth of micro-voids* Engrg. Fract. Mech. , 1985. **21**(4): p. 861-874.

113. Gunnell, J., *Standard Catalog of American Cars, 1946-1975*. 1987: Krause Publications.

114. NHTSA, D., *A safety roadmap for future plastics and composites itensive vehicles*. November 2007. p. 104.

115. Lovins, A. and D. Cramer, *Hypercars, hydrogen, and automotive transition.* International Journal of Vehicle Design, 2004. **35**(1/2): p. 50-84.

116. Jackson, R., B. and W. Schlesinger, H. *Curbing the US carbon deficit*. in *Proceedings of the National Academy of Sciences of the United States of America*. 2004.

117. Brinson, L., C., *Meeting the emerging demand for durable polymer matrix composites*. 2005: The national Academies Press.

118. Puffr, R. and J. Sebenda, *On the structure and properties of polyamides. XXVII. The mechanism of water sorption in polyamides.* Journal of Polymer Science:Part C, 1967. **16**(1): p. 79-93.

119. Grossman, S., D. Tirrell, and O. Vogl, *Water binding in regular copolyoxamide membranes.* 1980: ACS Publications.

120. Kohan, M., I., *Nylon Plastics Handbook*. 1995, New York: Hanser Gardner Publications. 631.

121. *Effects of moisture conditioning methods on mechanical properties of injection molded nylon 6.* 2003 [cited 2013; Available from: http://www2.basf.us//PLASTICSWEB/displayanyfile?id=0901a5e18000488a.

122. Reimschuessel, H., K., *Relationships on the effect of water on glass transition temperature and young's modulus of nylon 6.* Journal of Polymer Science: Polymer Chemistry Edition, 1978. **16**(6): p. 1229-1236.

123. Kettle, G., J., *Polymer*. 1977. **18**: p. 742.

124. Clark, R., L., M. Craven, D., and R. Kander, G., *Nylon 66/poly(vinyl pyrrolidone) reinforced composites: 2: Bulk mechanical properties and moisture effects.* Composites Part A: Applied Science and Manufacturing, 1999. **30**(1): p. 37-48.

125. Pai, C., C., R. Jeng, U., and S. Grossman, J., *Effects of moisture on thermal and mechanical properties of nylon-6, 6*.* Advances in Polymer Technology, 2003. **9**(2): p. 157-163.

126. Jia, N., V. Kagan, A., and H. Fraenkel, A., *Effects of moisture conditioning methods on the mechanical properties of injection molded nylon-6.* Journal of Reinforced Plastics and Composites, 2004. **23**: p. 729-737.

127. Gerard, B., G. Pijaudier-Cabot, and C. Laborderie, *Coupled diffusion-damage modelling and the implications on failure due to strain localisation. International Journal of Solids and Structures.* International Journal of Solids and Structures, 1998. **35**(31-32): p. 4107-4120.

128. Gerard, B., C. Le Bellego, and O. Bernanrd, *Simplified modelling of calcium leaching of concrete in various environment.* Materials and Structures, 2002. **35**: p. 632-640.

129. Ulm, F.J., E. Lemarchand, and F. Heukamp, H., *Elements of chemomechanics of calcium leaching of cement-based materials at different scales.* Engineering Fracture Mechanics, 2003. **70**: p. 871-889.

130. Oskay, C. and M. Haney, *Computational modeling of titanium structures subjected to thermo-chemo-mechanical environment.* International Journal of Solids and Structures, 2010. **47**: p. 3341-3351.

131. Ozdemir, I., W.A.M. Brekelmans, and M. Geers, G., D., *FE2 computational homogenization for the thermo-mechanical analysis of heterogeneous solids.* Computational Methods in Applied Mechanics and Engineering, 2008. **198**: p. 602-613.

132. Terada, K. and M. Kurumatani, *Two-scale diffusion–deformation coupling model for material deterioration involving micro-crack propagation.* International Journal for Numerical Methods in Engineering, 2010. **83**(4): p. 426-451.

133. Yu, Q. and J. Fish, *Multiscale asymptotic homogenization for multiphysics problems with multiple spatial and temporal scales: a coupled thermo-viscoelastic example problem.* International Journal of Solids and Structures, 2002. **39**(26): p. 6429-6452.

134. Kuznetsov, S. and J. Fish, *Mathematical homogenization theory for electroactive continuum.* International Journal for Numerical Methods in Engineering, 2012. **91**(11): p. 1199-1226.

135. *Multiscale Design Systems.* [cited 2013; Available from: http://multiscale.biz/.

136. Bailey, R., S. and S. Rzepka, *Fibre orientation mechanisms for injection molding of long fibre composites.* International Polymer Processing, 1991. **6**(1): p. 35-41.

137. Toll, S. and P. Andersson, O., *Microstructural characterization of injection molded composites using image analysis.* Composites, 1991. **22**(4): p. 298-306.

138. Toll, S. and P. Andersson, O., *Microstructure of long and short-fiber reinforced injection molded polyamide.* Polymer Composites, 1993. **14**(2): p. 116-125.